Investigation of the Rupture Initiation and Mechanical Performance of Alumina Port Covers for Integrated Rocket Ramjet Systems

A Thesis Presented for the
Master of Science
Degree
The University of Tennessee, Knoxville

Haley Regan Goldston
December 2021

Copyright © 2021 by Haley Regan Goldston
All rights reserved.

ACKNOWLEDGEMENTS

First and foremost, I would first like to thank my father and mother, Chad and Billie Goldston, for their endless encouragement, prayer and love for which I could never repay. I also want to thank my older brother, Chane Goldston, for cheering me on my entire life. My family inspires me to shoot for the moon and I would not be where I am today without their love and support. Additionally, I would like to acknowledge and thank my advisor, Dr. John Schmisseur, for giving me the opportunity develop into a graduate research student with the HORIZON research team. I also want to thank my "un-official advisor" Dr. Mark Gragston for dedicating so much of his time and attention to this research project and enduring the constant 80's music. I would also like to recognize Dr. Phillip Kreth and Dr. Trevor Moeller for their valuable contributions and for serving on my thesis committee, in addition to Dr. John Schmisseur and Dr. Mark Gragston. The collaborating port cover team members deserve acknowledgement for their time and expertise: Craig Francks, Lt. Deandra Dyer, Glenn Hrinda, David Buckwalter and Antony Farrington. I'd like to express my gratitude to Mr. Kirk Davenport for working incredibly hard in every aspect and Dr. Kenneth Langley for his guidance. Finally, I want to thank my peers and coworkers at UTSI for their valuable friendship.

This effort was supported under award number FA9101-20-F-0043.

ABSTRACT

Hypersonic flight is widely considered essential to ensure a competitive defensive capability in the United States. In hypersonic air breathing propulsion, cruise vehicles are a priority research and development area given the ease to which they can be implemented with existing DoD infrastructure. Advancements in ramjet engine systems, including integrated rocket ramjets, play a considerable role in military and space access hypersonic vehicle designs. By design, ramjets cannot produce static thrust. They first need to be brought to operational speeds with the help of a rocket booster. An integrated rocket ramjet (IRR) combines the booster phase and the ramjet phase in one single propulsion chain, further enhancing the systems efficiency. The key factor in IRR flight success is the separation of these two phases achieved by the use of a port cover, which will be discussed in detail throughout this paper.

In support of the continued maturation of IRR technologies, the University of Tennessee Space Institute has collaborated with Air Force Research Labs, NASA Langley Research Center and the Defense Science and Technology Labs to investigate the viability of alumina port covers through a numerical and experimental campaign. Verified by finite element stress analysis, UTSI tested alumina port covers with a 45-degree dome angle and 6mm thickness that were fabricated and purchased from three external vendors. Flight conditions were simulated using a high-pressure chamber and a mechanical fracturing mechanism was used to initiate fracture on the pressurized port covers.

High-speed cameras and retroreflective shadowgraphy techniques were used to obtain initial crack propagation patterns and average fragment velocity. The fragments were collected post-rupture and measured to estimate an average fragment size. It is imperative the fragment size is small enough to ensure no damage will occur to the internal structure of the flight vehicle during exit. Ultimately, the goal of this research is to determine if alumina port covers are suitable for vehicle use.

TABLE OF CONTENTS

Chapter One Introduction and Motivation 1
1.1 Ramjet Overview 4
1.2 Integrated Rocket Ramjet Overview 12
Chapter Two Literature Review 17
2.1 Survey of Prior Work 17
2.2 Materials Science 27
2.2.1 Fracture Mechanics 27
2.2.2 Material Properties 35
2.2.3 Microstructure 36
2.3 Manufacturing Processes 39
Chapter Three Experimental Methodology 42
3.1 Stress Analysis 42
3.2 High-Pressure Chamber 49
3.3 Diagnostic Techniques 53
3.3.1 Initial Crack Propagation 53
3.3.2 Retroreflective Shadowgraphy 55
3.3.3 Fragment Size Analysis 55
Chapter Four Results 60
4.1 Initial Crack Propagation 67
4.2 Fragment Velocity Analysis 70
4.3 Fragment Size Analysis 74
4.3.1 Fragment Recovery 76
4.4 Phenomena 80
Chapter Five conclusions 85
5.1 Future Work 88
References 91
Vita 95

LIST OF TABLES

Table 1.1. Summary of modern U.S. hypersonic weapons programs..... 3
Table 1.2. Historical U.S. ramjet and scramjet development programs. 11
Table 1.3. Historical U.S. IRR development programs. 14
Table 2.1 Mohr's Theory of Brittle Fracture intermediate stress criterion 34
Table 2.2 Alumina material properties 41
Table 4.1 Experimental test matrix..... 66
Table 4.2. Fragment recovery percentage and average fragment size correlation..... 77

LIST OF FIGURES

Figure 1.1. Characteristic engine performance determined by specific impulse 5
Figure 1.2. Two-dimensional ramjet engine schematic 7
Figure 1.3. Ramjet technology examples 8
Figure 1.4. Scramjet technology examples 10
Figure 1.5. Integrated rocket ramjet (IRR) schematic 15
Figure 1.6. Inlet port cover orientation 16
Figure 2.1. USAF ASALM missile illustration 18
Figure 2.2. ASALM-PTV propulsion system 19
Figure 2.3. Chemical Systems Division IRR port cover development 22
Figure 2.4. Chungnam National University port covers 23
Figure 2.5. Chungnam National University fracture pattern 24
Figure 2.6. AFRL SolidWorks stress analysis 25
Figure 2.7. AFRL CalculiX stress analysis 26
Figure 2.8. Tensile test schematic and results 28
Figure 2.9. Engineering stress strain curve 29
Figure 2.10. Griffith Theory of Brittle Fracture material specimen 31
Figure 2.11. Mohr's Theory of Brittle Fracture 33
Figure 2.12. Crystalline microstructure of alumina 37
Figure 2.13. Grain size chart 38
Figure 3.1. Port cover geometry 44
Figure 3.2. Stress analysis mesh details 45
Figure 3.3. Stress analysis loads and fixtures details 46
Figure 3.4. Maximum deflection 47
Figure 3.5. Maximum principal stress 48
Figure 3.6. High-pressure chamber 50
Figure 3.7. Fracture mechanism 51
Figure 3.8. Frame used to catch fragments 52
Figure 3.9. High-speed cameras and lenses 54
Figure 3.10. Initial crack propagation diagnostic 56
Figure 3.11. Retroreflective shadowgraphy diagram 57
Figure 3.12. Retroreflective shadowgraphy experimental setup 58
Figure 3.13. ImageJ technique 59
Figure 4.1. Port covers and microscopic surface images 62
Figure 4.2. Port cover orientation 63
Figure 4.3. Flip test images 64
Figure 4.4. Fracture initiation failures 65
Figure 4.5. Ortech initial crack propagation high-speed images 68
Figure 4.6. Stanford initial crack propagation high-speed images 69
Figure 4.7. Ortech shadowgraphy images 72
Figure 4.8. Stanford shadowgraphy images 73
Figure 4.9. Fragment size histograms 75

Figure 4.10. Ortech quadrant patterns, remaining rim pieces 78
Figure 4.11. Stanford quadrant patterns, remaining rim pieces 79
Figure 4.12. Shockwaves attached to port cover fragments 82
Figure 4.13. Mach disks 83
Figure 4.14. Triboluminescence 84
Figure 5.1. Multi-point fracture initiation 89
Figure 5.2. Scoring of port cover dome face 90

CHAPTER ONE

INTRODUCTION AND MOTIVATION

For the past 20 years, the United States has intermittently pursued the development of hypersonic systems for defense applications, and both the Pentagon and Congress have identified the development of hypersonic capabilities as a priority research and development area [1]. These superior systems could enable responsive, long-range, strike options against distant, defended, and/or time-critical threats when other forces are unavailable, denied access, or not preferred [2]. Hypersonic systems could enhance the U.S military's deterrence capabilities, a continuing goal of the modern DoD [3,4]. As a reflection of this continuing goal, the 2018 National Defense Strategy identified hypersonic capabilities as *essential* to ensuring a competitive defensive capability in the future [1].

Open-source reporting indicates that both China and Russia have successfully tested numerous hypersonic glide vehicles, and both countries are expected to field operational capability [1]. The growing interest in these technologies in foreign countries leads to a heightened focus in the United States on the strategic threat posed by hypersonic flight. Conventionally armed hypersonic weapons operate by using only kinetic energy, or energy derived from motion [5]. Most U.S. hypersonic weapons programs are to be conventionally armed, in contrast to those in Russia and China which are being designed for use with a nuclear warhead [6]. Currently, the United States does not have defenses to hold China and Russia at risk [7]. According to one expert, a nuclear-armed glider would be effective if it were 10 or even 100 times less accurate than a conventionally-armed glider due to nuclear blast effects [8]. As a result, U.S. hypersonic weapons will be more technically challenging to develop and require greater accuracy than nuclear-armed systems [1].

Hypersonic flight regimes received a great deal of attention between the years 1955-1970 thanks to atmospheric entry vehicles such as intercontinental ballistic missiles (ICBMs), which encounter Mach 25 and the Apollo lunar return vehicle reentering the atmosphere at Mach 36 [9]. Hypersonic speed is best defined as the flow regime at which aerodynamic heating and viscous interactions dominate the flow with the increasing Mach number [9]. When describing different flow regimes, the Mach number is typically the basis for the distinction [9]. Although it is generally thought of as arbitrary, hypersonic flow is classified as Mach 5 and above [10]. Recall from oblique shock theory that across a shock wave, density increases with the Mach number across. For flow over a hypersonic body, this increase in density means the distance between the body and the shock wave, known as the shock layer, can become very thin [10]. One consequence of this thin shock layer is that major viscous interactions frequently occur between the shock wave and boundary layer, resulting in extremely high temperatures. [9]. Increasingly high temperatures, where the specific heat ratio is no longer the constant γ_{air}=1.4, risk dissociation or ionization of air. The free electrons that are subsequently released effectively absorb radio-frequency radiation, which causes what is known as communication-blackout for hypersonic entry vehicles [10].

Hypersonic vehicles are generally grouped into two categories: hypersonic glide vehicles (HGV) and hypersonic cruise vehicles. HGVs have minimal or no self-contained propulsion element, but instead are launched from a rocket before gliding to a target. In contrast, cruise vehicles utilize active air-breathing propulsion systems, which can include ramjets or their supersonic counterpart, scramjets. Airbreathing engines obtain all of the oxidizer necessary for fuel combustion from the atmosphere. They can be easily implemented with existing DoD infrastructure in large numbers and interface well with current fifth-generation fighter jets and bombers [7]. Glide vehicles have the advantage of longer ranges while cruise vehicles are smaller and more affordable. Both technologies are considered to be of interest in the development of a full hypersonic capability spectrum. However, this investigation focuses air-breathing cruise vehicles which includes ramjets, their supersonic counterpart, scramjets.

Hypersonic airbreathing propulsion is challenging in itself. Proper aerodynamic integration with the vehicle is crucial to successful flight. In subsonic and supersonic aircraft, the components for providing lift, propulsion and volume are distinct components that are treated as separate aerodynamic bodies, while hypersonic aerodynamic design closely integrates these components [10]. Early hypersonic engines were attached to the vehicle by pylons or struts, which created drag that virtually cancelled out any internal thrust produced by the air breathing engine. Another early design flaw featured narrow internal passages dominated by wall effects which hindered compression, choking the flow [11]. Design challenges are compounded by increasingly severe flight conditions. To avoid excessive pressures at hypersonic speeds, these vehicles fly at very high altitudes where the air density is only one-hundredth or one-thousandth of the sea level value. Since airbreathing engines rely on airflow to generate the thrust that lifts and accelerates the vehicle, they are inclined to suffocate at these altitudes where rare air exists [11]. To demonstrate the scientific and engineering challenges associated with developing hypersonic capabilities, the Pentagon's FY2021 budget request for hypersonic-related research is $3.2 billion—a 24% increase from the previously funded FY2020 amount [1]. Table 1.1 lists the major offensive hypersonic technology programs in development for the United States [12].

Advancement of ramjet systems, including integrated rocket ramjets (IRR), are of extreme interest in hypersonic research due to their maneuverability, rapid travel and non-traditional trajectories. The key factor in IRR flight success is achieved by the use of an inlet port cover. The University of Tennessee Space Institute (UTSI) has collaborated with Air Force Research Labs (AFRL), NASA Langley Research Center and the Defense Science and Technology Labs to investigate the viability of inlet port covers made from the material alumina. Research objectives proposed for this campaign include the design of a high-pressure chamber that is capable of simulating flight conditions for ramjets and testing inlet port covers. Another major research objective is to design and fabricate a mechanical fracture mechanism to initiate crack propagation on the port cover in order to understand the loading capabilities and fracture mechanics. Ultimately, the goal of this research is to determine if alumina port covers are suitable for vehicle use.

Table 1.1: Summary of modern U.S. hypersonic weapons programs [12].

Program	FY2020 ($ in millions)	PB2021 ($ in millions)	Schedule
Conventional Prompt Strike (CPS)	512	1,008	IOC in FY2028
Long-Range Hypersonic Weapon (LRHW)	404	801	Flight tests through 2023
AGM-183 Air-Launched Rapid Response Weapon (ARRW)	286	382	Flight tests through 2022
Hypersonic Conventional Strike Weapon (HCSW)	290	0	Cancelled in 2020
Tactical Boost Glide (TBG)	152	117	Testing through 2021
Operational Fires (OpFires)	50	40	Testing through 2021; weapon system integration in 2021
Hypersonic Air-breathing Weapon Concept (HAWC)	20	7	Flight tests in 2020; final program reviews in 2021

1.1 Ramjet Overview

For many modern aerospace vehicles, turbojets or traditional rocket-powered systems are commonly used for propulsion. The first step in any conventional thermal power cycle is compression [13]. Turbojets are airbreathing engines that use a series of turbine fan blades to compress the air, generally employed in vehicles that operate in subsonic flow. Air compression adds energy to flow which in turn increases pressure and temperature as well. As observed in a typical Brayton cycle that powers car engines, high pressure is the secret to extracting work energy from combustion processes. Although turbojets can operate at supersonic speeds, increased drag and/or pressure losses lead to a huge efficiency deficit.

Traditional rocket-powered propulsion systems can operate at various Mach numbers. However, it must carry all of its oxidizer along with its fuel supply, which limits its efficiency due to the added mass. In the hypersonic flight regime, both turbojets and traditional rockets operate with low efficiency compared to that of a ramjet, as determined by specific impulse (change in momentum per unit of propellant.) While rockets produce an impressive specific impulse of around 600 seconds, ramjets produce specific impulse between 1000 and 4000 seconds, depicted in Figure 1.1 [14].

Since its origination by Rene Lorin of France in 1913, the ramjet has undergone a relatively long development period [13]. It is well known that the theoretical performance of the ramjet propulsion system is far better than alternative systems [14]. Advantages of utilizing ramjet technology include higher Mach number capabilities, longer powered range, thrust modulation and efficient maneuverability. Efficient ramjet engines can be designed and produced for airbreathing vehicles with speeds in the hypersonic flight regime [15]. The subsonic combustion ramjet will be referred to simply as ramjet and it typically operates in the Mach 2 - 4.5 speed regime. Present technology indicates that the fully mature ramjet will reach its greatest overall efficiency somewhere in the range Mach 6 to Mach 8 [15]. The supersonic combustion ramjet (scramjet) typically operates at speeds above Mach 4 [16].

Neither ramjets nor their supersonic counterparts, scramjets, need to be axially symmetric around a centerline because they have no rotating machinery [9]. The ramjet has been called a flying stovepipe, due to the absence of moving parts. Ramjet technology has evolved from the early simple subsonic “flying stovepipe” to its role in the complex concepts embedded within military and space access vehicle designs of today [13]. The basic ramjet engine consists of an inlet, diffuser, combustor and exhaust nozzle. It is convenient to describe the essential features of ramjet engines in a two-dimensional diagram by following the airflow from the undisturbed freestream from the far left until it exits the engine at the far right, as pictured in Figure 1.2 [9].

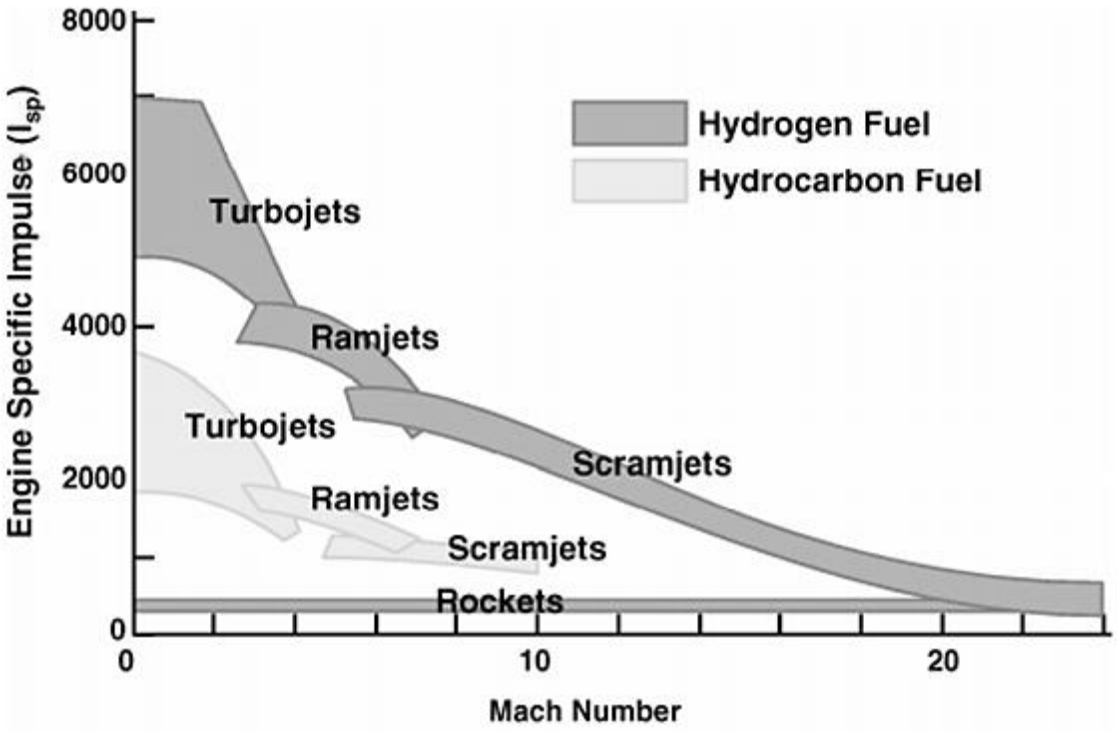

Figure 1.1: Characteristic engine performance determined by specific impulse [14].

Simple in concept, ramjets operate in a typical Brayton cycle: combustion of fuel in compressed air, the critical requirement to achieve ramjet and scramjet operation. Instead of using turbine blades, ramjets depend on the forward motion of the vehicle in the overall propulsion system to compress air by ram effect. Thus, compression strongly depends on velocity and increases dramatically with vehicle speed. The high-speed air is decelerated to subsonic conditions via normal shock train in the ramjet inlet, which serves the same purpose as a compressor. The position of the normal shock system is determined by the flight speed, air captured, total pressure losses, heat addition, inlet boundary layer height and exit nozzle throat size. Fluid dynamics knowledge provides that air flowing through a shockwave will experience an increase in entropy, therefore total pressure losses will always be present during ramjet combustion [17]. As Mach number increases, entropy increases which in turn compounds total pressure losses. This explains why ramjet efficiency declines in higher Mach number ranges. The inlet boundary layer height associated with viscous effects is critical in minimizing unstart potential, one of the challenges faced in ramjet operation [18].

Following the compression process, air is delivered through the diffuser into a combustion chamber. Fuel is then injected and burned with the aid of a flame holder, which imparts thermal energy to the gas. Typically, flame holders utilize a recirculation technique to trap some portion of the energy local to the injection point in order to provide stable ignition. Finally, the gas expands to high velocity through a convergent-divergent nozzle at speeds greater than the entering air. This conversion of thermal energy to kinetic energy produces forward thrust. Because the ramjet uses external air for combustion, it is a more efficient propulsion system for flight within the atmosphere than a rocket, which must carry all of its oxidizer along with its fuel supply.

Thrust generated in a ramjet process strongly depends on compression, which requires the ramjet to have significant forward velocity for practical operation. However, unlike turbojets or rocket engines, ramjet vehicles cannot produce static thrust. They first need to be accelerated to supersonic operational speeds with the help of a rocket booster before transitioning to the ramjet phase.

Examples of ramjet technology are pictured in Figure 1.3 (a), (b) and (c) [19,20,21]. NASA's experimental X-15 program is considered one of the most successful research efforts in history as the world's first piloted vehicle to study the hypersonic flight regime. The X-15A model was dropped from NASA's B-52 carrier aircraft and featured a dummy ramjet engine that was used to obtain performance and stability data [19]. The RIM-8 Talos utilized ramjet technology and is one of the earliest surface-to-air missiles to equip US Navy aircraft carriers [20]. The last example is the state-of-the-art MBDA missile named the Meteor, which is designed to equip the F-35 Lightning [21].

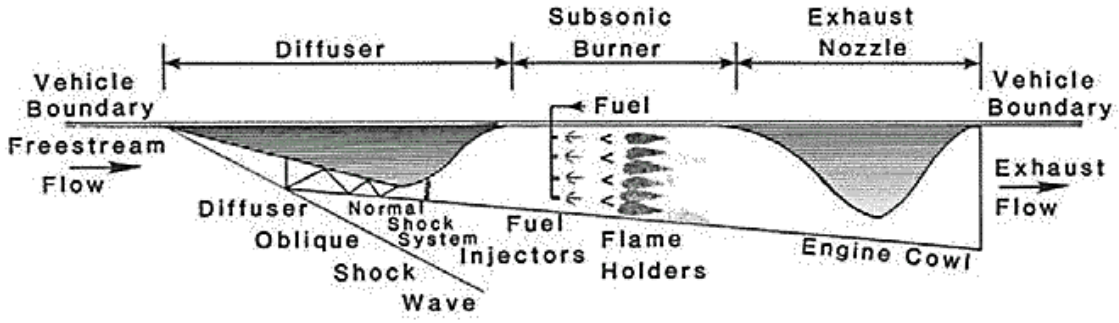

Figure 1.2: Two-dimensional ramjet engine schematic [9].

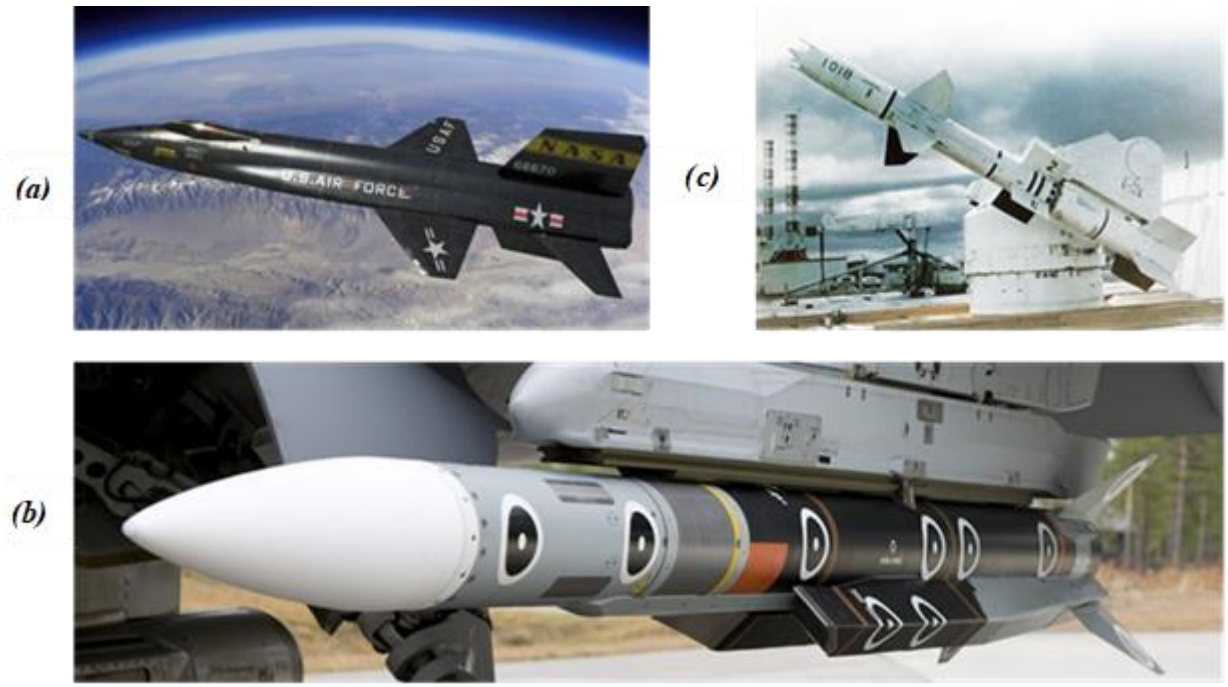

Figure 1.3: Ramjet technology examples (a) NASA X-15A hypersonic vehicle, (b) RIM-8 Talos US Navy surface-to-air missile, (c) MBDA Meteor missile [19,20,21].

Like ramjets, scramjets rely on the high-speed air relative to the vehicle in the overall propulsion system. When air passes through a shock train, temperatures can increase sharply. There is a risk of autoignition occurring at such temperatures which leads to unstable combustion in ramjet systems. The scramjet alleviates that risk by utilizing supersonic conditions during combustion instead of the air being slowed to subsonic flow via shock train in the inlet. Fuel is then injected in the diverging area combustor where it mixes and burns with the air. The unique combination of heat addition in a diverging area combustor and the absence of a nozzle throat permits a scramjet to operate effectively over a wider flight Mach number range than a conventional ramjet [3].

A variety of experimental programs have tested scramjet viability, including NASA's X-43, Boeing's X-51 and NASA's HIFiRE program, pictured in Figure 1.4 (a), (b) and (c) [22,23,24]. Part of NASA's Hyper-X program, the X-43 was an experimental unmanned hypersonic aircraft that was dropped from a B-52 and achieved airspeed of Mach 9.6 [22]. Boeing's X-51 Waverider was also an experimental unmanned hypersonic aircraft that replaced the previously mentioned X-43 [23]. NASA's Hypersonic International Flight Research Experimentation (HIFiRE) program flight-tested experimental scramjet vehicles that successfully accelerated from Mach 6 to Mach 8 [24].

Although the scramjet offers a wider flight Mach number range, it faces its own unique challenges. Scramjets require fuel preconditioning for efficient combustion at flight speeds below Mach 7 [3]. The combination of a low air static temperature and short combustor residence time (<1 ms) entails storing additional highly-reactive liquid fuels, such as hydrogen, or preheating gaseous fuels to be combined with a pilot [3]. Residence time refers to how long it takes for a chemical reaction (in this case combustion) to complete. In order to avoid significant waste of energy, it is important to ensure there is enough time for combustion to occur before the flow exits the nozzle. Heavy hydrocarbon fuels burn more slowly because they undergo pyrolysis, which is the breakdown of hydrocarbons into smaller hydrocarbons. On the other hand, hydrogen fuel burns much more quickly and has a better chance of burning in faster moving flow experienced in scramjet systems, the caveat being hydrogen fuel's well-known dangers.

Table 1.2 summarizes notable U.S. ramjet and scramjet development programs [13]. Although high speed, high altitude, and long ranges were attained, each of these missiles suffered from the common ailment of massive size for delivered range [13].

Figure 1.4: Scramjet technology examples (a) NASA X-43 experimental hypersonic vehicle, (b) Boeing X-51 experimental hypersonic vehicle, (c) HiFIRE launch [22,23,24].

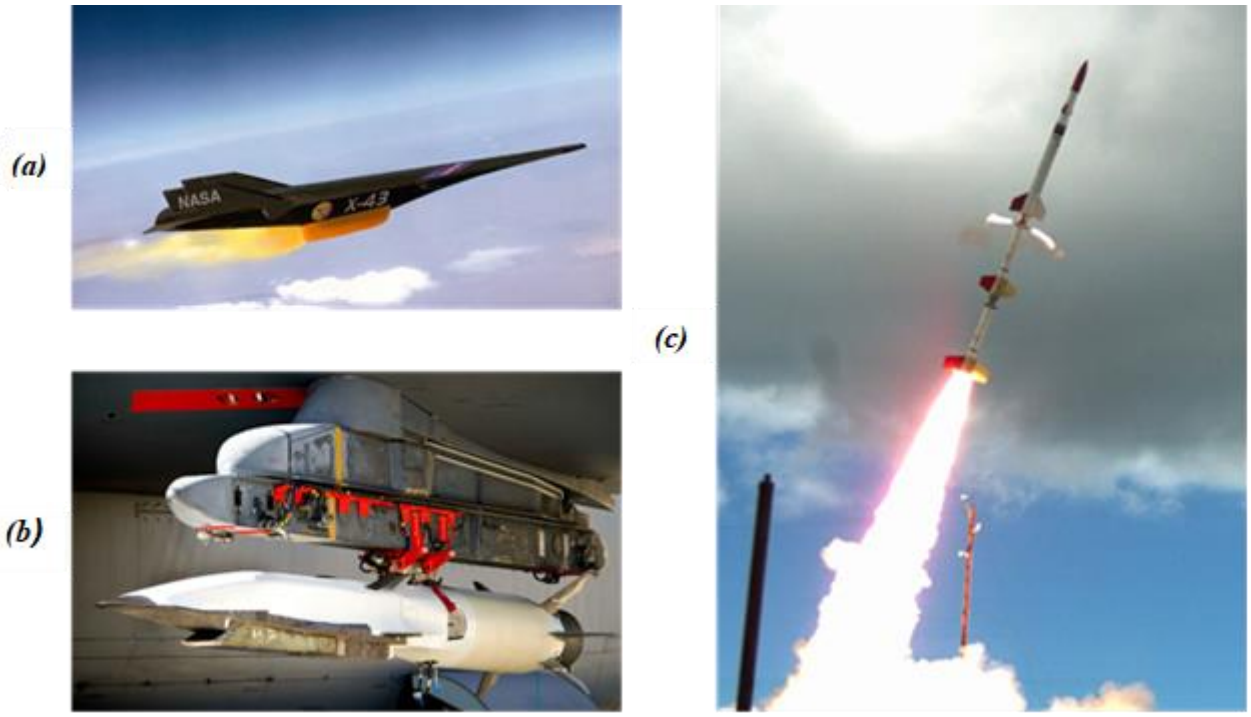

Table 1.2: Historical U.S. ramjet and scramjet development programs, (ramjet denoted by RJ, scramjet denoted by SJ) [13].

Vehicle	Dates	Cruise Mach #	Cruise altitude (ft)	Range (n. mi.)	Length/ Diameter (in/in)	Weight (lbm)
Cobra, RJ	1945-1946	2.0	20,000	____	__/6	240
Navaho, RJ	1946-1958	3.25	5,500	5,500	1,050/48	120,000
BOMARC, RJ	1950-1972	2.5-3.4	70,000-100,000	440	560/35	15,620
Talos, RJ	1950-1980	2.7	70,000	120	386/28	7,720
Typhon, RJ	1957-1965	4.1	100,000	200	333/16.75	6,160
Roadrunner, RJ	1960-1980	2.5	0-60,000	217	298/12	900
Hyperjet, RJ	1960-1966	5.0+	30,000	____	__/__	____
Vandal, RJ	1983-2020	2.2	____	43.5	434/28	8,210
Marquardt, SJ	1960-1970	3.0-5.0	____	____	88/10x15	____
SCRAM, SJ	1962-1977	7.5	100,000	350	288/26.2	5,470
WADM, SJ	1977-1986	4.0-6.0	80,000-100,000	500-900	256/21	3,750
NASP, SJ	1986-1994	0-26	0-Orbit	Orbital	__/__	500,000

1.2 Integrated Rocket Ramjet Overview

As previously discussed, ramjet operation depends on sufficient high-speed travel provided by a rocket boost phase. The integral rocket ramjet (IRR) design eliminates the need for external solid rocket motors which are necessary to accelerate the ramjet to operational speed by incorporating both the ramjet phase and rocket boost phase in one single propulsion chain [14]. The advent of the IRR addresses the primary design objective for weight and geometry constrained propulsion systems: enhanced packaging efficiencies. Understandably, IRR systems are identified as one of the top 10 enabling technologies for hypersonic propulsion [13]. Table 1.3 summarizes notable U.S. integral rocket ramjet development programs [13].

Although liquid or gaseous fueled systems exhibit superior performance, solid fuel integral rocket ramjets (SFIRRs) are preferred over liquid fuel integral rocket ramjets (LFIRRs) because of the simplicity of the fuel supply. The use of compacted solid-fuel also contributes to a considerable reduction in size, which provides two to three times the range of the comparably sized high-performance rocket motor [7]. This solid-fuel preference dominates only when the fuel throttling requirements are minimal: flight altitude and Mach number variations are limited [16].

The primary feature of the IRR that distinguishes it from the ramjet engine is the integration of two operational phases into a single propulsion chain, illustrated in Figure 1.5. The initial boost phase is necessary to accelerate the vehicle to speeds that support transition into ramjet operation [9,25]. The interaction of the rocket booster and ramjet phase occurs in the combustion chamber, which houses both the solid rocket propellant of the boost phase and the combustion process of the ramjet engine.

During the initial boost-phase powered by the rocket component, it is necessary to block the ramjet intake to prevent by-products from traveling upstream [25]. This problem is solved by implementing a frangible port cover that separates the two phases, pictured in Figure 1.6. The ramjet air inlet is essentially sealed by frangible port cover, forming a closed rocket motor. To allow for a smooth transition between the two phases, structural integrity of the port cover is essential to account for the high pressure, high temperature and vibration effects. The port cover acts as a stress-bearing member when the combustor pressure is greater than ram air pressure during solid propellant booster operation. To improve efficiency, a booster nozzle with a smaller throat area is inserted within the ramjet nozzle [26].

Once the solid rocket propellant from the boost phase has completely burned out and the booster tail-off pressure passes below the ram air pressure, the port cover is intentionally fractured and its fragments and the nozzle are ejected. The port cover is intended for one-time use as it is specifically designed to fracture and exit through the exhaust, however these fragments do not travel through a straight exit path. While travelling to the exhaust, it is important that the fragments do not damage the internal structure; hence, they must be

sufficiently small. Fragmentation into dust-sized particles would be the ideal outcome, although unrealistic. Following fracture, the removed port cover allows the compressed air to flow and therefore oxidation of fuel in the now empty combustion chamber, initiating ramjet operation.

It is important to keep in mind the material choice for the port cover used in IRR systems. As previously mentioned, the port cover will experience large pressure gradients and high vibrational effects throughout flight. The solid-rocket fuel in the rocket boost phase acts as an insulation to the port cover and protects it from extended high temperature exposure. However, when the solid rocket fuel is completely burned out, the port cover will encounter a very large temperature gradient and therefore must possess high thermal resistivity properties.

The most critical point in the flight of an IRR missile system is the ramjet takeover [13]. Proper and complete fragmentation of the port cover is necessary in order to allow for a rapid transition from rocket-boost phase to ramjet phase. Brittleness and high frangibility are imperative material properties for the port cover in order to ensure immediate fracture and to prevent inlet blockage. With mass flow rates in mind, a port cover that fails to fragment completely will partially block the ramjet inlet, restricting the flow of compressed air that is necessary for ramjet operation. If sufficient ramjet thrust cannot be achieved to overcome drag, then the entire mission is lost and considered to be a catastrophic failure. It was Prandtl who introduced the concept of healthy flows, and IRR operation is no exception [17].

Table 1.3: Historical U.S. IRR development programs [13].

Vehicle	Dates	Cruise Mach #	Cruise altitude (ft)	Range (n. mi.)	Length/ Diameter (in/in)	Weight (lbm)
Rare	1955-1960	2.3	50,000	____	120/5	153
Crow	1956-1964	3.0	50,000	97	127/8	370
LASRM	1964-1967	2.5	0-60,000	50	168/15	1,566
ASALM	1965-1980	2.5-4.0	10,000-80,000	56	168/20	2,415
ALVRJ-STM	1968-1979	3.0	0-40,000	28-100	179/15	1,480
ASALM-PTV	1976-1984	2.5-4.0	10,000-80,000	56	168/20	2,415
LIFRAM/SOFRAM	1976-1981	3.0+	____	150	144/8	650
SLAT	1986-1992	2.5	0	50	218/21	2,445

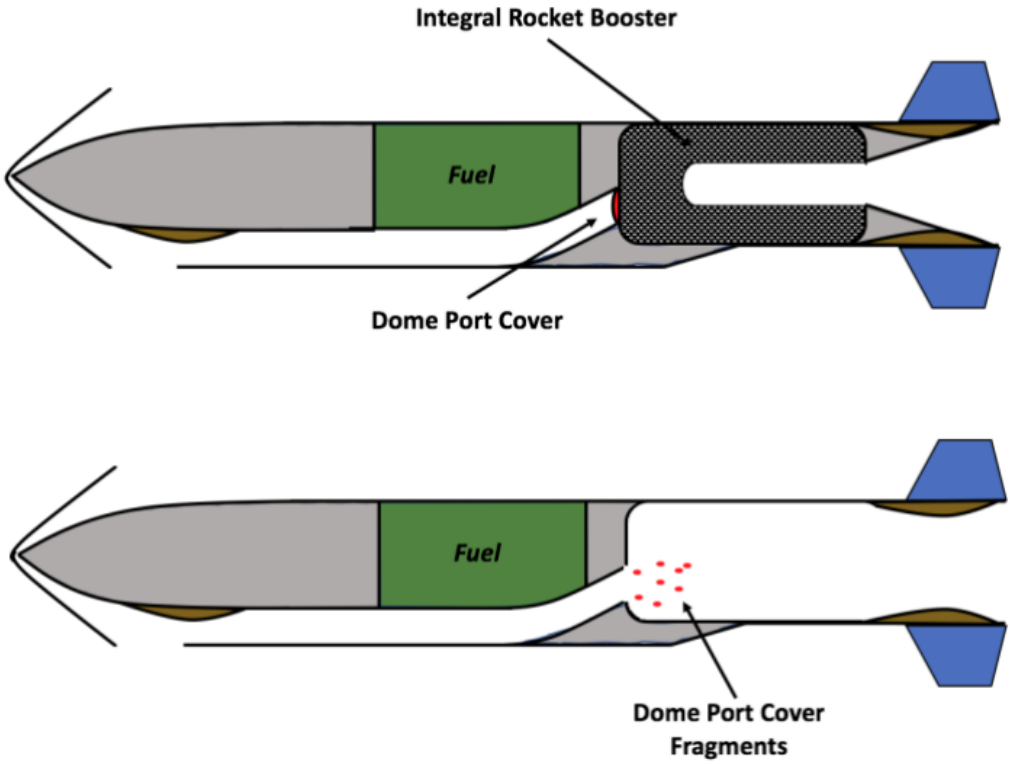

Figure 1.5: Integrated rocket ramjet (IRR) schematic.

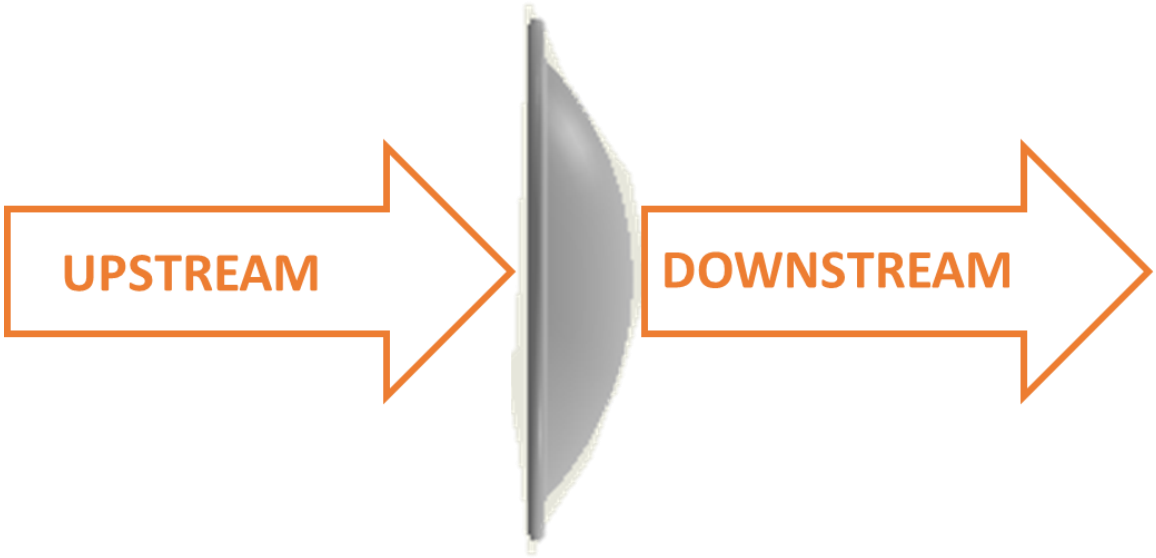

Figure 1.6: Inlet port cover orientation.

CHAPTER TWO
LITERATURE REVIEW

2.1 Survey of Prior Work

Before tackling the research objectives proposed for this investigation, it is important to review and understand prior work specific to port covers used in integrated ramjet rocket (IRR) systems. The first IRR technology featuring a frangible port cover was developed in the late 1970's for a supersonic missile program named Advanced Strategic Air-Launched Missile (ASALM) for the United States Air Force. The missile, expected to be carried by B-1 bombers, was intended for air-to-air, air-to-surface and anti-airborne warning and control system (AWACS) roles [13]. Operating at Mach 4.5, it was about 4.3 meters long with a range of 480 km. Figure 2.1 illustrates the ASALM design which featured no wings, but was instead guided by small fins at the tail. Several key features differentiated the ASALM weapon from its predecessors including its chin inlet, S-duct and the fuel injection aerogrid device [14]. However, the major innovation was the IRR propulsion system which featured a frangible chemically strengthened glass port cover. This innovative technology provided improved speed and range over the earlier missile, as well as improved performance against hardened targets [2,9]. The ASALM carried the same 1000-lb conventional warheads as the Tomahawk cruise missile, but was five times faster and had an improved altitude exceeding sixteen miles instead of the previously achieved altitude of 200 feet, making it essentially untouchable to all known defenses [27].

IRR technology continued to mature during the ASALM propulsion technology validation (PTV) program [14]. The ASALM-PTV IRR propulsion system is illustrated in Figure 2.2. The PTV missile was designed in the same range category as popular surface-to-air missiles Bomarc and Typhon [16], but with about one-eighth the launch weight. After ground test development, seven missiles were flight tested over a broad range of conditions covering most of the design envelope, with a 100% IRR operation success rate. Flight data showed rapid transition from rocket boost phase to ramjet, about 100 milliseconds in duration [14], further emphasizing the importance of the combustion port cover's role in successful IRR flight.

Marquardt, a well-known aeronautical engineering firm, developed the frangible glass port cover used in ASALM-PTV. The one-inch thick dome was sealed in the chin inlet by an O-ring. The interior inlet wall featured a machined "seat" to prevent the port cover from moving upstream when subject to pressure loads. Fracture was initiated on the port cover by an explosive detonation cord mounted on the dome face. Typical of frangible glass, it shattered into one-inch size fragments, consistent with its thickness. Remarkably, those fragments exited the ramjet nozzle easily and posed very little threat to the missile system [26].

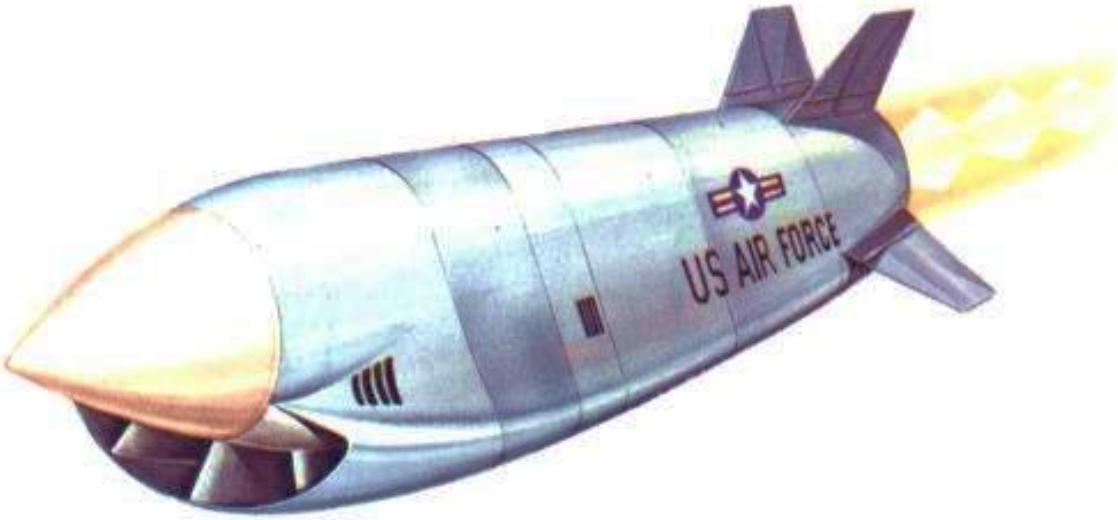

Figure 2.1: USAF ASALM missile illustration, Martin Marietta design [13].

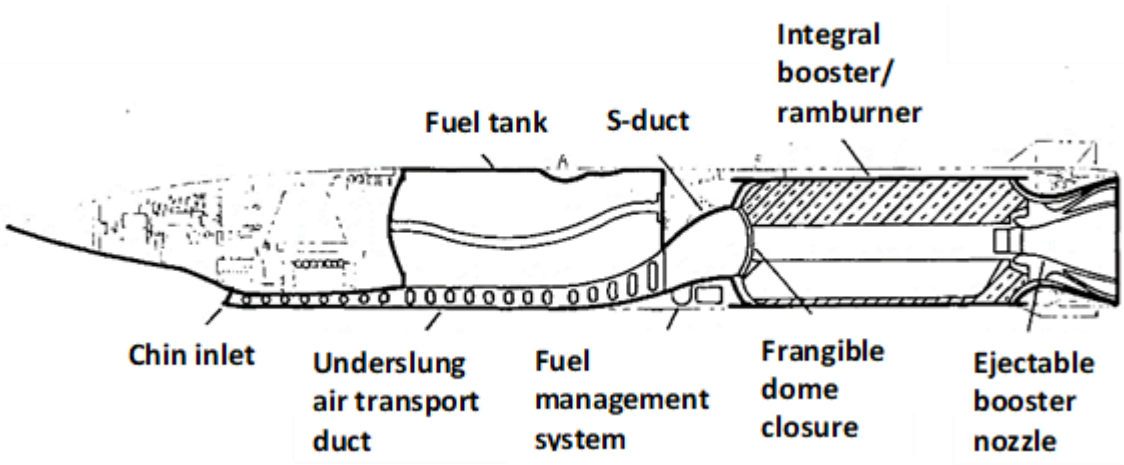

Figure 2.2: ASALM-PTV propulsion system [26].

Just as Sir Isaac Newton wrote, “If I have seen farther than others, it is because I stand on the shoulders of giants.” [28] The groundbreaking ASALM program results have served as a major foothold for the advancement of IRR systems, towards the mission of hypersonic capabilities [16].

During the innovative ASALM era, a substantial technology base for port cover design was developed in support of the first IRR flight demonstration programs. The notable United States Air Force Low Altitude Supersonic Ramjet Missile (LASRM) and the United States Navy Advanced Low Volume Ramjet (ALVRJ) programs featured single-piece metal port covers [29]. Although the port covers functioned satisfactorily, further design simplification, reduced costs, minimized ejection hazard and high reliability were desired.

In support of the advancement of IRR technologies, Chemical Systems Division performed an experimental research study focused on exploring alternative port cover designs [29]. The port covers studied in this campaign were grouped into four categories: frangible, linear shaped charge (LSC), semi-consumable, and flexible membrane. Along with the integral ejectable port covers, a variety of mechanical-type concepts were also considered, pictured in Figure 2.3 (a) and (b). The research demonstrated the basic design feasibility of frangible and mechanical port cover concepts for application to integral rocket ramjets, ultimately determining the frangible ceramic port covers offer lower ejecta risk than metal port covers and offer more structural reliability than frangible glass at a lower cost [29]. In brittle materials with high frangibility properties, it is a common concern that early failure can occur in the presence of a crack or flaw in the material. Since the port covers are exposed to a high-pressure gradient and severe vibrational effects, the structural integrity of frangible ceramic port covers exhibited a lower risk of early failure than that of frangible glass.

Fast forward to the year 2010, Chungnam National University in Daejeon, South Korea investigated fracture phenomena of flat plate and dome shaped port covers made of ceramic coated glass, illustrated in Figure 2.4 [30]. The objective of this study was to evaluate the fracture pressures for 3 mm, 4.5 mm and 6 mm thick port covers of flat plate geometries versus dome geometries using a basic shock tube to initiate fracture. Researchers utilized limited high-speed imaging to see the fracture process and compared the experimental results with computational expectations [30]. Upon fracture, the port cover featuring dome geometry is removed along the transition part of the curvature where the dome meets the flat rim region. This fracture pattern correlated well with the theoretical characteristics expected in this research. The fracture pressures for various thickness to diameter ratios were collected and shown to be linearly related and the average fragment sizes were between 2-8 mm^2 [30]. Chungnam National University’s results provide qualitative fracture pattern details and a comparative average fragment size, pictured in Figure 2.5 [30].

Due to variation in the properties of chemically strengthened glass brought about by proprietary approaches unique to each vendor, alternative materials are of interest. The inconsistency of chemically strengthened glass properties motivated the Naval Air Warfare Center to investigate an alternative material in the year 2016 [25]. As previously discussed, port covers must be sourced from materials with low tensile strength, high compressive strength, high frangibility and good thermal resistivity. Alumina, an engineering ceramic, was found to be a viable option since it possesses these qualities, is widely available and the mechanical properties are easily obtainable. The Naval Air Warfare Center suggested alumina to be a favorable alternative material. The material alumina will be discussed in further detail in the following chapters.

Pursuing the newly suggested material, the Air Force Research Laboratory (AFRL) performed a numerical campaign that utilized finite element analysis (FEA) on alumina port covers ranging in thickness and dome angles. Finite element analysis is a method used to simulate how a model behaves under specified conditions [31]. Following initial design parameters set in place during the ASALM port cover design, stress analysis simulations were performed to compare maximum deflection and maximum principal stresses between the different geometries. The SolidWorks stress analysis tool [32] was used in this numerical campaign and the results were further verified by the CalculiX stress analysis solver [33]. AFRL's evaluation of the alumina port covers proved that the thickness throughout to be the most efficient dimensions [25]. The maximum deflection and maximum principal stress results using Solidworks for a port cover with a 45° dome angle and 6mm are displayed in Figure 2.6 (a) and (b), respectively. The maximum deflection and maximum principal stress results using CalculiX for a port cover with a 45° dome angle and 6mm are displayed in Figure 2.7 (a) and (b), respectively.

Although countless literature can be found that describe in great detail the history, application and operation of hypersonic air breathing propulsion systems in general [34,35,36], this literature review is focused on the innovative IRR technologies, more specifically the campaigns that study the port covers that are used to achieve successful IRR operation. This survey of prior work was taken deeply into consideration when determining the research objectives proposed for this investigation. The University of Tennessee Space Institute has closely followed the lead of the Naval Air Warfare Center's suggested material choice of alumina for the port covers that are tested as well as AFRL's evaluation of the most efficient port cover geometry to feature a 45° dome angle and 6mm thickness throughout.

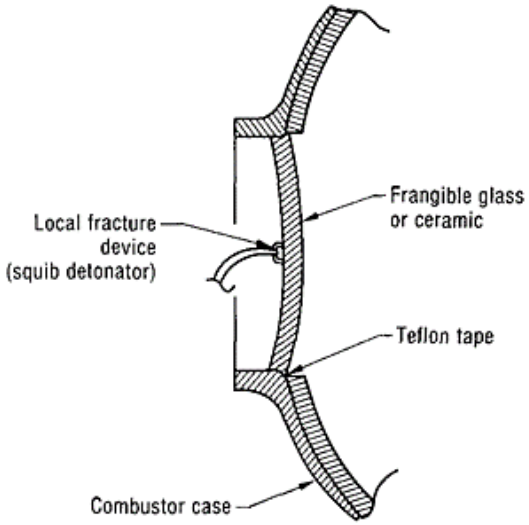

(a)

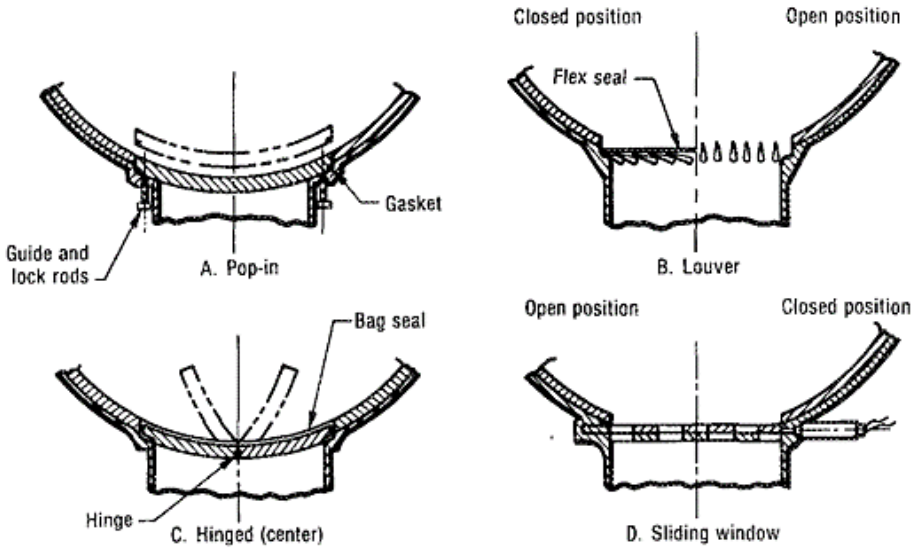

(b)

Figure 2.3: Chemical Systems Division IRR port cover development experimental port covers, (a) frangible port cover (b) mechanical port cover [29].

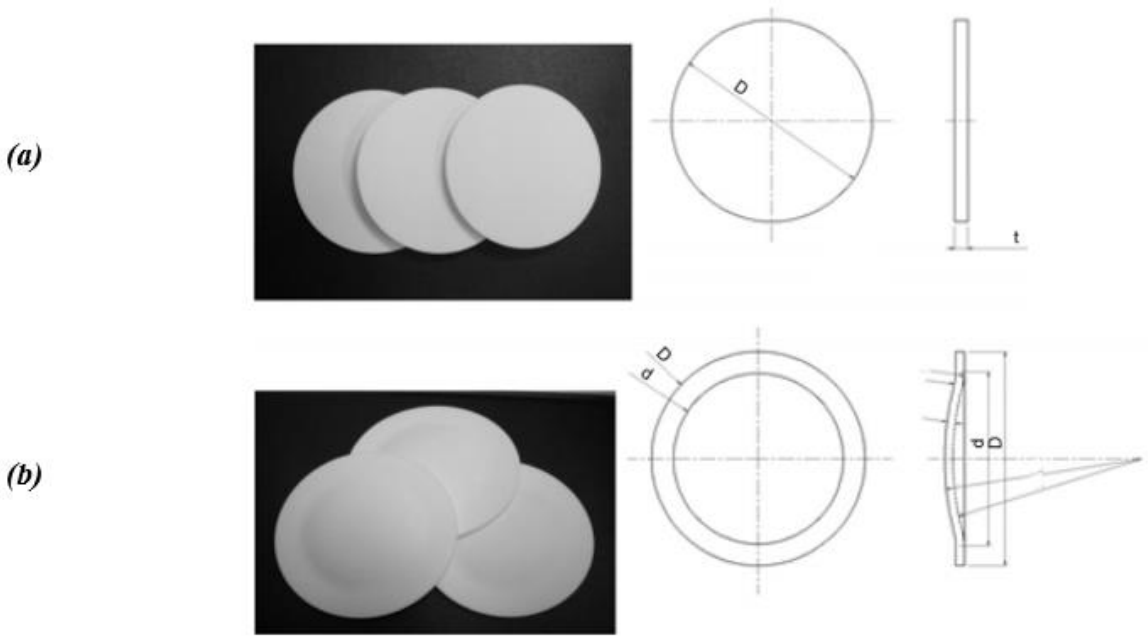

Figure 2.4: Chungnam National University (a) flat plate and (b) dome ceramic coated glass port covers [30].

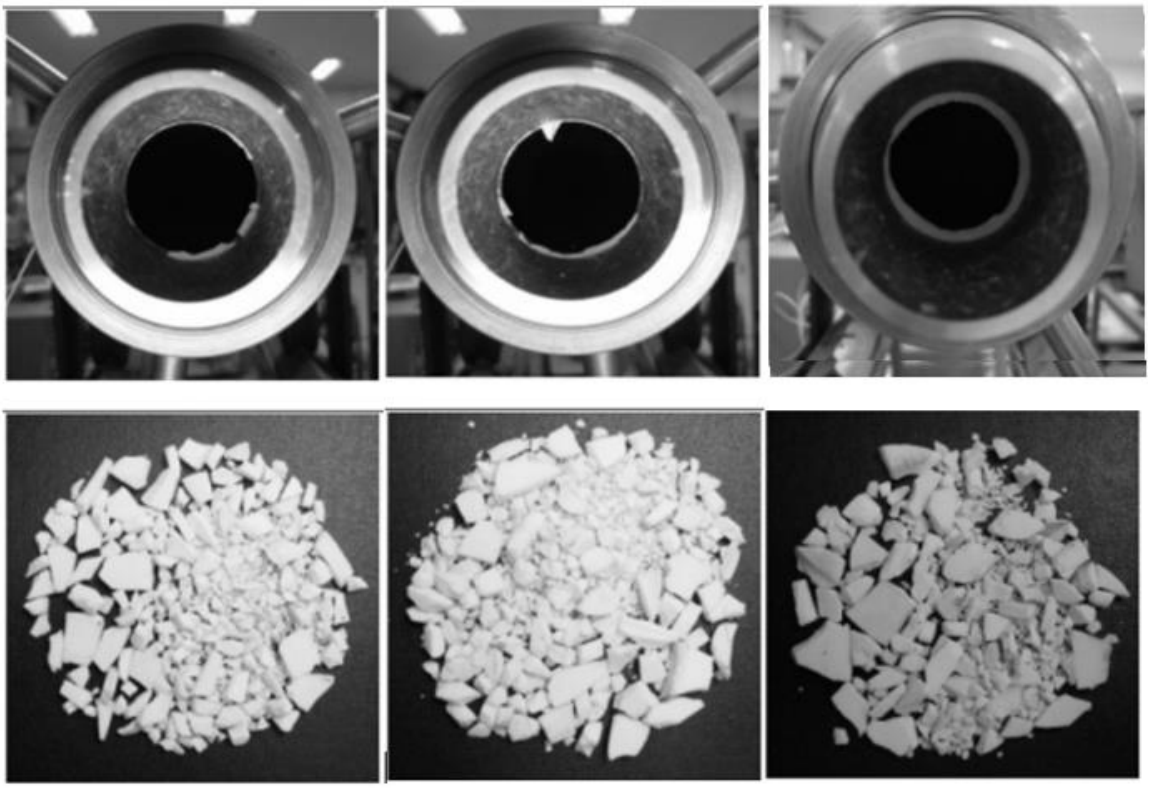

Figure 2.5: Chungnam National University port cover fracture pattern and fragment size results, (a) plate, 3.0 mm (b) plate, 4.5 mm (c) dome, 3.0 mm [30].

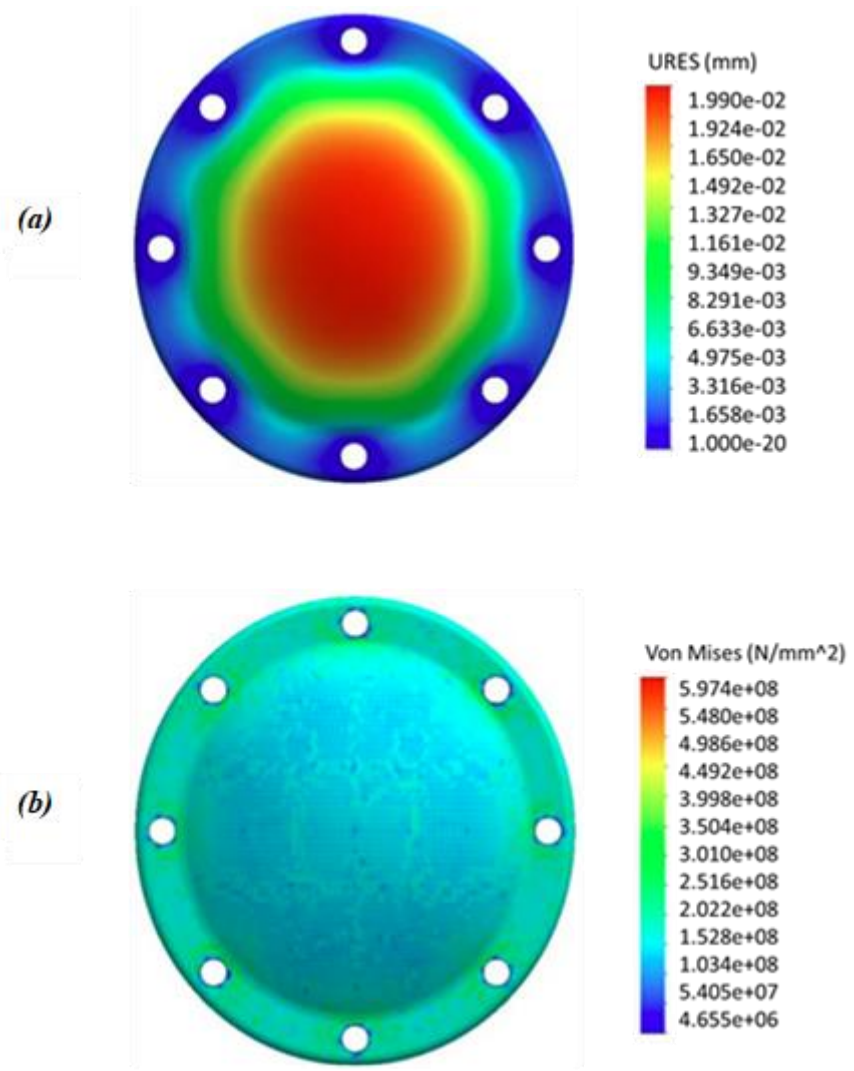

Figure 2.6: AFRL SolidWorks stress analysis results on 45° dome angle and 6mm thickness, (a) maximum deflection (b) maximum principal stress [25].

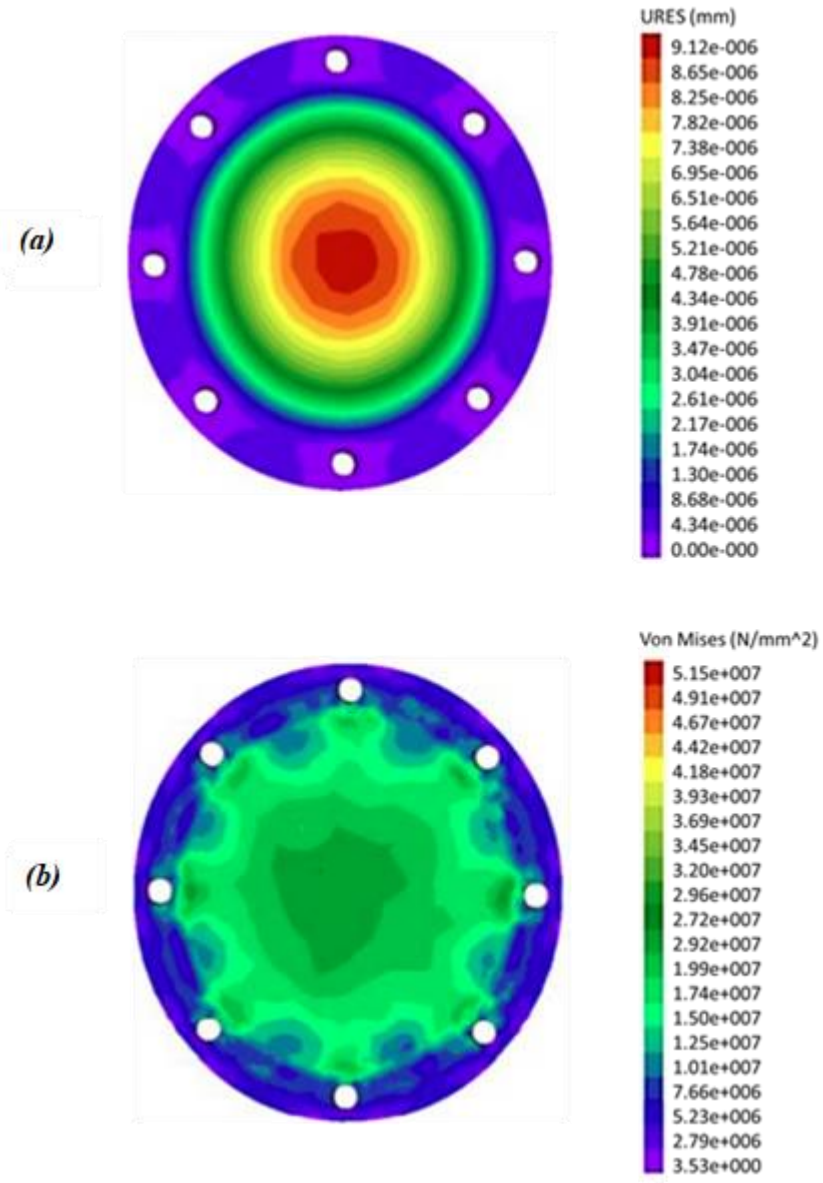

Figure 2.7: AFRL CalculiX stress analysis results on 45° dome angle and 6mm thickness, (a) maximum deflection (b) maximum principal stress [25].

2.2 Materials Science

2.2.1 Fracture Mechanics

Fracture mechanics is the field of mechanics concerned with the study of crack propagation that occurs in materials under stress as well as the subsequent resistance to fracture and ultimate failure [37]. In the study of material science, fracture is defined as the separation of a material into two or more parts. Fracture mechanisms are normally classified as either ductile or brittle. Ductile materials are capable of sustaining large amounts of plastic deformation before failure [38]. Plastic deformation describes the failure mode in which the deformation is permanent and non-reversible [38]. The ductile fracture process occurs relatively slowly and gives several warnings before the point of separation, normally occurring after the yield stress is surpassed. Yield stress is the point at which elastic deformation becomes plastic deformation [38]. Before the yield stress is reached, ductile materials will return to its original shape when the applied stress load is removed. Brittle fracture is the sudden failure of a material caused by the rapid propagation of cracks [38]. This mode of fracture features little or no plastic deformation and usually occurs at lower stress levels than ductile fracture.

An experimental test known as a tensile test is picture in Figure 2.8. A material specimen is clamped into the machine and a controlled tensile stress is applied until failure occurs. A ductile specimen and a brittle specimen are pictured post-tensile test with the corresponding fracture surfaces. Note that there is visible plastic deformation of the ductile specimen in which the diameter is decreased due to stretching of the material, known as necking. Ductile materials exhibit fracture at an angle approximately 45° from loading, which is displayed as the cup-cone fracture surface [39]. This fracture mode indicates that shear stress contributed more to the failure than the tensile stress that was applied. Notice that the brittle specimen displays no visible plastic deformation and features a smooth fracture surface, indicative of a clean break under tensile stress. While under compression, brittle materials fail in shear stress [39]. These failure modes are characteristic of brittle materials and can be attributed to the microstructure, which will be discussed in detail in a later section.

A plot known as an engineering stress-strain curve is obtained from the tensile test, pictured in Figure 2.9. The area under the curve for each material represent the materials ability to absorb energy without fracture, known as tensile toughness, u_f . The initial relationship between stress and strain is linear. Beyond this linear portion of the curve, the stress reaches the yield strength, S_y, where elastic deformation becomes plastic deformation [38]. For ductile materials, where considerable plastic strain takes place after yielding, some of the energy is stored in the microstructure of the material, but most of it is released in the form of heating [38]. Brittle materials exhibit no distinct yielding point because fracture occurs very close to the S_y value [38]. The stress–strain response curve is parabolic in shape with a very small area under it which indicates that despite high strength, brittle materials exhibit low tensile toughness [38].

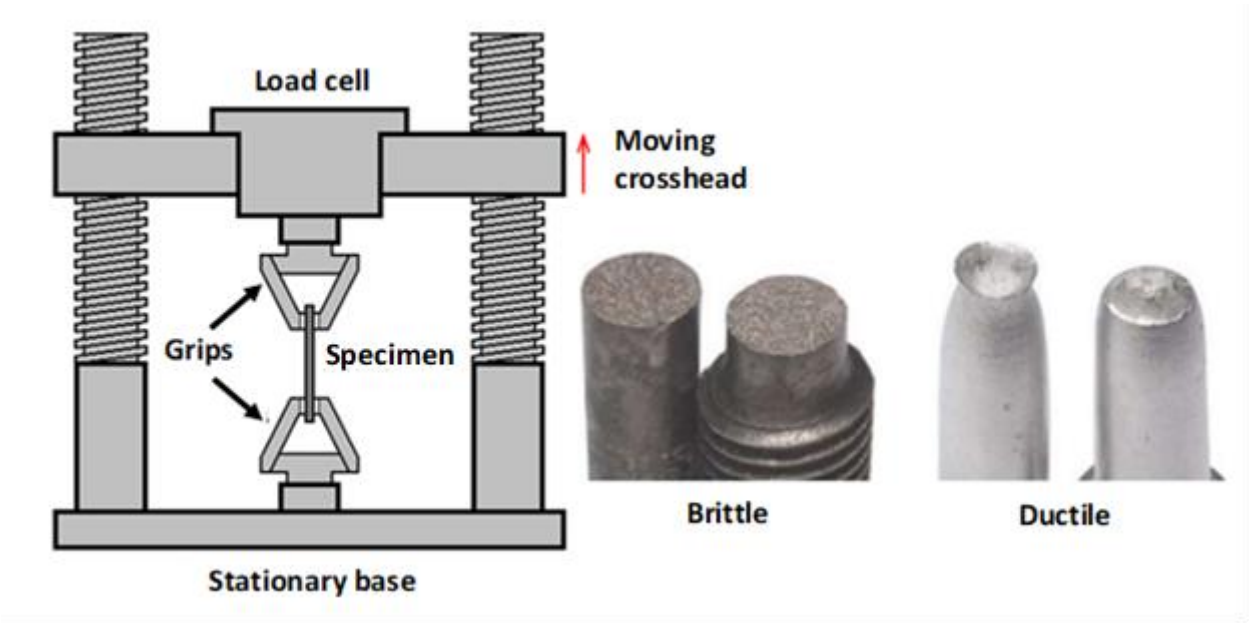

Figure 2.8: Tension test schematic and results for ductile versus brittle material samples [40].

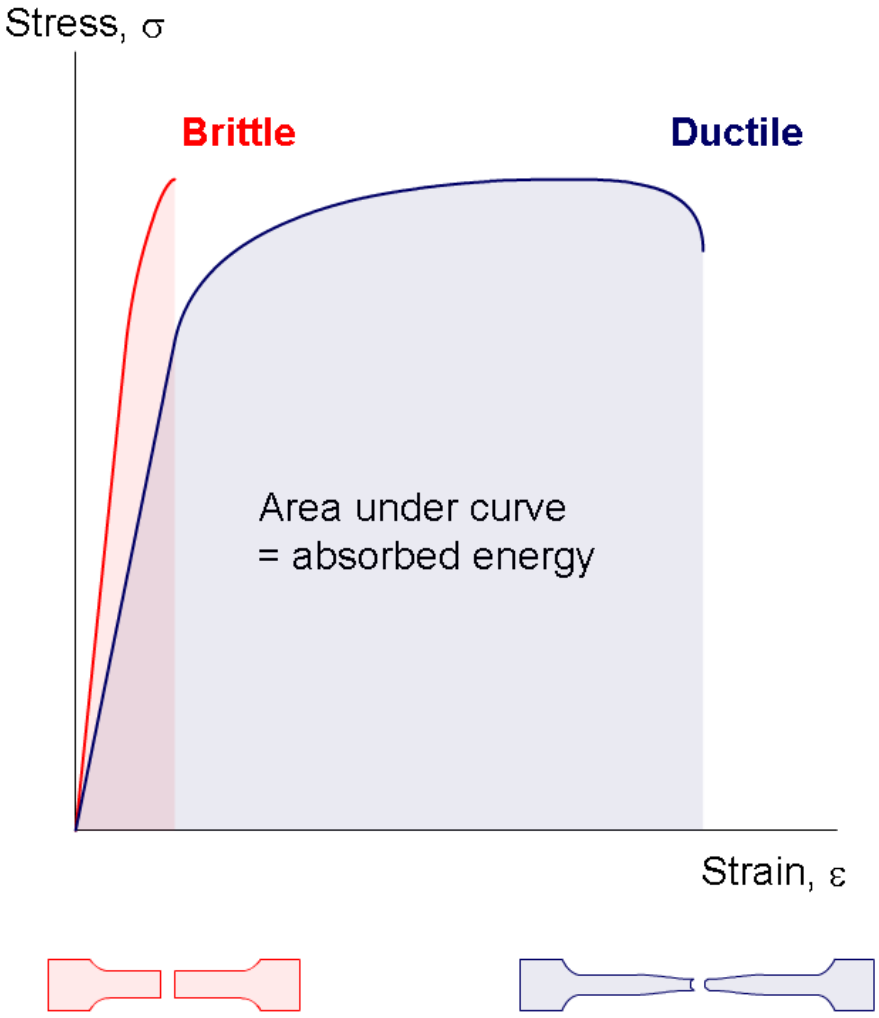

Figure 2.9: Engineering stress-strain curve for a ductile versus brittle fracture [40].

The foundation of fracture mechanics was first established in 1921 by the aeronautical engineer A. A. Griffith [41]. While performing stress field calculations restricted to brittle materials, he established the Griffith Theory of Brittle Fracture. It is often observed that brittle materials that failure can occur well below the yield stress of a material in the presence of cracks or flaws. This useful estimate of failure is based on the known initial crack length of a brittle material specimen.

Consider a material specimen in the shape of a thin plate of length l with a thru-crack of length $2c$, pictured in Figure 2.10 [41]. The corresponding force-deflection curve represents the thin plate under uniaxial tensile loading. Curve A represents a non-extending crack of length $2c$, while curve B represents a non-extending crack of length $2(c + \Delta c)$. The area between these two curves represents the strain energy that is released in order to extend the crack from $2c$ to $2(c + \Delta c)$. Using elasticity theory, Griffith showed that the energy released per unit thickness during a crack growth of $2\Delta c$ is

$$\Delta w_e = \frac{2\pi\sigma^2}{E} c\Delta \qquad \textbf{(1)}$$

Where γ_s represents the surface energy per unit area, the additional crack surface that is created requires surface energy per unit thickness given by

$$\Delta w_s = 2\gamma_s(2\Delta c) = 4\gamma_s\Delta c \qquad \textbf{(2)}$$

The Griffith criterion requires that in order for a crack to propagate, the strain energy that is released under uniaxial tensile loading must exceed the strain energy that was required to form the initial crack surface [41]. From this criterion, if $\Delta w_e < \Delta w_{s,}$ the crack will not grow since the released energy will be less than that required to create a new surface. If $\Delta w_e > \Delta w_{s,}$ crack growth will occur since adequate energy is available for creating the new surface. For estimating crack growth and subsequent failure, we must have the condition

$$\frac{2\pi\sigma^2}{E} c\Delta c \geq 4\gamma_s\Delta c \qquad \textbf{(3)}$$

Where E represents Young's Modulus, the critical fracture stress,σ_c, is determined by

$$\sigma_c = \sqrt{\frac{2E\gamma_s}{\pi c}} \qquad \textbf{(4)}$$

From this, the critical stress is clearly inversely proportional to $c^{\frac{1}{2}}$. The conclusion can be drawn that the smaller the flaw, the greater the value of σ_c is required to cause failure. The Griffith Theory of Brittle Fracture and corresponding equation forms the starting point of the modern fracture mechanics [41].

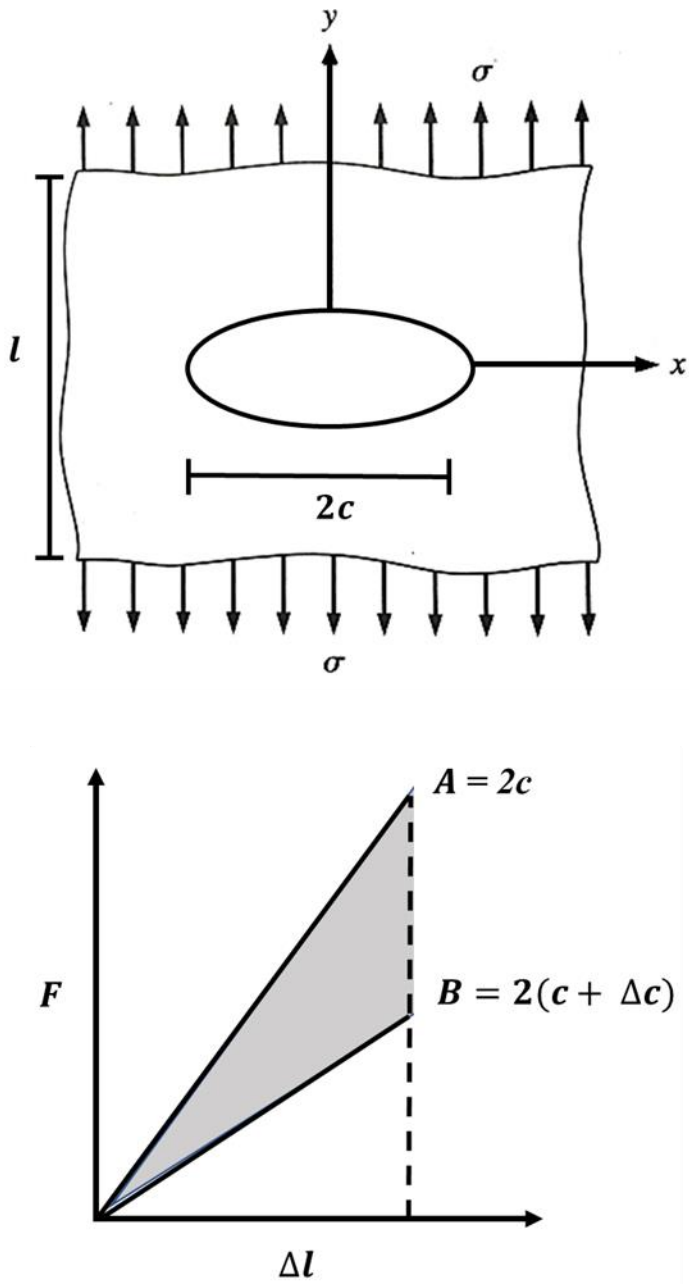

Figure 2.10: Material specimen of length l with initial crack length of $2c$ and its corresponding force-deflection curve [41].

When a part is subject to an applied load, such as tension, compression, pressure, etc., complex normal and shear stress occur. These stresses vary in magnitude and direction and the most severe stresses are known as principal stresses which act on the direction of principal axes [38]. Consider a point on a solid body that is represented by an *x-y-z* coordinate system. Considering normal stress and shear stress in each coordinate direction, the solid body at this point is subjected to six components of stress: the normal components of σ_x, σ_y and σ_z and the shear components τ_{xy}, τ_{yz} and τ_{zx} [38]. The relatively simple, yet practical case of plane stress is the state in which the stresses acting on one orthogonal plane are zero, meaning that $\sigma_z = \tau_{yz} = \tau_{zx} = 0$ [38]. Equilibrium of forces requires that moments about the x- and y- axes must equal zero, so τ_{yz} and τ_{zx} acting on the other two planes are also equal to zero [38]. The non-zero components remaining are σ_x, σ_y and τ_{xy}, reducing the body into tow-dimensional analysis [38].

The same state of plane stress can be designated to any other coordinate system and the new coordinate system is related to the original coordinate system by an angle of rotation, θ. This method of representing equivalent states of stress from one coordinate system to another is called transformation of axes and is represented by a series of equations known as transformation equations that are derived from Hooke's Law [38]. It is important to recognize that this transformation of axes does not result in new states of stress, but instead it is an equivalent representation on a new coordinate system [38].

A convenient graphical representation of the transformation between coordinate systems for plane stress, known as Mohr's circle, was developed by Otto Mohr in the 1880s [38]. Mohr's circle reduces principal stresses in a plane into two-dimensional components. contains all possible states of stress on or within the circle [41]. Plotted on σ versus τ axes, the two ends of a diameter of Mohr's circle can be used to characterize the stresses on orthogonal planes [38]. The center-point of Mohr's circle is the average of the two normal stresses, σ_x and σ_y. The radius of Mohr's circle is the maximum shear stress in the *x-y* plane and the maximum and minimum normal stresses along the *σ*-axis can be determined if the angle of rotation, θ, is known. For normal stresses, tension is positive, and compression negative [38].

The Mohr Theory of Brittle Failure utilizes the Mohr's circle representation for uniaxial tensile stresses and uniaxial compressive stresses in order to predict the failure of bodies made from brittle materials. This theory suggests that failure occurs when Mohr's Circle at a point in the body exceeds the envelope created by the two Mohr's circles for uniaxial tensile strength and uniaxial compression strength, shown in Figure 2.11 [42]. The left Mohr's circle (outlined in blue) is the limiting compression stress σ_c of the material. Likewise, the right circle (outlined in red) is the limiting tension stress σ_t. Failure lines are drawn tangent to these two circles and Mohr's theory suggests that failure will occur if and when the Mohr's circle for intermediate stress states in the center (outlined in black) falls on or outside these failure lines [41]. All intermediate stress states fall into one of the four cases categorized in Table 2.1 and each case defines the maximum allowable principal stress values to avoid failure in a brittle material [41].

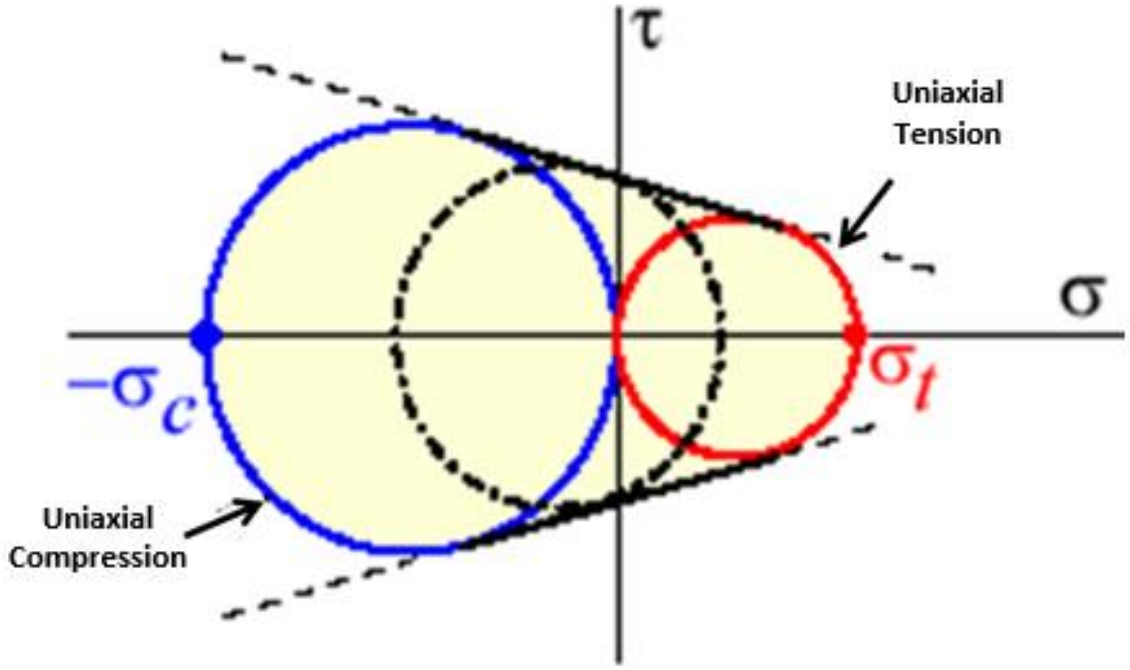

Figure 2.11: Mohr's Theory of Brittle Failure [42].

Table 2.1: Mohr's Theory of Brittle Fracture intermediate stress criterion [42].

Case	Stress Distribution	Principal Stresses	Criterion
1	Both in tension	$\sigma_1 > 0, \sigma_2 > 0$	$\sigma_1 < \sigma_t, \sigma_2 < \sigma_t$
2	Both in compression	$\sigma_1 < 0, \sigma_2 < 0$	$\sigma_1 > -\sigma_c, \sigma_2 > \sigma_c$
3	σ_1 in tension, σ_2 in compression	$\sigma_1 > 0, \sigma_2 < 0$	$\frac{\sigma_1}{\sigma_t} + \frac{\sigma_2}{-\sigma_c} < 1$
4	σ_1 in compression, σ_2 in tension	$\sigma_1 < 0, \sigma_2 > 0$	$\frac{\sigma_1}{-\sigma_c} + \frac{\sigma_2}{\sigma_t} < 1$

2.2.2 Material Properties

Rather than studying the effectiveness of port covers for use in integrated rocket ramjet (IRR) systems, the scope of this campaign focuses on a new material choice, alumina, for such port covers. In order to introduce the material choice, consider improvements in engines over the last century. Mid-1800's steam engines, used for water and rail transportation, employed simple cast iron parts while operating at temperatures around 100° C, the boiling point of water. As engine technology continued to mature, the internal combustion engine was introduced in automobiles and gas-turbine engines became practical for use in aircraft propulsion during World War II [38]. As increasing operating temperatures provide greater efficiency, current materials in jet engines withstand severe temperatures around 1800° C. Low-alloy and stainless steels as well as nickel and cobalt alloys were developed to better survive the increasing temperatures [39]. However, failures caused by creep, fatigue and corrosion heavily influenced engine development. The increased use of advanced engineering ceramic materials in the future is likely because they alleviate metal-specific failure modes and allow for superior temperature and corrosions resistance [38].

Ceramics used in high-stress applications, called engineering ceramics, exhibit several important advantages compared to traditionally used metals: high corrosion resistance, high melting temperatures, very stiff, relatively light weight and inexpensive. Although brittle, their tensile strength and fracture toughness makes the material suitable for use in high-stress applications. While yield strength is more relevant to ductile materials, the most important strength property for brittle materials is the ultimate tensile strength σ_{ut}, which is the highest engineering stress reached prior to fracture and recorded as 390 MPa for alumina [44]. The engineering fracture strength, σ_f, is equal to the force at fracture, even if this is not the highest force reached. Hence, for brittle materials, $\sigma_{ut} = \sigma_f$, whereas for ductile materials, σ_{ut} often exceeds σ_f [39].

Choice of material and its corresponding mode of fracture is highly dependent on its intended application. For frangible port covers used in IRR systems, a brittle material is not only preferred, but necessary for successful flight. As described in detail in Chapter 1, the most important part of IRR operation is the transition between rocket boost phase and ramjet phase. The transition process involves the solid rocket fuel being completely burned out to generate thrust, the port cover is fragmented and compressed air can now enter the combustion chamber for ramjet operation. It is imperative the frangible port cover fractures immediately to avoid any delay in that transition.

The main concern with brittle fracture is that failure can occur at stresses well below the material's yield strength due to the presence of a pre-existing flaw or crack. When the dominant stresses are compressive, the flaws tend to be pressed together which alleviates the premature-fracture effects characteristic of brittle materials. This is one reason that brittle materials can exhibit up to 4 times stronger compressive strength than in tensile strength [39].

Specific engineering ceramic properties for alumina are easily obtainable, one reason the material was chosen. A notable material property of alumina is a term well known in the materials science community: Poisson's Ratio. Poisson's ratio represents deformation of a material normal to the direction of loading [39]. For reference, Poisson's Ratio for a rubber band is 0.5, meaning it deforms the same amount any direction that it is stretched. Poisson's ratio for a cast iron skillet is between 0.21-0.26 [43]. At 0.22, alumina carries a similar deformation strength found in a cast iron skillet [44,43]. Young's modulus, E, is a stiffness measurement of the material under axial loading [39]. Ceramics exhibit relatively high elastic moduli, often higher than for many metals. Another reference material is a human femur bone, which has a Young's Modulus of 14 GPa [45]. At 370 GPa, the microstructure of alumina exhibits stiffness properties much higher than that of a human femur, but does not scratch the surface of a diamond which exhibits an enormous Young's Modulus of 1220 GPa [44,45,46].

2.2.3 Microstructure

Engineering ceramics, predominantly crystalline in microstructure, are often fairly simple compounds of metals with nonmetals such as oxygen, carbon, or nitrogen [38]. In solids, atoms and molecules are held together by primary chemical bonds of three kinds: ionic, covalent, and metallic [38]. Materials with covalent bonds include carbides, nitrides and oxides. Alumina, also known as aluminum oxide, is the metal aluminum covalently bonded with oxygen and its corresponding crystalline microstructure is illustrated in Figure 2.12 [44]. The hardness and brittleness of alumina can be attributed to the covalent bonds which are strongly directional and therefore resistive of deformation, rarely yielding to dislocation. Dislocation is defined as a linear irregularity within the crystal's atomic structure of a material that leads to plastic deformation and surface steps [31]. Slip is the process by which plastic deformation occurs due to dislocation motion. Due to the strength and directional nature of covalent bonding and the complex crystalline structures, slip does not often occur in ceramics [38].

There is often significant porosity in ceramic materials that promote macroscopic cracking and brittle failure generally occurs as a result of such macroscopic cracks growing and joining [38]. Often a time dependent process, the fracture behavior is dependent on the loading rate [38]. Grain boundaries in crystalline compounds are comparatively weaker than those found in metals, which further enhances the brittleness. Minimizing grain size, increasing temperature and reducing stress loads tend to mitigate crack initiation. Likewise, increasing grain size, elevated temperatures and higher stress loads favor crack propagation. Grain size charts are used to illustrate a range of grain refinement and coarsening scales for specific materials. Figure 2.14 is a grain size chart for the material carbide ranging from 1 micron to 10 microns [39].

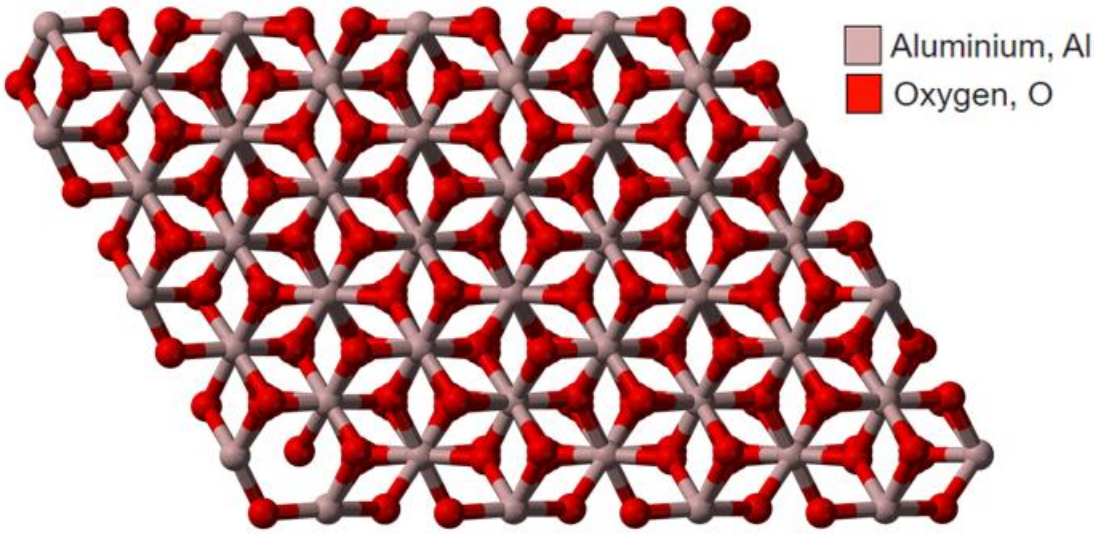

Figure 2.12: Ball and stick model of alumina crystal structure [39].

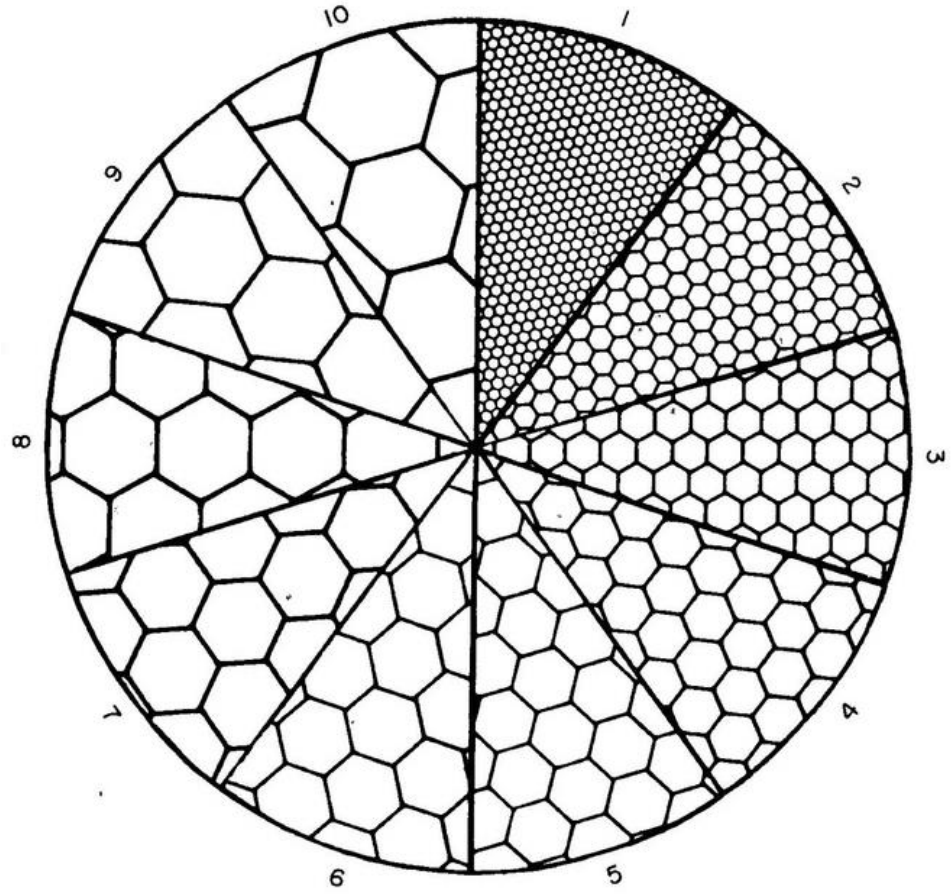

Figure 2.13: Grain size chart, 1-10 um at 1500X [39].

2.3 Manufacturing Processes

Ceramics are processed by binding the particles of a fine powder into a solid. Initial processing of an engineering ceramic composed of simple chemical compounds begins with obtaining the compound. If it is not already in this form, the compound is ground to a fine powder. The powder is then compacted into a mold of a specified shape by cold or hot pressing. Reasonably self-explanatory, cold pressing does not involve any additional heating to the shaping while hot pressing utilizes an elevated temperature to provide additional bonding of the powder. By lowering the porosity quotient, hot pressing techniques remove potential material weaknesses resulting in a denser, stronger part; however, cold pressing is necessary when a material's density must remain fixed [47].

Following hot or cold pressing, the ceramic is said to be in a green state and is the consistency of a piece of chalk. While in green state, the ceramic has very little strength and it is at this point that any necessary geometries are machined which would otherwise be difficult when the ceramic is at its final state. Example of geometries that are machined during green state include flat surfaces, holes, threads or dome faces such as those featured on the port covers used in this campaign.

After any necessary machining, the green piece is then sintered, which involves heating to around 70% of the material's absolute melting temperature. The particles fuse under the heat and form a solid with some degree of porosity, which is defined as the percentage of voids or empty spaces in a material. The sintering process is associated with a remarkable shrinkage of the material due to the considerable consolidation of the powder. Mechanical properties can be improved by minimizing the porosity. This can be further accomplished by reducing initial particle sizes or by applying additional pressure during the sintering phase [47].

Since the manufacturing process of ceramics, more specifically engineering ceramics, require several very specific machining components, it was obvious the manufacturing of the port covers needs to be outsourced. For most applications, parts made from alumina are relatively small and commonly available as rods, bearings, seals and electrical components. It was necessary to seek out manufacturers with the capability to custom produce a relatively large alumina port cover. To obtain a more comprehensive understanding of performance with minimal impact from vendor specific manufacturing processes, the port covers used in this experiment were fabricated and purchased from three external vendors: Ortech, Inc., Stanford Advanced Materials and Precision Ceramics, USA. Each vendor uses a slightly different chemical compound for the alumina and also minor variations in the manufacturing method, which results in the discrepancy of alumina mechanical properties as shown in Table 2.2 [48,49,50]. These values were provided from each manufacturer.

Ortech Advanced Ceramics, Inc. provided 10 port covers made of 99.5% alumina. As provided by the vendor the Ortech manufacturing process began with making a blank model with the powder alumina. A computer numerical control (CNC) lathe was used to machine the port cover to the specified geometry. This blank was fused into a solid through high temperature sintering followed by grinding to the specified geometry. As mentioned in previous sections, the main concern with brittle materials is that the presence of a flaw or crack can cause failure at stresses well below the material's yield strength. These flaws or cracks can be caused by machining techniques used during the manufacturing process. Microscopic surface images of the upstream dome face were taken to display the varying surface roughness details for each vendor.

Stanford Advanced Materials also provided 10 port covers made of 99.5% alumina. Stanford's manufacturing process, again provided by the vendor, began with pouring the alumina powder into the disc mounted rubber mold. This was followed by a cold isostatic press for 15 minutes under 185 MPA. A CNC lathe was used to trim the outer circle and two planes of the formed ceramic blank. The blanks were then carved to make the concave surface and control the size before shrinking. The port covers were then sintered for 285 hours under 1650° F, followed by heat preservation for 11 hours. The surface was grinded, then the convex shape and skirt were milled. The port cover was then chamfered, cleaning and vacuum packed for shipment.

The third vendor is Precision Ceramics which produced 99.7% alumina and 8 were purchased due to a more expensive price per part. Precision Ceramics began by putting powder in the mold and pressing it in to a highly compacted "green" billet. The consistency of this port cover at this stage is similar to that of pressed chalk. The green billet is then machined into the desired dimensions. At this point called green machining, the part is the correct geometry but ~20% bigger. The port covers are then sintered in the furnace where they shrink about 20%. An as-fired part is completely finished as this point. Upon inspection, Precision ceramics experienced shrinkage that caused the surface to be out of tolerance. This was corrected by diamond grinding the surface back to tolerance range.

Table 2.2: Alumina material properties provided by each manufacturer [48,49,50].

Property	Stanford Advanced Materials	Ortech, Inc.	Precision Ceramics
Alumina Content	99.5%	99.5%	99.7%
Density	3.89 g/cm³	3.90 g/cm³	3.90 g/cm³
Poisson's Ratio	0.22	0.22	0.22
Young's Modulus	370 GPa	370 GPa	350 GPa
Flexural Strength	≥300 MPa	379 MPa	390 MPa
Maximum Use Temperature	1500 °C	1750 °C	1650 °C
Vicker's Hardness	≥15 GPa	14.1 GPa	16 GPa

CHAPTER THREE
EXPERIMENTAL METHODOLOGY

3.1 Stress Analysis

As previously described in Chapter 2, the AFRL's finite element analysis (FEA) recommended the most efficient port cover geometry to be 6 mm thick throughout with a 45˚ dome angle, see Figure 3.1. Model thickness describes the distance between the top surface and bottom surface of the dome. Stress analysis results indicated that any increase or decrease in thickness would weaken the model and reduce the minimum safety factor. Dome angle describes the angle at which the dome face intercepts the outer support rim.

For brittle materials, crack propagation is likely to occur where there is a sharp change in geometry. The large number of stress concentration focused around the bolt holes in the AFRL model compromised the integrity of the port cover. In response to this observation, the model was redesigned slightly for this investigation. The bolt holes were removed and the oblong shape was adjusted to be a perfect circle. These modifications greatly decreased the price per part as well as altering the fracture mechanics such that the stress concentrations were now located at the point where the dome face meets the outer support rim. All other points of geometry were consistent with the original model, included the thickness, dome angle and use of fillets on the transition region from outer support rim to dome face.

In order to validate the recently altered port cover is capable of withstanding the same pressure loads as the original design, repeated stress analysis was necessary. Similar to the AFRL campaign, two software were used to validate the stress analysis results. The first repeated FEA method utilized Solidworks stress analysis tool [32]. The parameters set in place from AFRL were closely followed in order to provide relative results and the SolidWorks preset material properties for alumina were applied. An FEA mesh is defined as the network of elements and nodes that discretize a region. Refining the mesh density generally yields improved results, especially in areas of high stress gradients and/or geometric transition zones [41]. A blended curvature-based mesh was applied to the dome faces using the finest mesh density setting, an element growth ratio of 1.5 and an overall minimum safety factor of 1.5. SolidWorks mesh details and areas of interest are illustrated in Figure 3.2 (a).

The entire outer support rim is fixed and pressure loads are applied to the inner and outer dome faces. Several pressure variations were tested to confirm the structural integrity of the model; however, the results reported in the following sections represent the expected pressure loads an IRR port cover will experience at a maximum of 600 psi on the upstream

dome face and 14.5 psi representing atmospheric conditions on the downstream dome face. The pressure loads and fixtures details used in SolidWorks are pictured in Figure 3.3 (a).

Ansys Mechanical is the second stress analysis tool used to validate the port cover [51]. Two different alumina concentrations of 99.5% and 99.7% were evaluated in Ansys. Material properties for alumina of these concentrations were unspecified in Ansys, so the material property values provided from each manufacturer were entered manually. In order to follow the curvature-based mesh used in SolidWorks as closely as possible, the default meshing function was applied to the outer support rim and the face sizing mesh function was applied to the upstream and downstream dome faces. An element growth ratio of 1.5 and minimum safety factor of 1.5 were specified as well. SolidWorks mesh details and areas of interest are illustrated in Figure 3.2 (b). Again, the entire outer support rim is fixed and previously applied pressure loads on the inner and outer dome faces were repeated. Ansys pressure loads and fixtures details are pictured in Figure 3.3 (b).

Deflection is a measure of deformation a material experiences under a load [39]. Maximum deflection is the largest deformation a material will encounter before failure occurs. For brittle materials, such as alumina, little to no deformation will occur before fracture. The SolidWorks stress analysis resulted in a maximum deflection value of 13.1 μm. This miniscule value was anticipated and confirmed that the chosen material would perform as expected in the port cover application.

Under the same loading conditions used in the SolidWorks FEA, the Ansys stress analysis resulted in a maximum deflection value of 13.5 μm for the 99.5% alumina concentration model and 14.0 μm for the 99.7% alumina concentration. Figure 3.4 (a) and (b) show the maximum deflection plots for SolidWorks and Ansys stress analyses, respectively. Note that the maximum deflection values are located at the center of the dome face where the majority of the pressure forces are absorbed.

The maximum principal stress theory states that a material fails (or in this case fractures) when the largest principal stress exceeds the ultimate tensile strength, σ_{ut} [39]. With a 600psi pressure load on the upstream dome face and 14.5 psi pressure load on the downstream dome face, the maximum principal stress in the SolidWorks evaluation was 127.0 MPa. The SolidWorks maximum principal stress plots are pictured in Figure 3.5 (a). As provided by the manufacturers, the ultimate tensile stress of alumina is $\sigma_{ut} = 390\ MPa$. Since the maximum principal stress is well below the ultimate tensile strength of alumina, this indicates that the port cover won't fail from these pressure loads alone.

The Ansys stress analysis resulted in a maximum principal stress of 133.1 MPa for both 99.5% and 99.7% alumina concentrations. The Ansys maximum principal stress plots are pictured in Figure 3.5 (b). The FEA performed in both SolidWorks and Ansys verified that the model is suitable for the experimental phase.

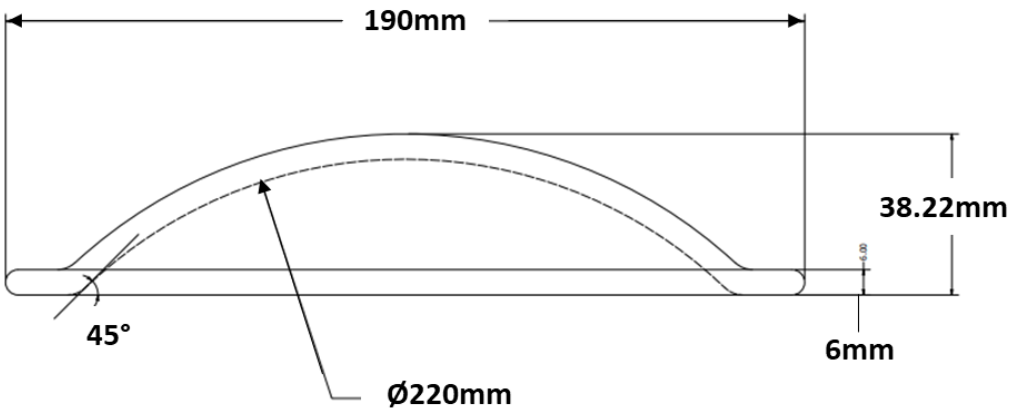

Figure 3.1: Port cover geometry, 6 mm thickness throughout (±0.1 mm) and 45° dome angle (± 0.25°).

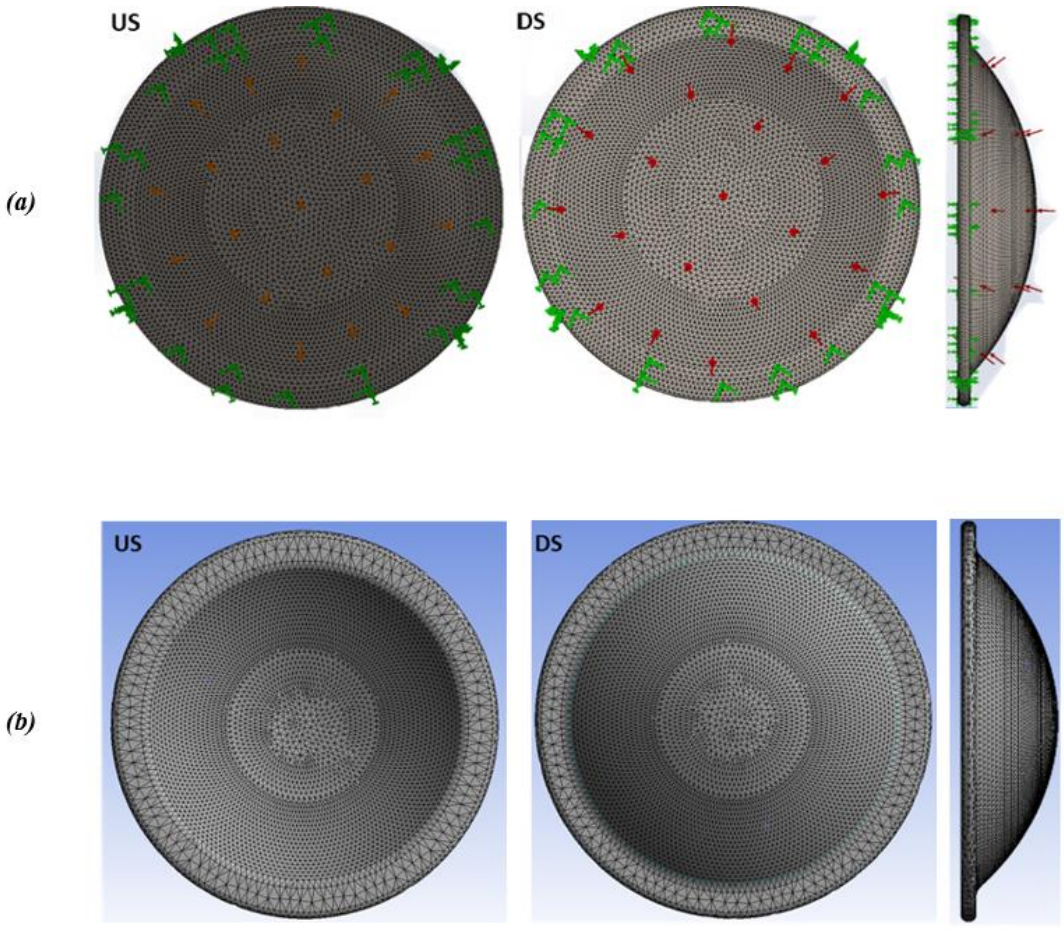

Figure 3.2: Stress analysis mesh details for (a) SolidWorks and (b) Ansys.

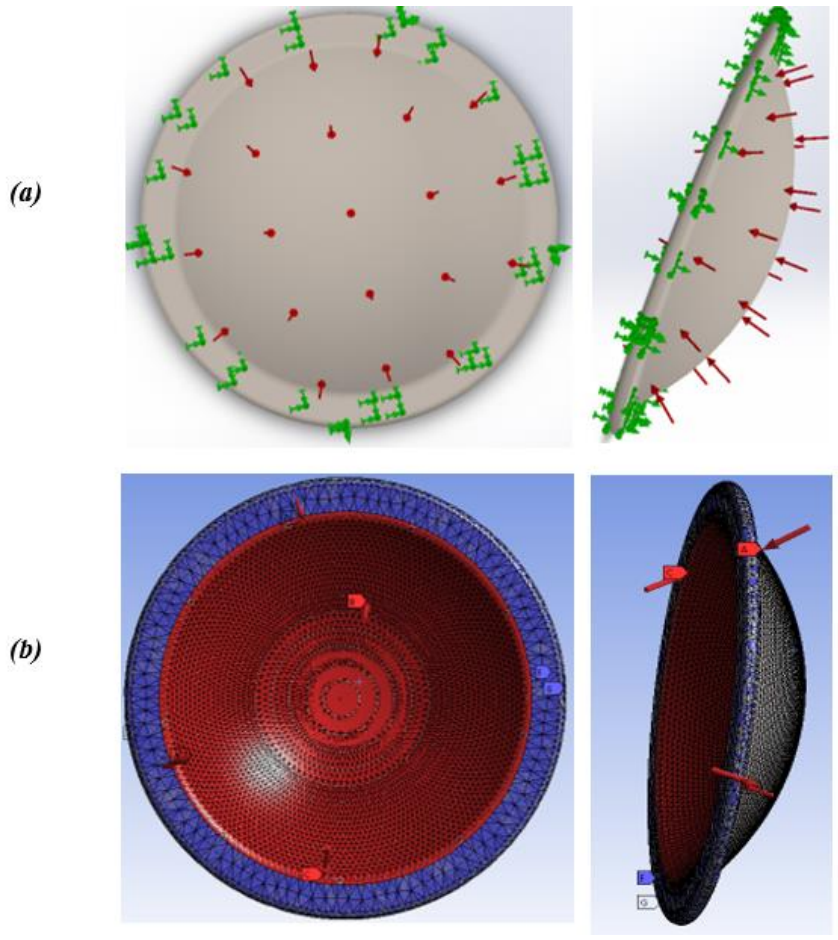

Figure 3.3: Stress analysis loads and fixtures details for (a) SolidWorks and (b) Ansys.

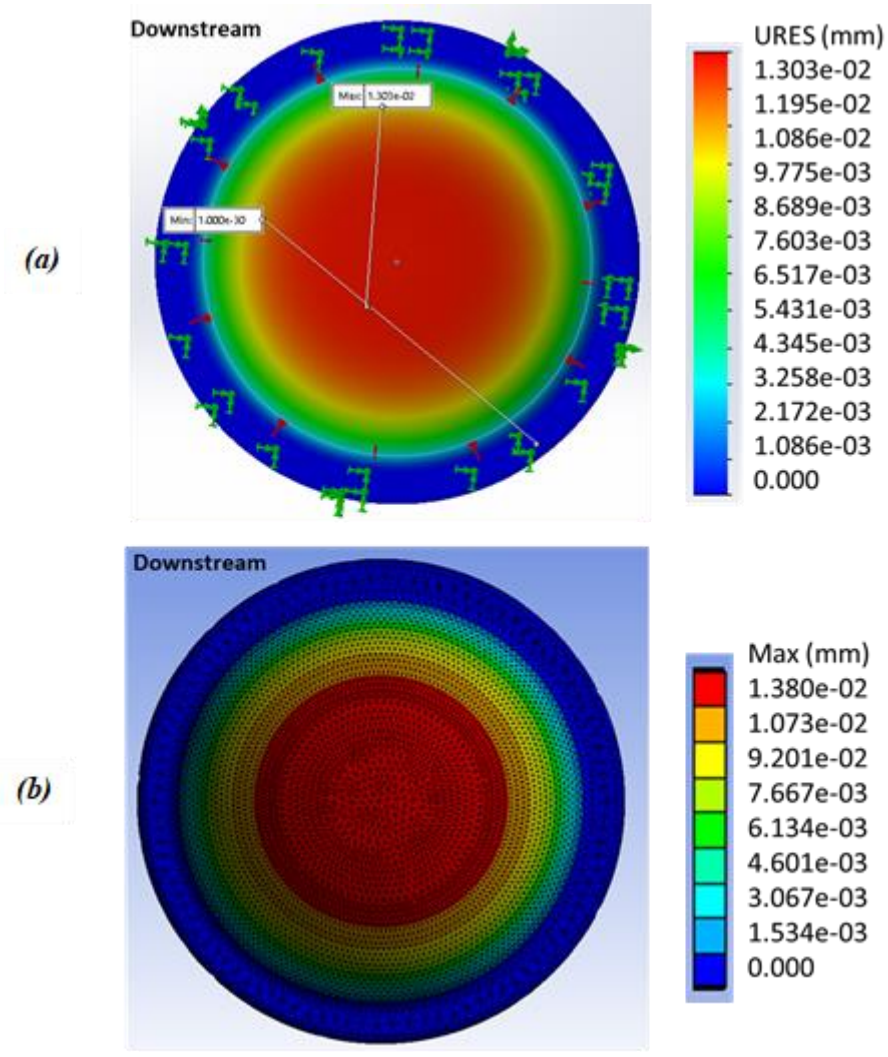

Figure 3.4: Maximum deflection stress analysis results for (a) SolidWorks and (b) Ansys

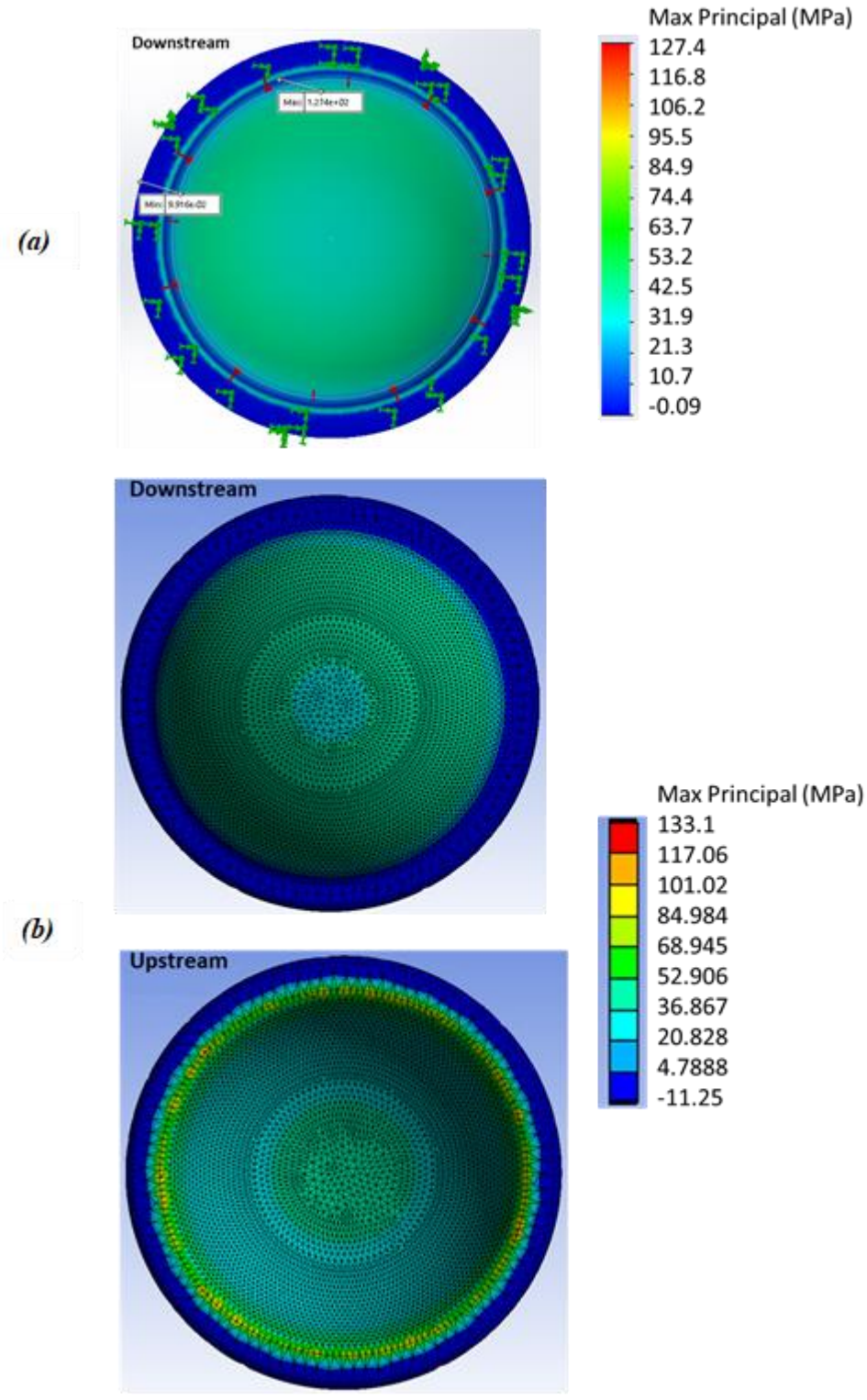

Figure 3.5: Maximum principal stress results for (a) SolidWorks and (b) Ansys.

3.2 High Pressure Chamber

Although FEA is a useful and necessary tool to determine initial parameters and expectations of a research model, realistic applications always introduce unforeseen limitations. It is necessary to perform experimental testing of the port cover to determine viability for use in IRR vehicles. The experimental phase of this research includes investigating the fracture mechanics by introducing a pressure load with the use of a high-pressure chamber, then intentionally fracturing the port cover while collecting various quantitative and qualitative data.

The facility used for the experimental campaign is a high-pressure chamber rated to provide up to 600 psi of static pressure designed and built at UTSI. The pressure vessel is made from schedule 40 304L 10" steel. The vessel is contained by two class 300 10" 304 stainless-steel slip-on flanges. The large outer flange is made from modified class 150 28" carbon steel and allows the facility to be capable of closed state operation, pictured in a CAD rendering in Figure 3.6 (a). It is preferred to utilize the open state operation to allow fracture of the port covers into true atmospheric conditions for enhanced optical access as well as minimizing the post-rupture fracturing that would likely occur on the fragments, risking inaccurate average fragment sizes. The two flanges holding the windows and port cover are modified class 300 10" carbon steel. The entire pressure chamber is supported by 4" square structural steel tubing. A side view of the pressure chamber is pictured in Figure 3.6 (b).

Once the port covers are installed in the pressure chamber, a control box is used remotely pressurize the chamber. Once the desired pressure is reached, the control box is switched over to trigger a mechanical fracturing mechanism, pictured in Figure 3.7. The design and fabrication of this fracture mechanism is a major research objective for this investigation. This fracture mechanism features an alloy steel striking rod encased in a 6061-aluminum frame [52] that is attached the front of the pressure chamber itself directly below the port cover. The striking rod is fired remotely using a pneumatic cylinder purchased from McMaster-Carr [53]. The purpose of the fracture mechanism is not to fully puncture the port cover, but rather initiate crack propagation on the downstream dome face. The high-pressure loads are responsible for fully fragmenting the port cover after the initial crack.

With the goal of minimizing additional impact fragmentation, an 8 ft x 7 ft frame made from 80/20 aluminum t-slot structural framing bars was placed directly in front of the pressure chamber. Sheets of 0.75-inch-thick hardwood subflooring were layered with 0.25-inch-thick rubber mats and 2-inch-thick foam insulation panels to catch the fragments and prevent further fragmentation upon impact. Wire mesh was added to the top of the support frame to prevent fragments from flying outside of the lab space. This is important when collecting and measuring the size of the fragments post-rupture as well as reconstructing the port cover. This precautionary set-up is pictured in Figure 3.8.

(a)

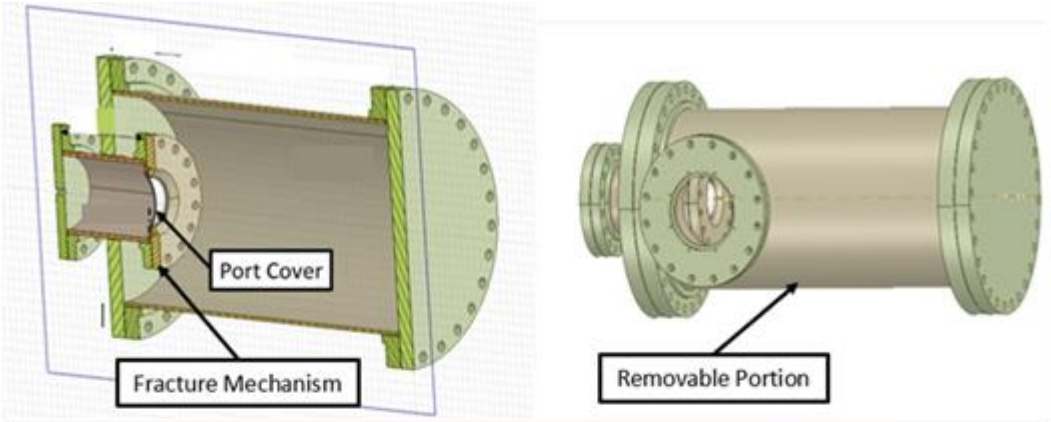

(b)

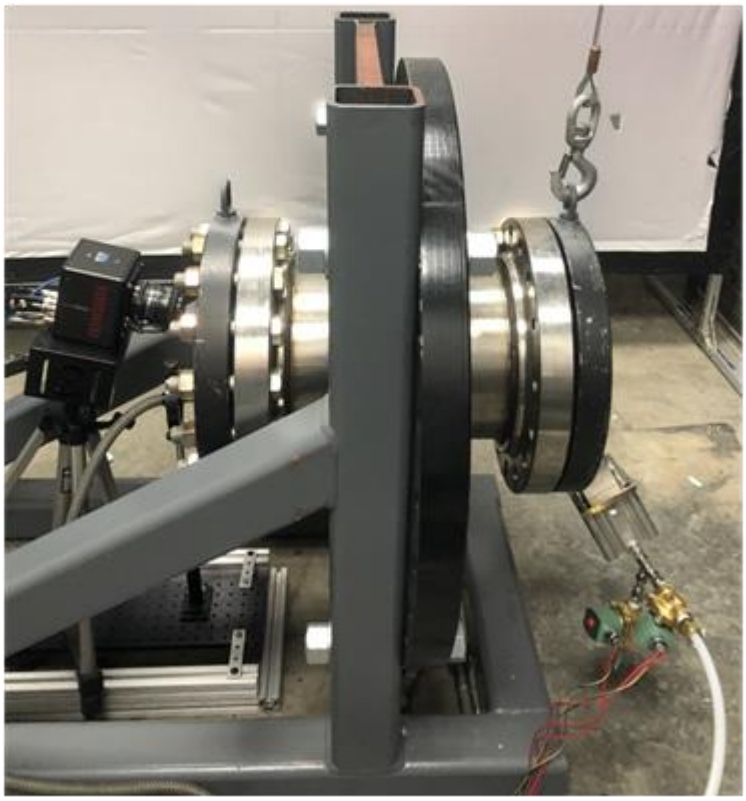

Figure 3.6: High- pressure chamber (a) CAD rendering and (b) facility.

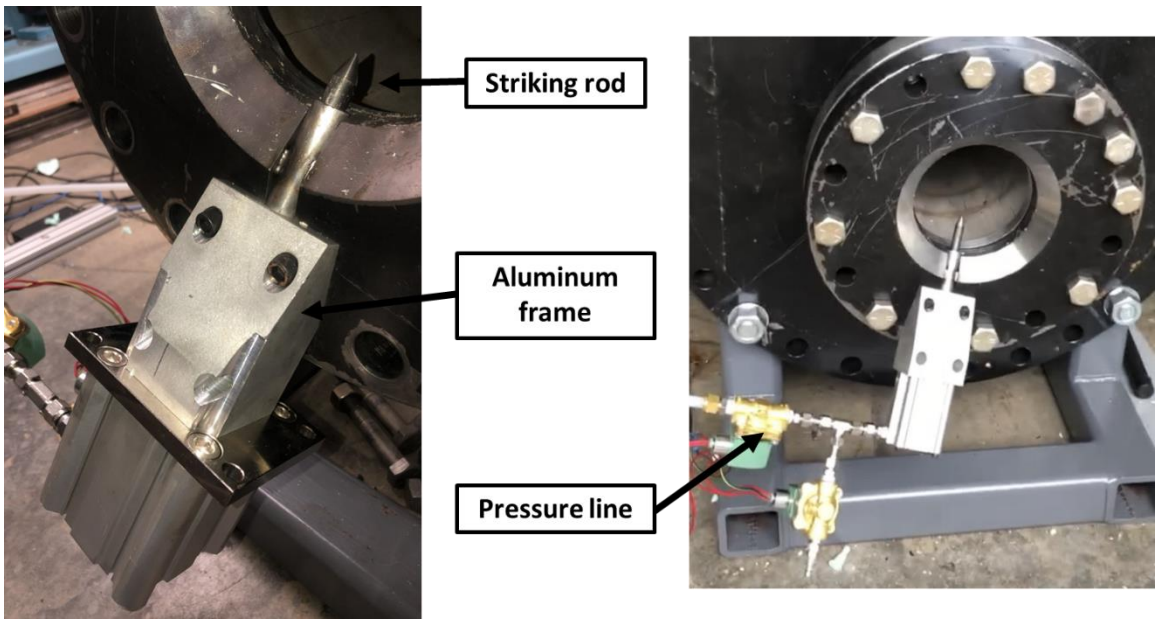

Figure 3.7: Fracture mechanism.

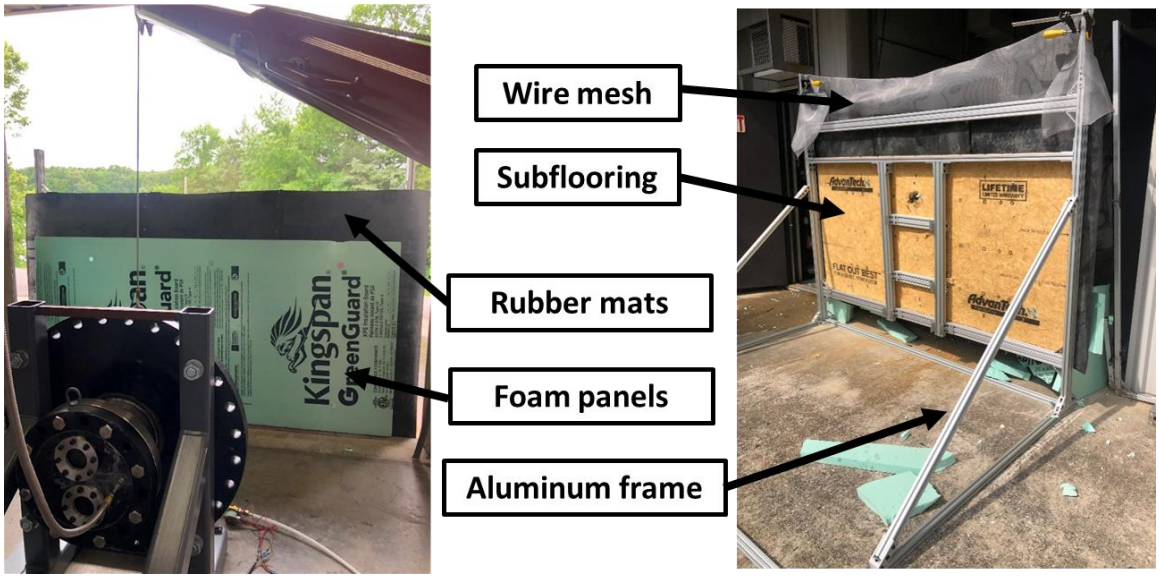

Figure 3.8: Frame used to catch fragments.

3.3 Diagnostic Techniques

In order to answer the research questions proposed in Chapter 1, it is necessary to study the port cover as it is fractured. High-speed camera diagnostic techniques capture images of the fragmentation process and subsequent fragments travelling through the atmosphere. The first camera is stationed perpendicular to the high-pressure chamber protected by a thick transparent acrylic barrier. In order to achieve maximum field of view for this diagnostic, the camera used is a Photron Mini UX100 pictured in Figure 3.9 (a) [54]. This camera model provides a 1280 x 1024-pixel image resolution with frame rates up to 4 kHz and achieves high light sensitivity through the utilization of micro-lenses. Due to its small sensor size and compact packaging, the Mini UX is suitable for operation with a range of optical systems in high shock and vibration environments, pertinent factors to these experiments. A Nikon Zoom-NIKKOR 24-85mm camera lens with an f/2.8-4d was attached to the camera, pictured in Figure 3.9 (b) [55].

The second high-speed camera is stationed directly behind the pressure chamber, directed into one of two small windows included in the pressure chamber design. One window is intended for optical access and the other is used for a light source. The high-speed camera used is a Photron Mini AX200, pictured in Figure 3.9 (c) [54]. In order to sync the triggering system for the light source and the first high-speed camera with this second high-speed camera, the frame rate was set to 8000 fps. At this frame rate, a pixel resolution of 1024x848 was obtained which provided ample field of view to see the entire port cover. The Mini AX features a mechanical shutter that allows for remote system calibration, which proved useful when setting the light source brightness. A Nikon NIKKOR 50mm camera lens with an f/1.4D was attached to the camera, pictured in Figure 3.9 (d) [55].

3.3.1 Initial Crack Propagation

The Griffith theory of brittle fracture, discussed in detail in Chapter 2, identifies the initial crack size as the determining factor for the entire fracture propagation pattern and ultimate failure of the material. Optical access to view the initial crack propagation as well as the entire rupture process is beneficial in understanding the fracture mechanics of the alumina port cover as well as the influence of the mechanical fracturing mechanism. With this in mind, the high-pressure chamber was designed with two small, circular windows are located on the back. The top window is used for camera access and the second window is used for a light source. The light source utilized in this diagnostic is the Fiber-Lite High Intensity Illuminator Series 180. To prevent air leaks, and consequentially a loss in pressure, the window frames are installed on the inside of the chamber so that the pressurized air acts to seal the windows very tightly. A top view of the diagram and the experimental setup is pictured in Figure 3.10 (a) and (b), respectively.



Figure 3.9: High-speed cameras and lenses used are the (a)Photron MiniUX100 high-speed camera, (b) Nikon 24-85mm zoom lens, (c) Photron MiniAX200 high-speed camera and (d) Nikon 50mm zoom lens [54,55].

3.3.2 Retroreflective Shadowgraphy

Retroreflective shadowgraphy is the second imaging technique utilizing a high-speed camera in these experiments due to its simplicity and ability to accommodate large-scale flow visualizations, which is necessary to maximize the number fragments travelling downstream in each image [56]. A field of view of 823 x 658 mm was obtained with this specific high-speed camera and experimental set up. The motivation behind the shadowgraphy diagnostic is to calculate fragment velocities and the following equipment was required: retroreflective screen, high-speed camera, LED light source, focusing lens and 45° rod mirror lens. The LED light source is aligned with a 75 mm focusing lens, which focuses the light to a small point. The point of light is reflected off of a 45° rod mirror lens towards the retroreflective screen. When the light travels back into the camera lens, the fragments passing through the illuminated region are imaged as shadows. In contrast to similar high-speed flow imaging, it is important to focus the camera on the retroreflective screen rather than the shadowgraph object. Figure 3.11 displays the retroreflective shadowgraphy diagram and Figure 3.12 displays the experimental set up in the pressure chamber facility.

3.3.3 Fragment Size Analysis

Since it is imperative that the port cover fragments are small enough that they do not damage the internal structure of the airbreathing vehicle, the average fragment size measurement is considered the most important data collected during these experiments. Each port cover is weighed before fracture, the fragments are manually recovered after fractur then the collected fragments are weighed in order to determine what percentage of the port cover was able to be recovered. The recovered fragments were photographed on a dark surface with a measuring tape for scale.

ImageJ, an image processing computer program [57], was utilized to find the average fragment size of each photograph with a measuring tape for scale, detailed in Figure 3.13. Using the Process tab, the image was converted to black and white by selecting Binary then Make Binary. Occasionally the binary conversion assigned the fragments to be black with a white background. Since the program counts white pixels as objects it is necessary to Invert the image located in the Edit tab. A straight line was drawn on the measuring tape from two lines indicating one inch. Using the Set Scale option located in the Analyze tab, the length of the previously drawn line is auto-filled with pixel count. Since the port cover geometry is given in metric units, the known distance of one inch is entered as 25.4 mm. The scale value of pixels/mm is calculated and the scale is set for that image. A rectangle is drawn around the fragments and Set Measurements located in the Analyze tab is used to choose which specific measurements ImageJ will report. For average fragment size measurements, area must be selected. Finally, Analyze Particles located under the Analyze tab is used to select Outlines from the Show: option. After pressing OK, the outlined image of every fragment that was counted and measured is displayed along with fragment count and corresponding fragment size and average fragment size in mm^2 units.

(a)

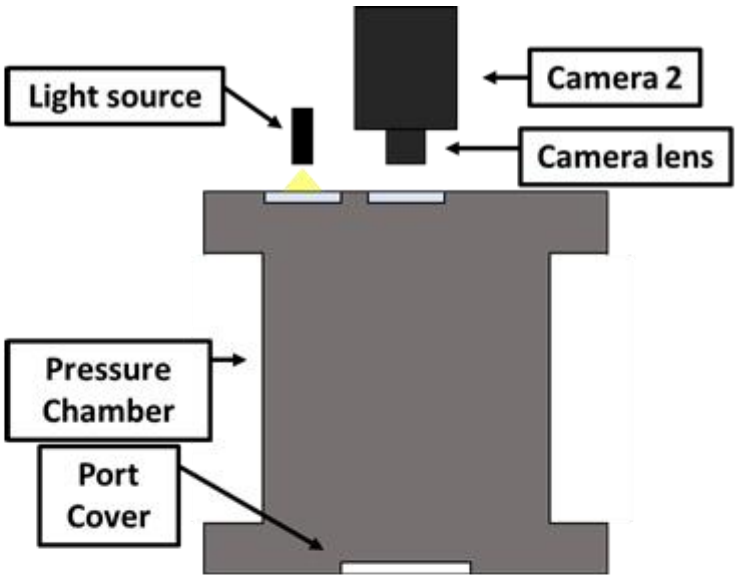

(b)

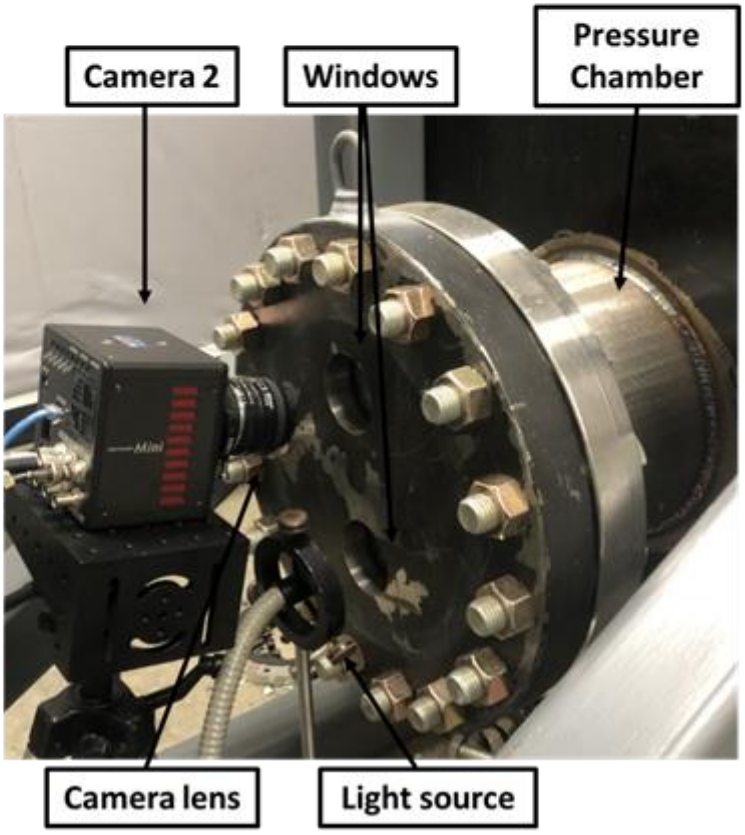

Figure 3.10: Initial crack propagation diagnostic (a) top view and (b)experimental setup.

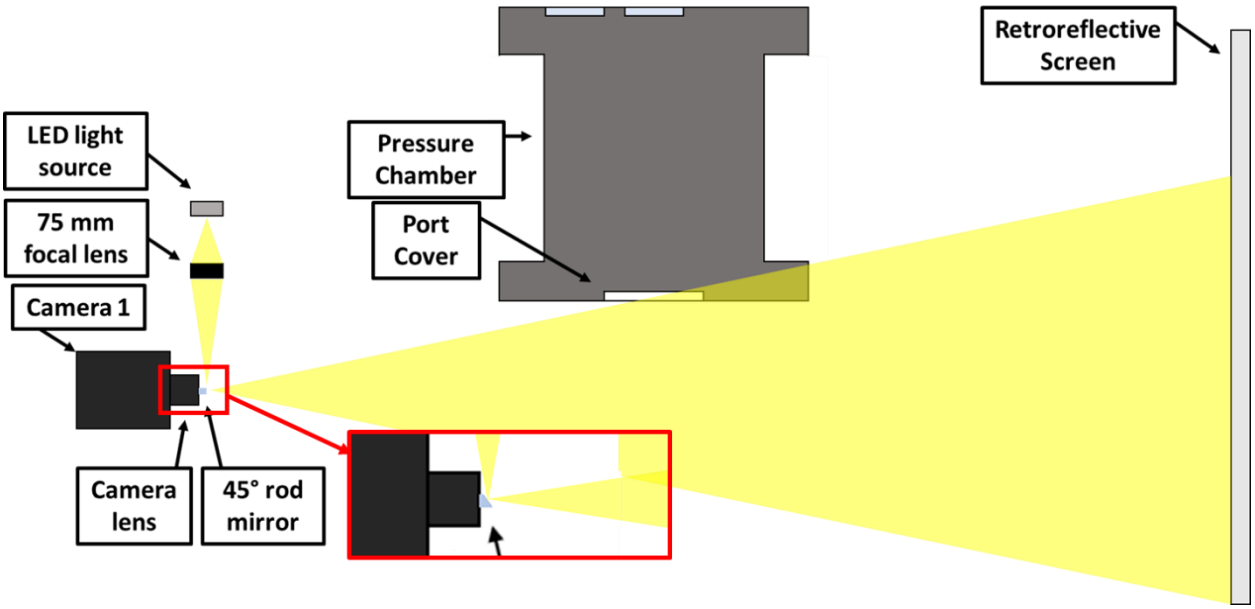

Figure 3.11: Retroreflective shadowgraphy diagram.

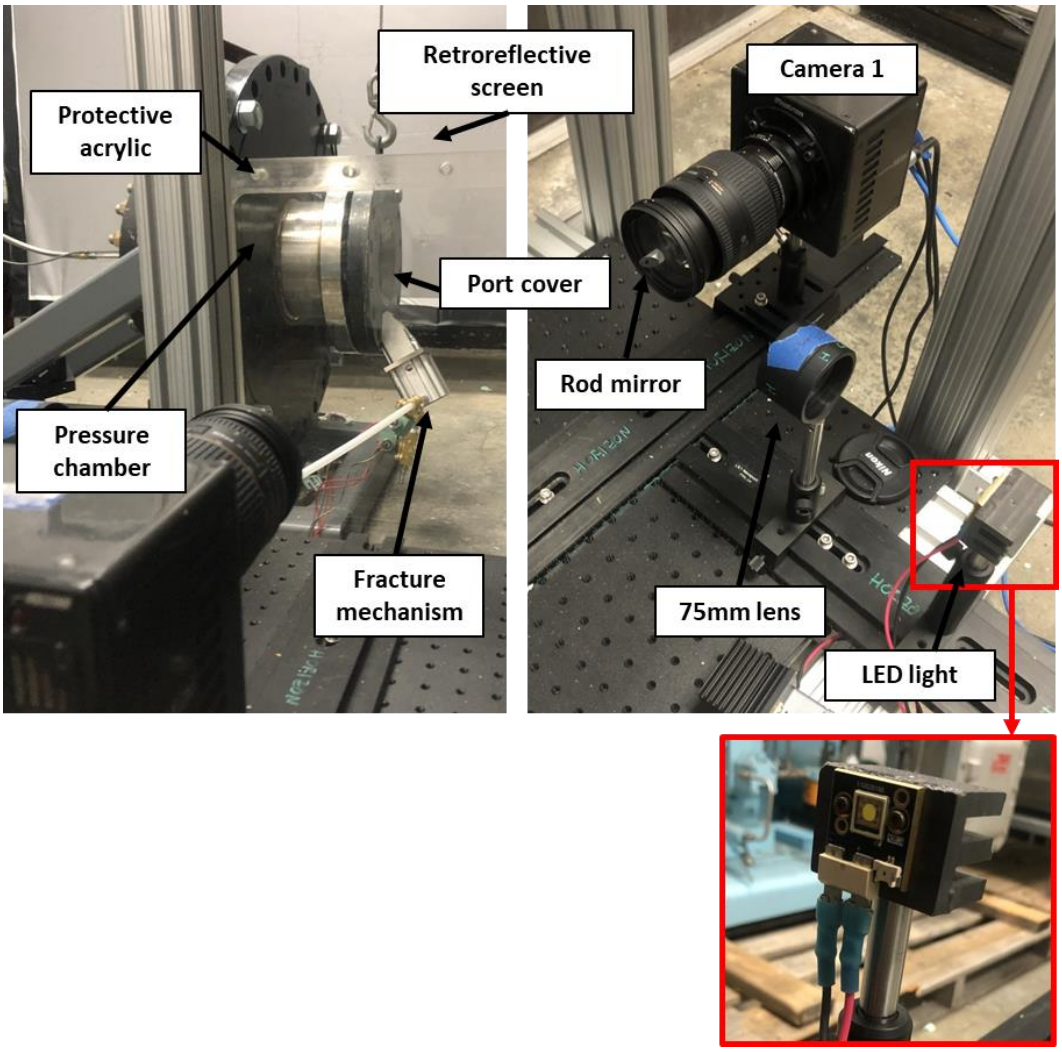

Figure 3.12: Retroreflective shadowgraphy experimental setup.

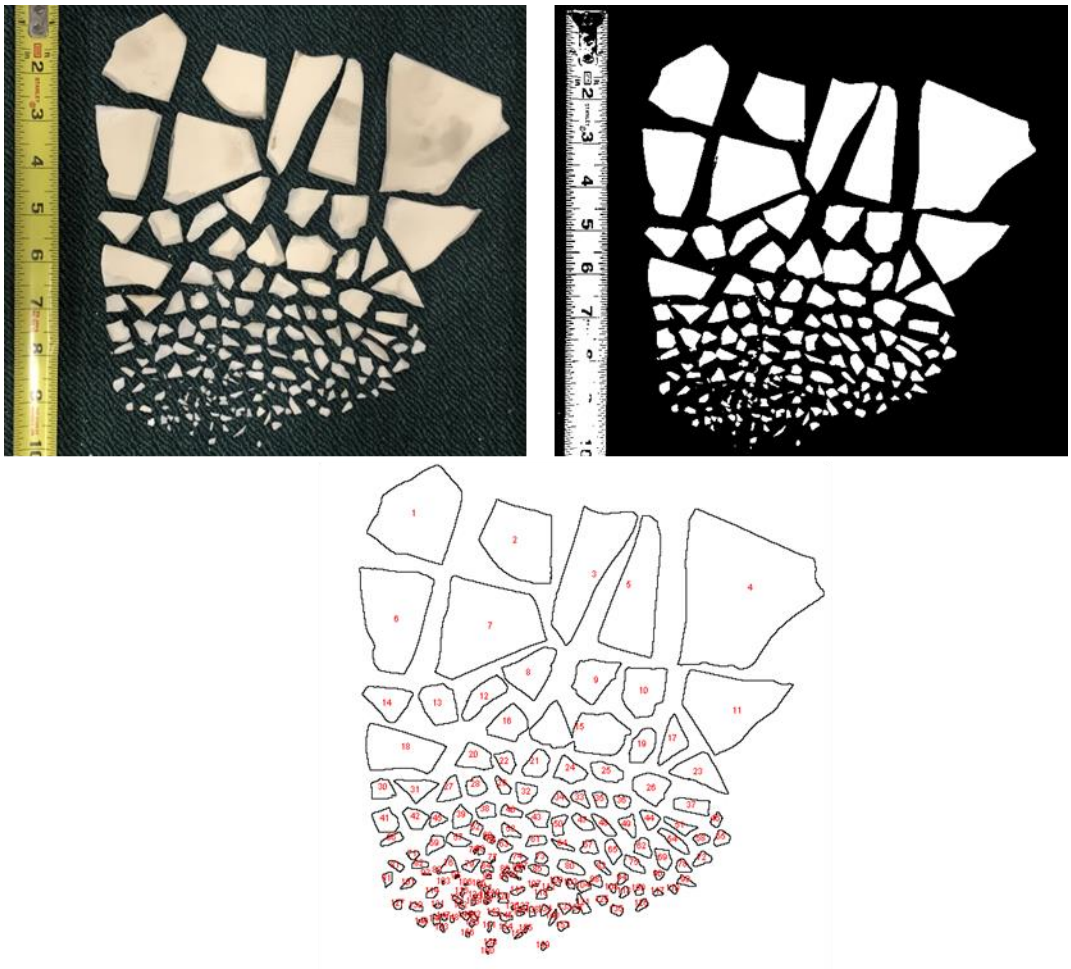

Figure 3.13: ImageJ technique to calculate fragment sizes.

CHAPTER FOUR

RESULTS

Port covers were purchased and tested from three external manufacturers: Ortech Advanced Ceramics, Inc., Stanford Advanced Materials and Precision Ceramics. When the port covers arrived, a preliminary maximum burst pressure test was performed for each manufacturer in order to compare experimental results to the numerical results. The goal of this preliminary test was to install the port cover in the pressure chamber, pressurize to 450 psi to ensure the port cover could withstand the maximum pressure loads that will be experienced in an IRR system, then initiate crack propagation on the port cover's downstream dome face using the mechanical fracture mechanism. During these tests the Ortech port covers burst at 165 psi on average, the Stanford port covers burst at 220 psi on average and the Precision Ceramics port covers were the only port covers that withstood the full 450 psi.

As previously mentioned in Chapter 2, the main concern with brittle materials is that failure can occur at stresses well below the material's yield strength in the presence of a pre-existing crack or flaw. These flaws or cracks can be caused by machining techniques used during the manufacturing process. When the port covers arrived, microscopic surface images of the upstream dome face were taken to display the varying surface roughness details for each vendor. The Ortech, Stanford and Precision Ceramics port covers and surface roughness effects from the manufacturing process are pictured in Figure 4.1 (a), (b) and (c), respectively. For the initial phase of this project, the port covers were purchased as-fired with no additional surface refinement. During the sintering phase, the Precision Ceramics port cover experienced shrinkage outside of the expected dimension tolerances. The piece was diamond-grinded to correct the tolerance, hence providing a smoother, more uniform surface finish. Although Ortech, Inc. and Stanford provided 99.5% alumina concentration port covers while Precision provided 99.7% alumina concentration, the FEA stress analysis showed negligible difference between the two concentrations. However, it is likely that the visible pre-existing flaws on the dome surface contribute heavily to the premature failures during the maximum burst pressure tests.

Another preliminary test was performed called the flip test. The pressure chamber was designed so that the port covers can be installed so that either of the dome faces can encounter high pressure, visualized from a top view in Figure 4.2 (a) and (b). It is well known that brittle materials are stronger in compression than in tension and the goal of this preliminary test was to flip the port cover orientation to validate the port cover's compressive strength from each manufacturer by pressurizing, again, to 450 psi. After the port cover withstood the 450 psi, the next steps in the flip test were to relieve the pressure, remove the port cover, re-install it in the normal orientation, re-pressurize to 130 psi and finally initiate crack propagation on the downstream dome face using the mechanical fracture mechanism. The 130 psi is the expected pressure a port cover will encounter during flight.

Although the flip test results did exceed the maximum burst pressures while under tension, the Ortech port cover under compression burst at 290 psi, pictured in Figure 4.2 (a), the Stanford port cover burst at 375 psi, pictured in Figure 4.3 (b), and the Precision port cover, again, was able to withstand the full 450 psi. The images were captured with the initial crack propagation camera diagnostic located directly behind the pressure chamber. Two observations can be made from these images, the first being the shearing fracture mode characteristic of brittle materials under compressive stress. The second observation is that fracture does occur on the geometric region where the dome face meets the flat outer support rim, which agrees well with the stress concentrations found from FEA.

Continuing with the second part of the flip test, the pressurized air was released from the chamber and the Precision port cover was removed then re-installed in the normal orientation. Finally, the port cover was re-pressurized to 130 psi. At the maximum burst pressure of 450 psi, the Precision port covers were successfully fractured with the mechanical fracturing system. However, while under the lower pressure of 130 psi, the Precision port covers were not able to be fractured. The sharpened steel fracturing rod was deformed several times without making a dent in the port cover, pictured in Figure 4.3 (a). The steel rod was replaced by a sharpened carbide tip, which was shattered by the port cover during the first attempt, pictured in Figure 4.4 (b). Finally, a sharpened diamond tip was installed. Although it did make a small chip in the port cover, pictured in Figure 4.3 (c), it failed to fully fragment the port cover. Because of this failure to fracture the port cover, the remainder of this chapter contains only results for port covers manufactured by Ortech and Stanford.

The experimental test matrix in Table 4.1 displays the results from each of the experimental methods utilized during this campaign. Meaningful average fragment size data and average fragment velocity data with corresponding standard deviations are reported for three port cover cases from each manufacturer. Each port cover was pressurized to 130 psi and intentionally fractured.

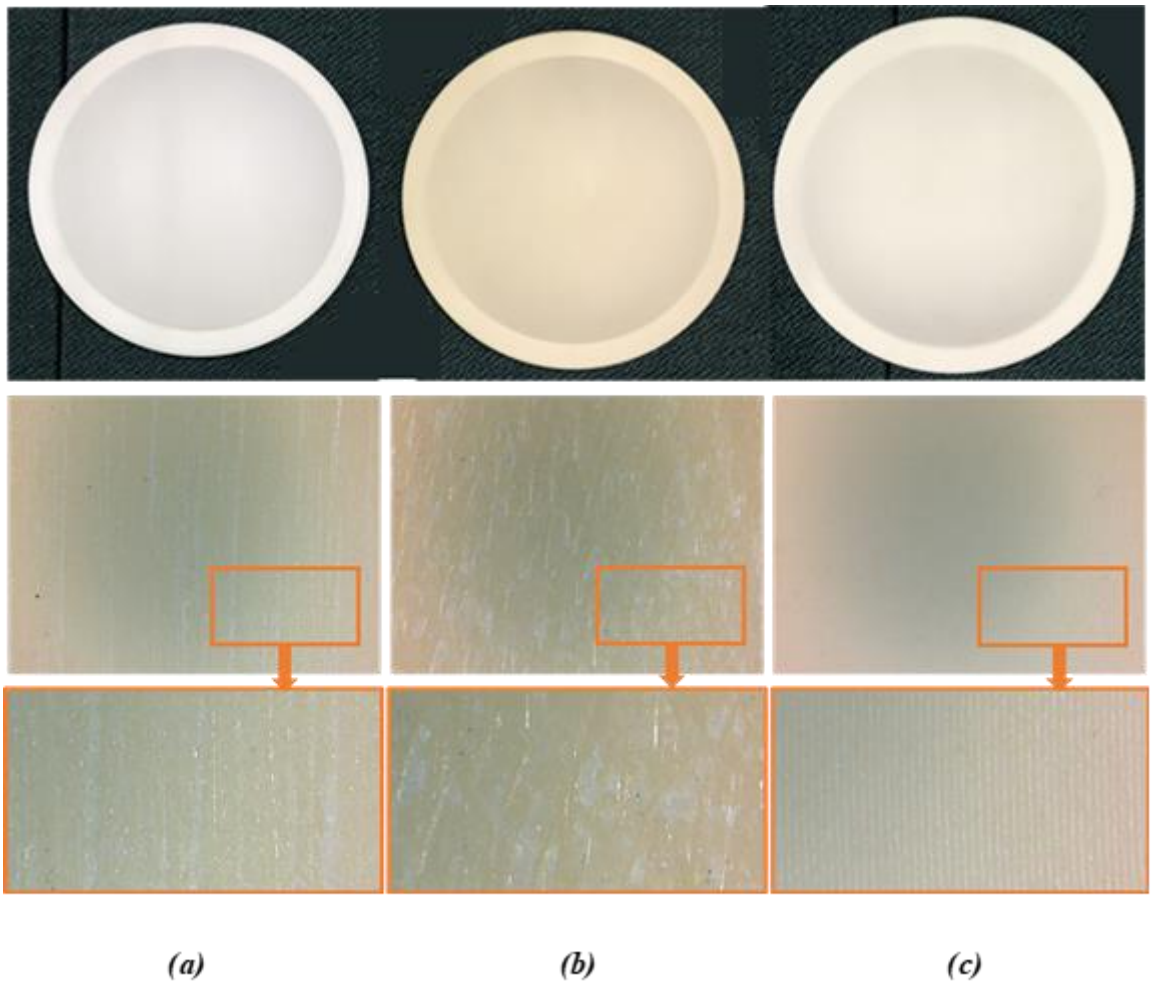

Figure 4.1: Port covers and microscopic surface roughness images (200x magnification) of dome face from each manufacturer: (a) Ortech Inc., (b) Stanford Advanced Materials and (c) Precision Ceramics.

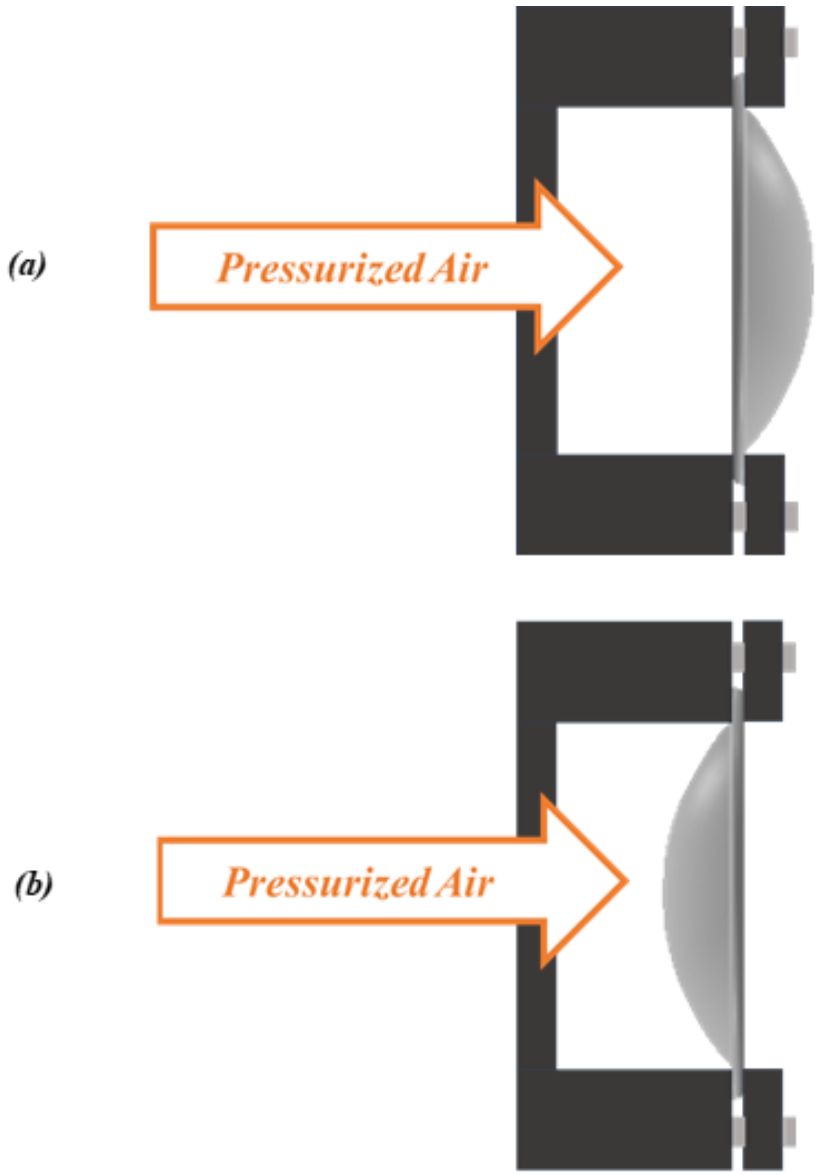

Figure 4.2: Port cover orientation (a) normal and (b) flip test.

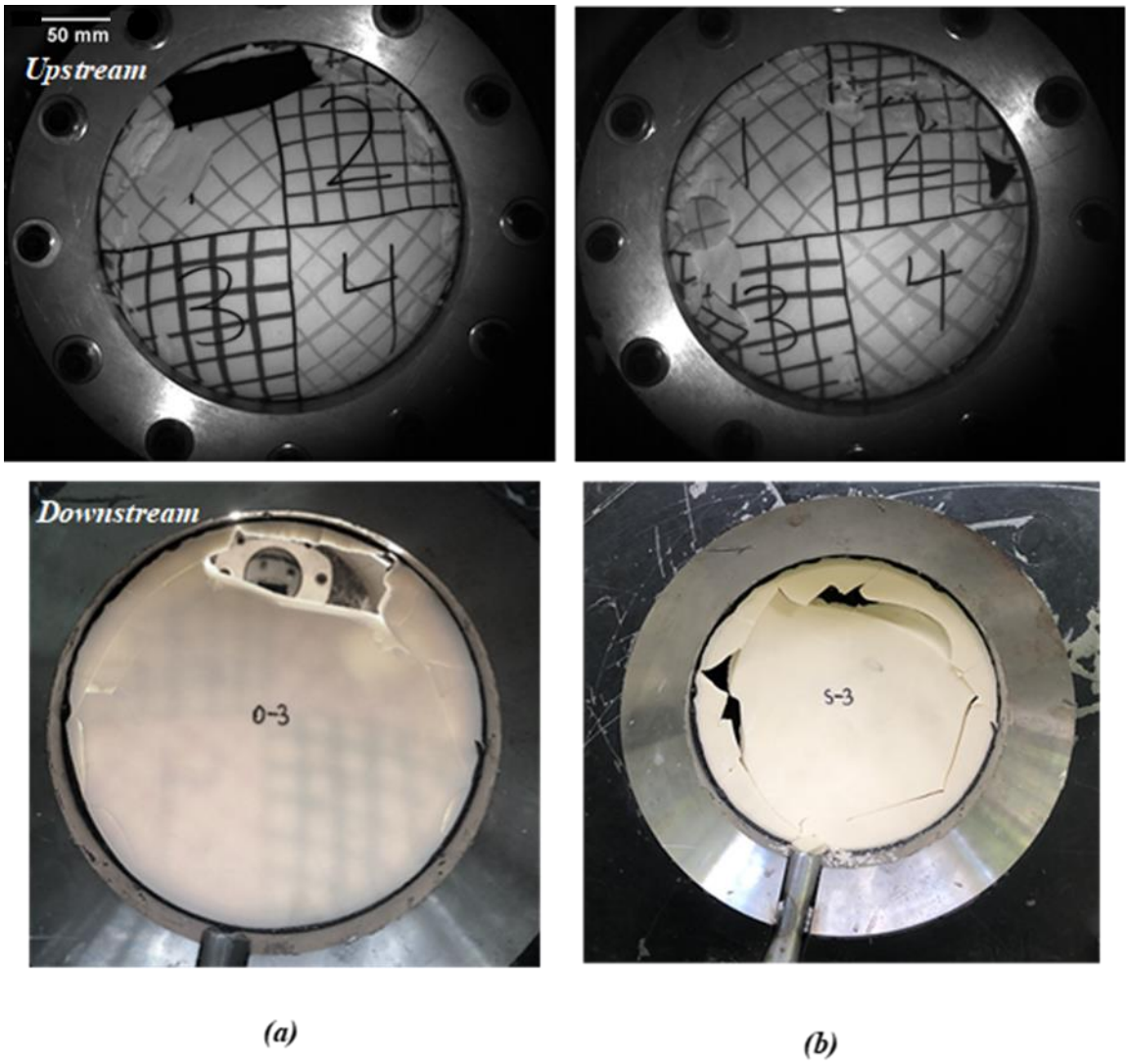

Figure 4.3: Flip test images with high-speed camera (upstream) and post rupture images (downstream) for (a) Ortech and (b) Stanford.

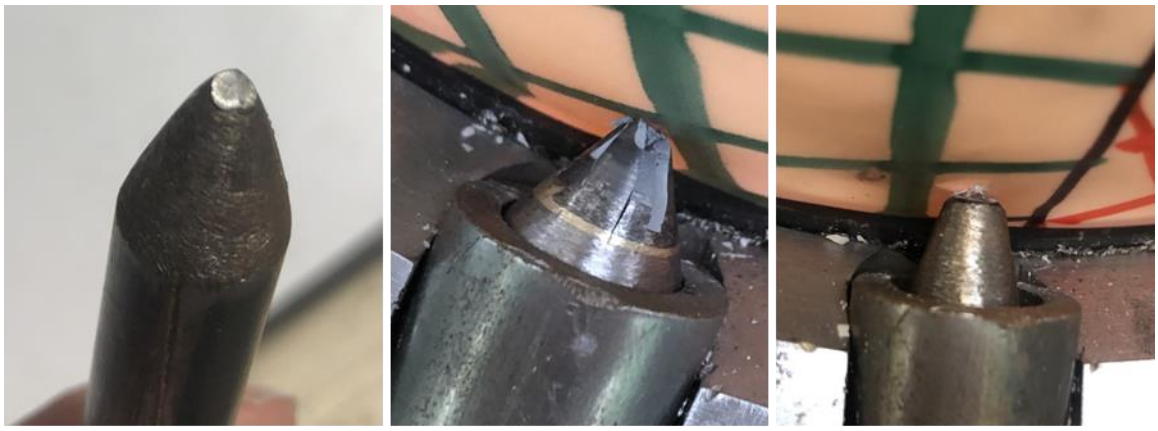

(a) *(b)* *(c)*

Figure 4.4: Fracture initiation failures: (a) deformed steel fracture rod (b) shattered carbide tip fracture rod (c) chipped diamond tip fracture rod.

Table 4.1: Experimental test matrix results.

Case	Burst Pressure (psi)	Avg. Fragment Size (mm^2)	Fragment Size St. Dev. (mm^2)	Avg. Velocity (m/s)	Velocity St. Dev. (m/s)
Ortech 1	130.1	126.87	373.50	112.06	21.00
Ortech 2	131.0	163.28	541.76	114.86	24.27
Ortech 3	131.1	160.29	625.78	78.79	47.07
Stanford 1	130.2	134.43	735.25	103.65	19.69
Stanford 2	130.5	133.42	532.21	115.91	29.09
Stanford 3	130.1	114.61	424.99	118.71	25.60

4.1 Initial Crack Propagation

Two windows located in the back of the pressure chamber allow for optical access of the initial crack propagation pattern of the port cover as it fractures. Results from this high-speed camera diagnostic emphasized the influence that the mechanical fracturing mechanism has on the entire fracture pattern and mechanics of the port cover. Again, it should be noted that the fracturing mechanism triggers a fracturing rod to strike the downstream dome of the port cover. The rod does not puncture the port cover, but rather initiates a crack that compromises the integrity and the high-pressure air in the chamber is responsible for the subsequent total fracture.

Each port cover is pressurized to 130 psi then the fracturing mechanism is triggered Sequential images of the fracture pattern details for Ortech and Stanford are pictured in Figure 4.5 and 4.6, respectively. The images are taken at 8 kHz and the time ranges from 0.0 to 2.25 milliseconds. The location of the fracture mechanism for Ortech cases 1 and 2 is in the bottom right corner of the port cover, and slightly left of center in the bottom middle for Ortech case 3. The location of the fracture mechanism is in the bottom right corner of the port cover for all three Stanford cases.

Several observations can be made from these images, one being the concentration of large fragments in the center of the dome face. From the FEA stress analysis, it is seen that the maximum principal stress concentrations are located where the outer support rim transitions to the dome face. The initial crack propagation images agree well with those results such that the fracturing mechanism influences the facture pattern on the dome face and results in large fragments, while the high-pressure loads fracture the port cover around the rim into very small, desirable fragments.

Another qualitative observation is that the location of the fracture mechanism on the port cover generally produced smaller fragments in that region. Since the initial crack propagation camera diagnostic is set up behind the port cover, the regions are effectively mirrored in these upstream images compared to the downstream images. The quadrant designated as 3 is the location of the fracturing mechanism. During port cover reconstruction, quadrant 3 generally had smaller fragments than quadrant 1,2 and 4.

These images also provide a size and shape estimate of the fragments, notably the very large fragments. This allows a comparison between some collected fragments that can be easily identified in these images. This is useful in determining if the precautionary frame used to catch the fragments actually works to minimize additional fracturing upon impact. A final observation worth mentioning is the characteristic fracture mode of a brittle material under tensile loading. Recall the flip test orientation tested port covers under compressive loading and resulted in shear failure. The flip test fracture high-speed images displayed the top layers of the dome face flaking away. The fracture mode in this test feature uniform, clean breaks in the direction of the tensile loading.

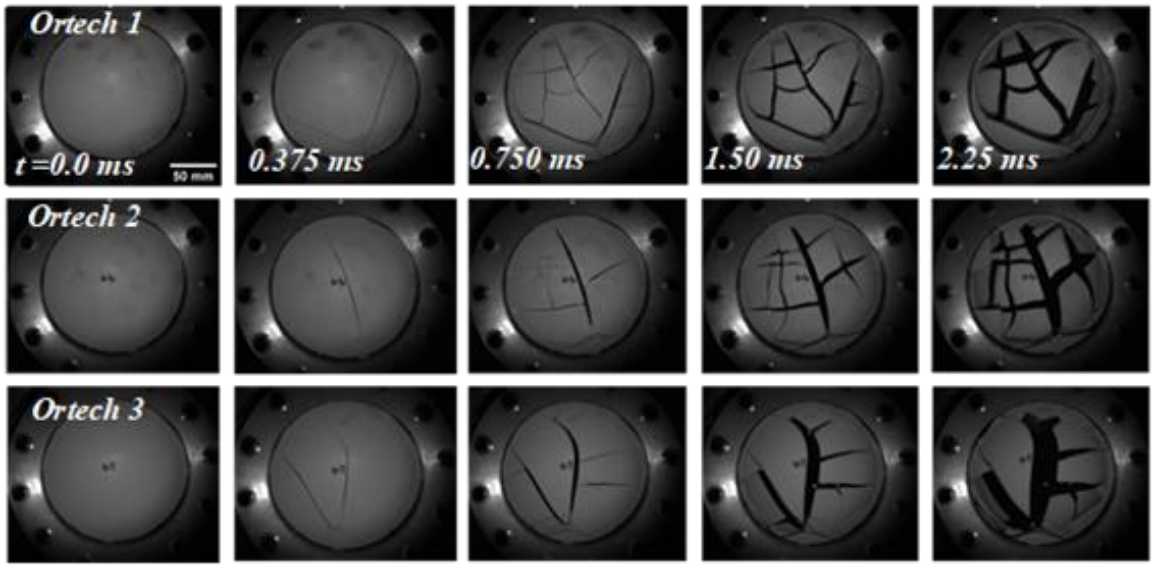

Figure 4.5: Ortech initial crack propagation high-speed images.

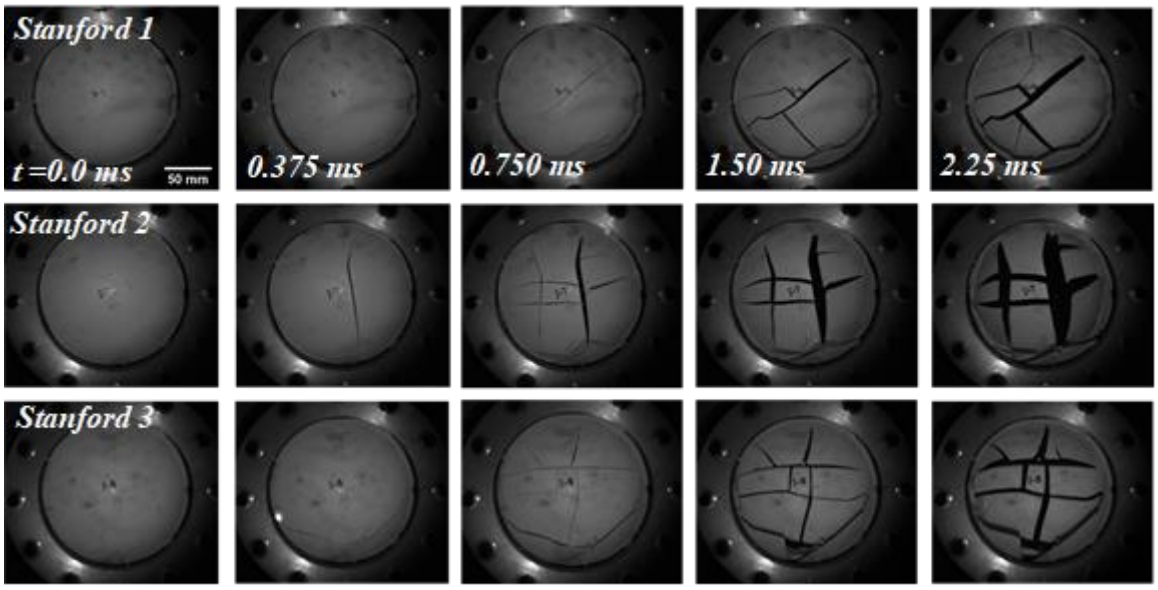

Figure 4.6: Stanford initial crack propagation high-speed images.

4.2 Fragment Velocity Analysis

A retroreflective shadowgraphy imaging technique is used to visualize the motion of the fragments and surrounding air. The average fragment velocity is calculated by analyzing sequential shadowgraphy images of the port cover rupturing and the fragments travelling downstream, which appear as shadows on camera. By analyzing the shifting x-position of the fragments as they travel downstream and recording the time lapse between each image, velocity was calculated for each port cover using the following well-known equation [58]:

$$\frac{x_2 - x_1}{t_2 - t_1} = \frac{\Delta x}{\Delta t} = velocity \qquad \textbf{(5)}$$

Upon fracture, the port cover fragments do not travel exclusively in the x-direction. Due to the dome geometry, as the fragments travel downstream in the x-direction, they also spread and travel at a 45° angle in the y- and z-directions. The out-of-plane motion coupled with rotational effects cause difficulties in measuring each individual fragment velocity. Instead, a reference line was used to analyze the x-position of the selected fragments.

The selected fragments are three front-running fragments from each port cover. Recall from the initial crack propagation data that the larger fragments are located in the center of the dome face. In the retroreflective shadowgraphy images, these larger fragments in the center of the dome face tended to be the front-running fragments because they are travelling in a mostly x-direction. The high-pressure chamber is not yet capable of providing dry air, so when the high-pressure, wet air enters the shadowgraphy images it is seen as a large shadow that effectively hides the fragments. The first thirty frames are visible and the velocity calculations are derived from those.

The reference line is placed at the leading edge of each fragment and adjusted frame by frame to record each x-position of the fragment in pixels. The retroreflective shadowgraphy technique requires the high-speed camera to be focused on the retroreflective screen rather than the shadowgraph object. A scaling card of a known length is placed on the retroreflective screen in order to convert from pixels to millimeters. The velocities between the first 30 frames were averaged to obtain an average fragment velocity for each port cover and ultimately for each vendor.

A total of six port covers were tested, three from Ortech and three from Stanford. Figures 4.4 and 4.5 display shadowgraphy images of the Ortech and Stanford case 1, 2 and 3 port cover fracture evolution, respectively. It should be noted that the bright white spot in the center of the images is a reflection caused by the protective acrylic barrier used to protect the high-speed camera equipment from the port cover fragments. The pressure chamber flange can be seen in the first frame. These images were taken at 4 kHz and the time ranges from 0 to 4 milliseconds.

From these calculations, the Ortech case 1 average fragment velocity is 112.06 m/s with a standard deviation of 21.00 m/s. The Ortech 2 average fragment velocity is 114.86 m/s with a standard deviation of 24.27 m/s and Ortech case 3 average fragment velocity was calculated to be 78.79 m/s with a standard deviation of 47.07 m/s. The Stanford case 1 average fragment velocity is 103.65 m/s with a standard deviation of 19.69 m/s. The Stanford 2 average fragment velocity is 115.91 m/s with a standard deviation of 29.09 m/s and Stanford case 3 average fragment velocity was calculated to be 118.71 m/s with a standard deviation of 25.60 m/s. Ortech port cover's average fragment velocity was calculated to be 101.9 m/s and Stanford was calculated to be 112.8 m/s.

An observation from the shadowgraphy images is the large fragment travelling downstream from the Ortech 3 port cover. This is one of the front-running fragments used in the calculations and explains the slower average fragment velocity for the Ortech 3 port cover. The same issue occurs for Stanford 1, in that the average fragment velocity is noticeably smaller for Stanford 1 because one of the frontrunning fragments that was chosen for velocity analysis is a very large fragment.

With the two-dimensional retroreflective shadowgraphy technique, diverging light can make the fragment can appear to be larger and slower when it is travelling closer to the camera or it can appear to be smaller and faster when it is travelling farther away from the camera. Considering this uncertainty, an experiment was conducted to measure the percent error of velocities as a function of depth. A scaling card was placed in three locations relative to the port cover, the left edge closest to the high-speed camera, the center and the right edge closest to the retroreflective screen. At each depth, images were taken of the scaling card "travelling" downstream the exact same distances from the port cover. Using the same reference line velocity calculations, a 0.6% error was found to be present in the velocity of the scaling card closest to the camera compared to the velocity of the scaling card farthest from the camera.

From a statistical point of view, because the field of view was effectively cut in half by the intrusion of wet air in the images, the small sample size can present uncertainties in these velocity measurements. However, following the diverging light experiment, as the fragments travel further downstream it is likely they will continue on the out of-plane path and there will be an even larger error present in the velocity measurements.

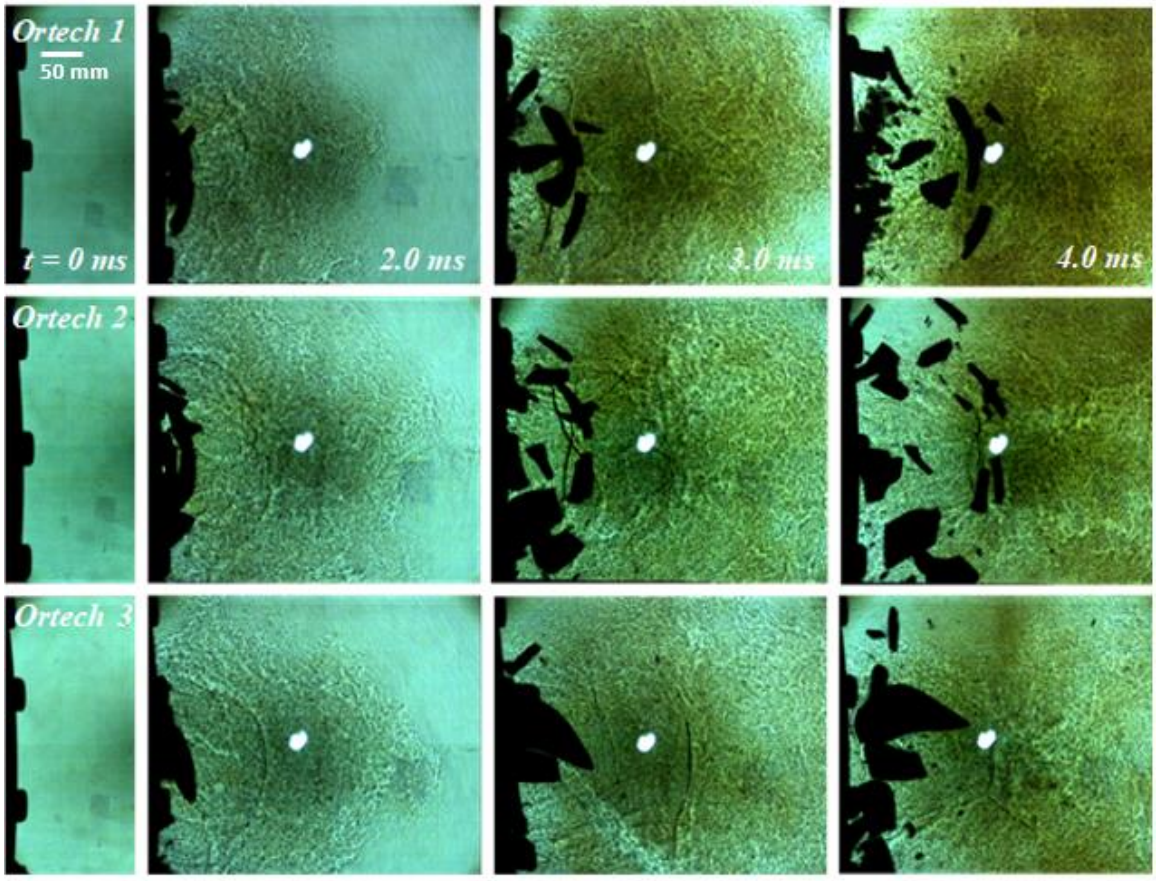

Figure 4.7: Ortech shadowgraphy images.

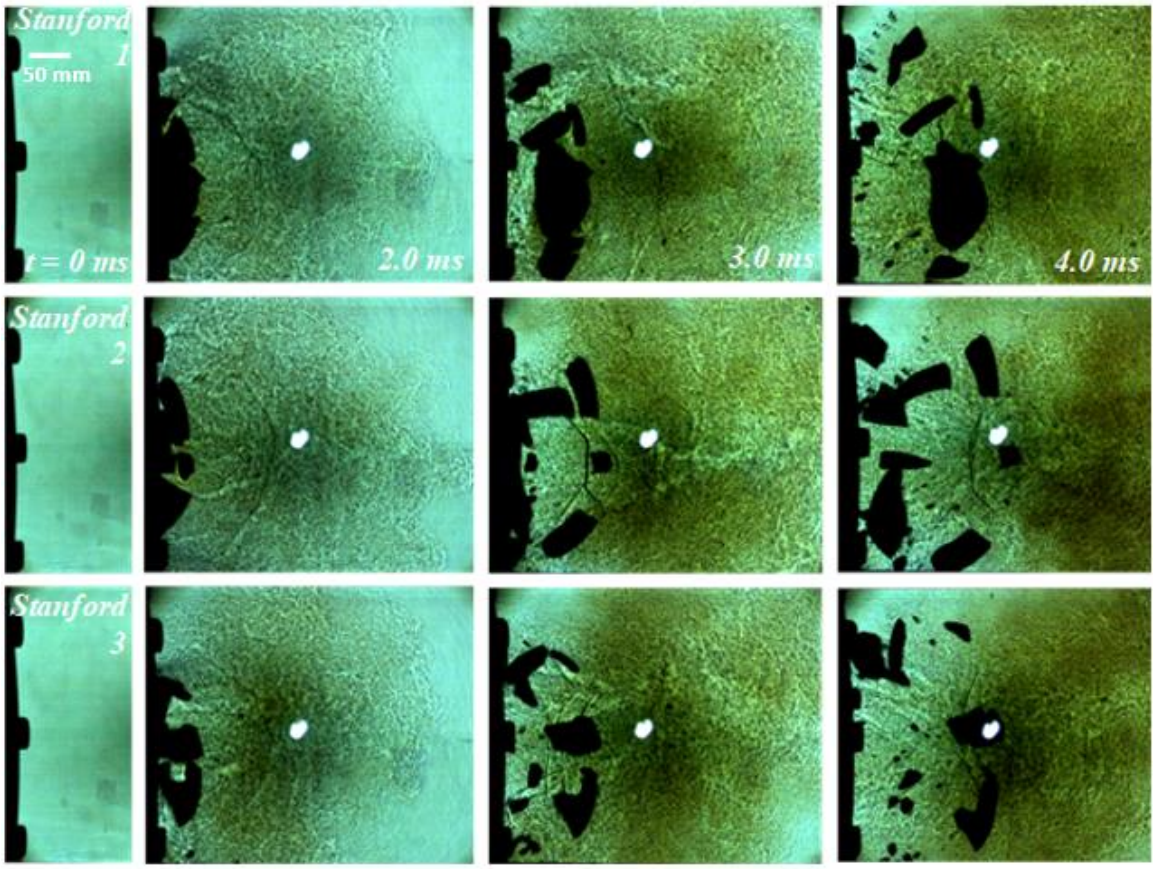

Figure 4.8: Stanford shadowgraphy images.

4.3 Fragment Size Analysis

Upon fracture, the fragments travel downstream and exit through the exhaust. The route the fragments travel is not a straight shot to the exhaust, instead they must pass through several sharp turns to exit. It is imperative that the average fragment size of the ruptured port cover is small enough so that they do not cause any damage to the internal structure of the air-breathing engine and the fragment size measurements are the most important factor in determining the viability of the alumina port covers in this investigation.

The average fragment size for the Ortech port covers fractured at 130 psi are 150.15 mm^2 with a standard deviation of 514.35 mm^2. The average fragment size for the Stanford port covers fractured at 130 psi is 127.49 mm^2 with a standard deviation of 564.15 mm^2. The average fragment sizes are derived using ImageJ techniques, previously detailed in Chapter 3. Figure 4.1 (a) and (b) display histograms with a bin size of 75 of the ImageJ fragment size results. For both Ortech and Stanford port covers, there is a large concentration of small, desirable fragments skewed to the lower end of the histograms. Unfortunately, the large amounts of small, satisfactory fragments do not alleviate the daunting handful of large fragments. Uncertainty present in these calculations stem from the human error in collecting the fragments. Large fragments are easy to find and collect, while the very small fragments are not as easily collected. This indicates that there is most likely an even larger concentration of very small fragments that were not able to be collected and therefore not included in these calculations.

Commonly observed in brittle materials, the fragmented pieces of a model are consistent in size with the thickness of the whole model. For example, in the ASALM-PTV investigation, a frangible chemically strengthened glass port cover with one-inch thickness throughout was used in the integrated ramjet rocket system [26]. After the port cover was fractured, the average fragment size was calculated to be 1 in^2. The alumina port covers in these experiments are 6mm thickness throughout, therefore a 6 mm^2 average fragment size was expected and desired.

However, it should be emphasized that in most realistic applications as well as the previously mentioned ASALM-PTV example [26], a detonation cord affixed to the port cover's dome face was used to fracture the port covers rather than a mechanical fracturing rod featured in these experiments. Although several fragments did measure to be within reasonable range of 6 mm^2, this mode of fracture has produced several outlying fragments which skew the average fragment size immensely, as illustrated by the large standard deviation values.

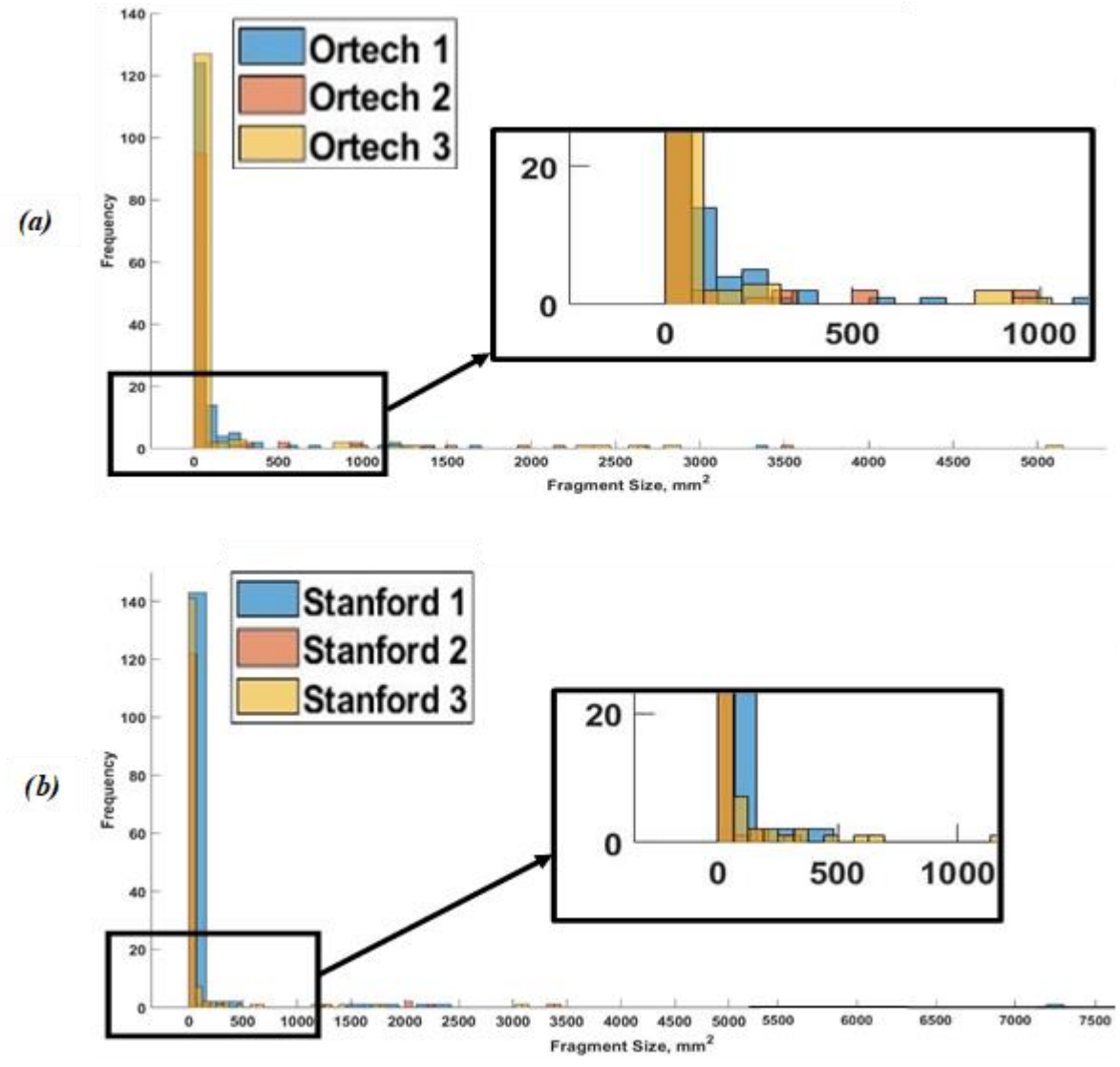

Figure 4.9: Fragment size histograms for a) Ortech and b) Stanford.

4.3.1 Fragment Recovery

The pressure chamber was specifically designed so that the port covers are capable of fracturing into true atmosphere to avoid further fragmentation beyond the initial fracture and consequently false fragment size results. With the importance of average fragment size in mind, several measures were taken to ensure fragments were as recoverable as possible. The pressure chamber facility is located in a bay with a garage door. During the experiments, the garage door is opened to allow a large exit area for the fragments, effectively converting the entire facility to true atmospheric conditions. As described in detail in Chapter 3, a large frame was constructed to block the fragments from travelling into the wooded area beyond the facility. To prevent further fragmentation upon impact, the frame was layered with 0.25-inch-thick rubber mats and 2-inch-thick foam insulation sheets, recall Figure 3.8. Due to the dome geometry, the port covers' wide fragmentation spread and ricochet caused some fragments to hit the floor directly in front of the pressure chamber. In response, the foam insulation sheets are also lined on the concrete floor directly in front of the pressure chamber.

An obvious uncertainty in the average fragment size results is the human error in collecting fragments. Despite thorough recovery efforts, it is likely that the fragments unable to be recovered are miniscule, while the largest fragments are easily collected. To quantify the fragment recovery process, the port covers are weighed prior to fracture and the fragments are weighed after fracture. As expected, higher percentages of fragments recovered correlated with smaller average fragment sizes, reported in Table 4.2.

An identifiable quadrant pattern was drawn on each port cover using permanent marker to characterize fracture patterns. Once the fragments were collected and weighed, each port cover was 'puzzled' back together in an effort to visualize which quadrant was most/least recovered. With the fracturing mechanism located firing into the dome face labeled quadrant 3, it is noted that quadrant 3 commonly featured smaller fragment sizes, especially around the point of impact. Figure 4.2 and 4.3 display each port cover quadrant pattern, remaining rim pieces post-rupture and the reconstructed port cover fragments for Ortech and Stanford, respectively.

It should be emphasized that the rim pieces are not included in the average fragment size data due to the fact they remain fixed in the pressure chamber frame and do not travel downstream. Recall in IRR operation, it is essential when the rocket boost phase is complete, the port cover is fragmented immediately allowing ramjet phase to take place. Ramjet operation requires compressed high-speed air provided by the inlet previously blocked by the port cover. Ideally, with mass flow restriction in mind, the entire dome portion of the port cover will be fragmented and exit the system while leaving only the support rim in the pressure chamber. If large rim pieces with dome face remnants do not fragment and exit post rupture, the ramjet phase is at risk.

Table 4.2: Fragment recovery percentage and average fragment size correlation.

Case	# of Fragments	Recovered %	Average Fragment Size (mm^2)	Fragment Size St. Dev. (mm^2)
Ortech 1	160	94.5%	126.87	373.50
Ortech 2	110	87.5%	163.28	541.76
Ortech 3	142	90.9%	160.29	625.78
Stanford 1	153	92.9%	134.43	735.25
Stanford 2	133	83.4%	133.42	532.21
Stanford 3	165	95.1%	114.61	424.99

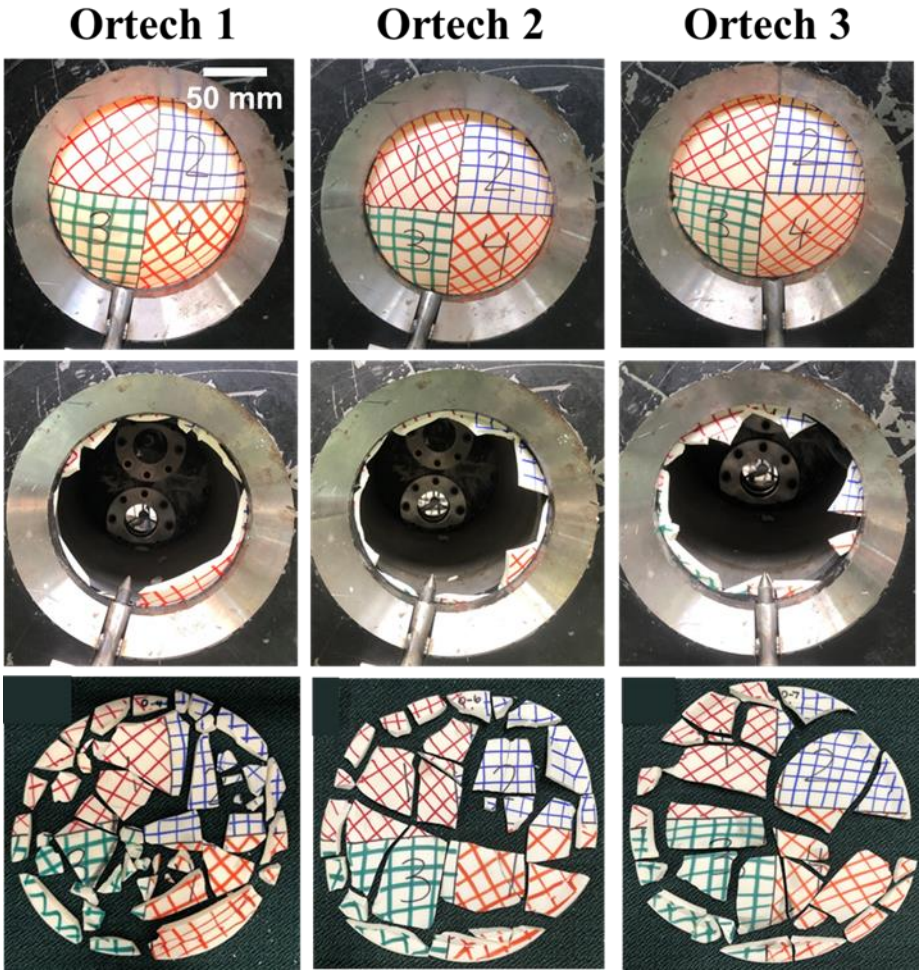

Figure 4.10: Ortech quadrant patterns, remaining rim pieces and reconstruction.

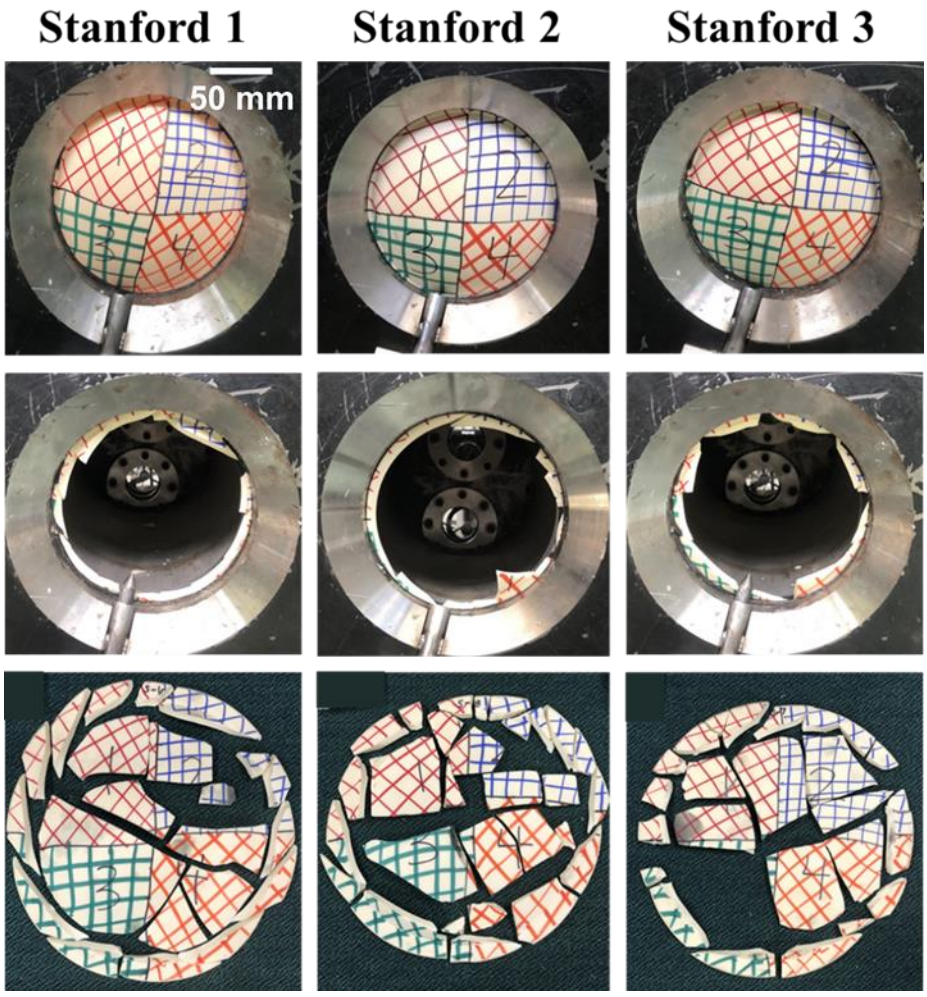

Figure 4.11: Stanford quadrant patterns, remaining rim pieces and reconstruction.

4.4 Phenomena

During these experiments, interesting and unexpected fluid dynamics phenomena were observed and unintentionally captured with the high-speed camera imaging techniques. A shockwave is defined as a propagating disturbance that moves faster than the local speed of sound and is characterized by an abrupt change in Mach number, pressure, temperature, density, and velocity of air [17]. Shockwaves form when the sound waves travelling upstream collide with a supersonic pressure front travelling downstream, creating a concentration of high-pressure. Energy is always preserved across shockwaves, but entropy always increases. This guaranteed increase in entropy is extracted as a drag force and ultimately makes the shockwave thermodynamics an irreversible process. Different types of shockwaves exhibit unique behavior and are generally formed as a function of the surrounding geometry. Normal shockwaves are perpendicular to the flow direction, while oblique shocks are at an angle to the flow direction. Oblique shocks are generally attached to sharp nosed objects and the angle between the shock and the body can be used to calculate the Mach number. Bow shocks, rather than attaching completely, occur directly upstream of a blunt body [17].

When the port cover is initially cracked by the mechanical fracturing rod striking the outer dome face, there is a miniscule delay (< 0.75 ms) during which the crack propagates across the dome face and then the entire port cover completely fragments due to pressure loads. During that delay, the pressurized air that is forcing the fragments downstream escapes the pressure chamber and accelerates downstream faster than the fragments. Interestingly, the retroreflective shadowgraphy unintentionally captures these supersonic shockwaves that attach to the travelling fragments, pictured in Figure 4.9. Depending on rotation and orientation while travelling downstream, some of the fragments feature sharp noses geometries which are associated with attached oblique shocks. Other fragments are considered blunt body geometries which are associated with detached bow shocks. The associated shockwave with each of these geometries are accurately represented in these images.

Another phenomenon that is observed is that an under expanded jet is mimicked when the pressurized air exits the chamber into true atmosphere following port cover fracture. The large pressure gradient generates a Prandtl-Meyer expansion fan followed by an intersecting oblique shockwave. When characteristics of the same family intersect one another in the flow, shockwaves form in supersonic jets [59]. With increasing pressure ratio between the chamber and ambient conditions, or between the nozzle and ambient conditions in the case of an under expanded jet, the characteristics intersect further and further upstream and a Mach reflection occurs in the middle of the flow. This Mach reflection is a normal shock known as a Mach disk for axisymmetric flow [59], a common occurrence in aircraft pictured from shadowgraphy imaging in Figure 4.10.

In a true under-expanded jet, the aircraft exhaust passes through the Mach disk and its temperature increases sharply. Excess fuel in the exhaust stream can be ignited due to the elevated temperature and produces the visible glow referred to as shock diamonds [59]. The Mach disk is considered the first shock diamond and if the Prandtl-Meyer expansion fans and oblique shockwave intersections are strong enough, several Mach disks may form. If the gases were ideal and frictionless, the pattern of disks and diamonds would repeat indefinitely, however the pattern eventually dissipates due to turbulent shear effects. Aircraft engine performance is sometimes qualitatively characterized by the number of Mach disks it produces.

A final materials science phenomenon present in these results is triboluminescence in which flashes of light are emitted when a material is mechanically fractured. Although this phenomenon is not fully understood yet, theory suggests that upon fracture, the charge is separated and when the charge recombines, the electrical discharge ionizes the surrounding air causing a flash of light [60]. Triboluminescence occurs not when the fracturing mechanism initiates a crack, but as the alumina fragments collide with each other, specifically located where the dome face fragments away from the outer support rim, pictured in Figure 4.11. Triboluminescence is attributed to materials with crystalline microstructures, such as alumina and also sugar. This phenomenon is commonly demonstrated by using a hammer to crush a piece of hard candy.

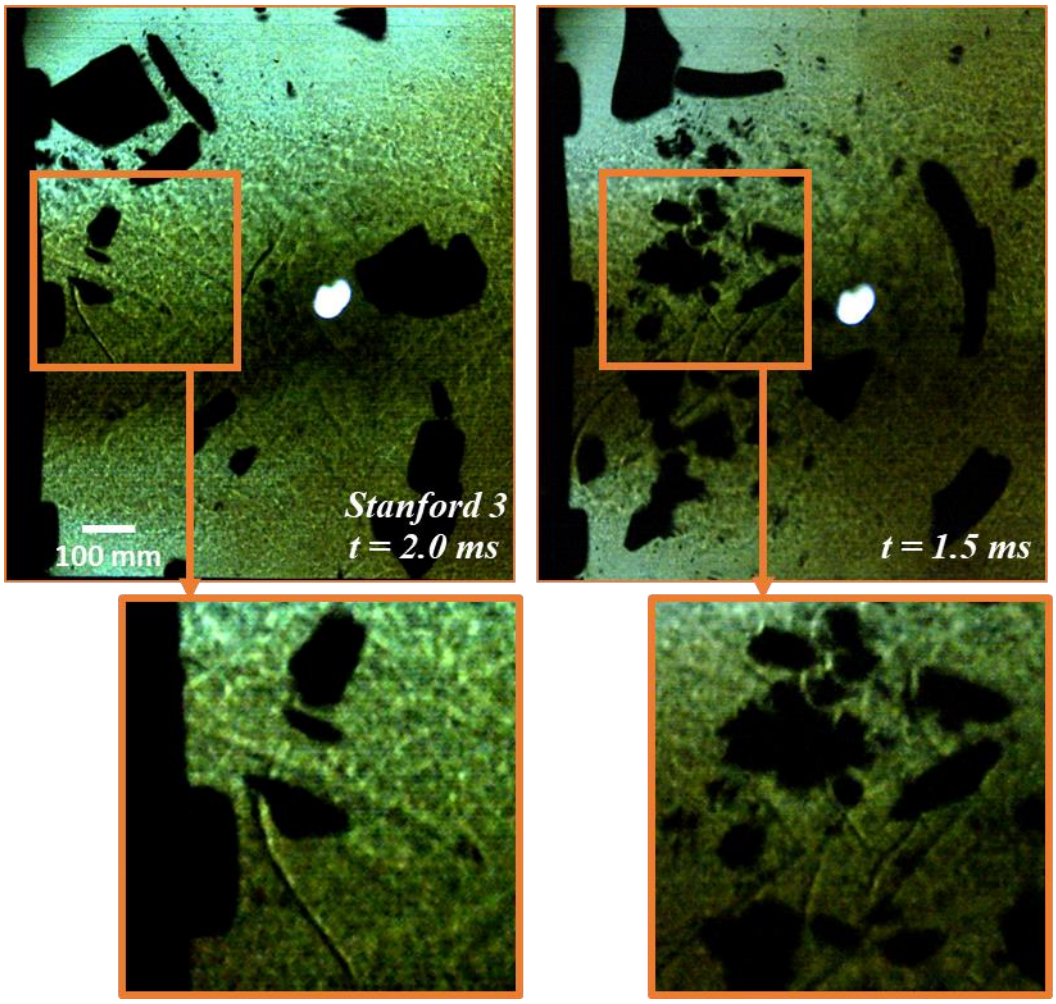

Figure 4.12: Shockwaves attached to port cover fragments.

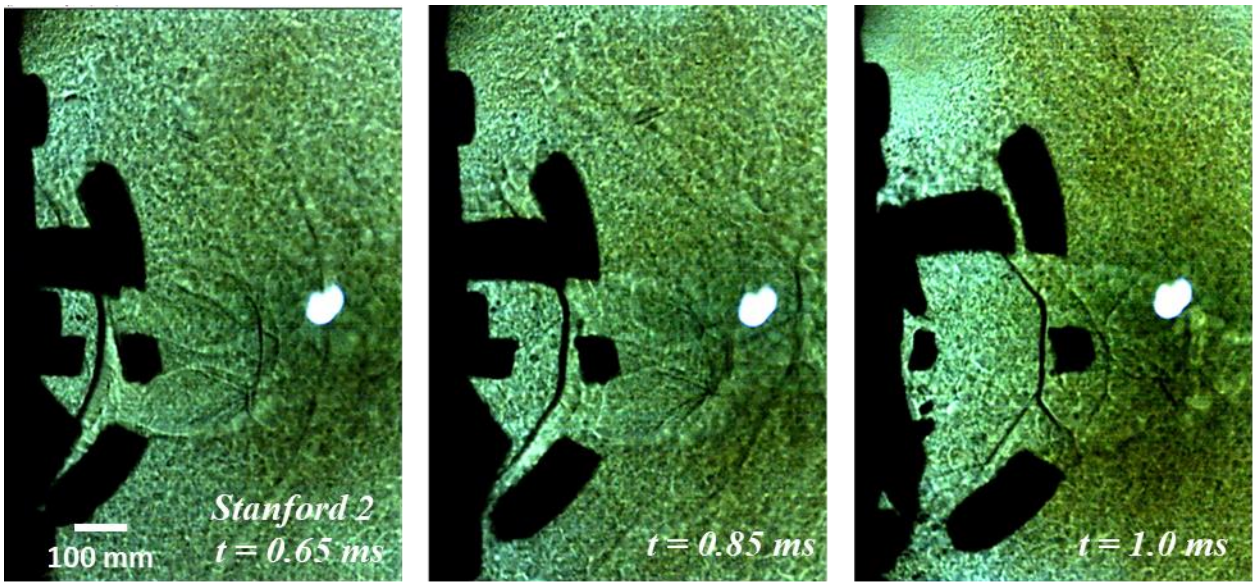

Figure 4.13: Mach disks forming due to large pressure ratio.

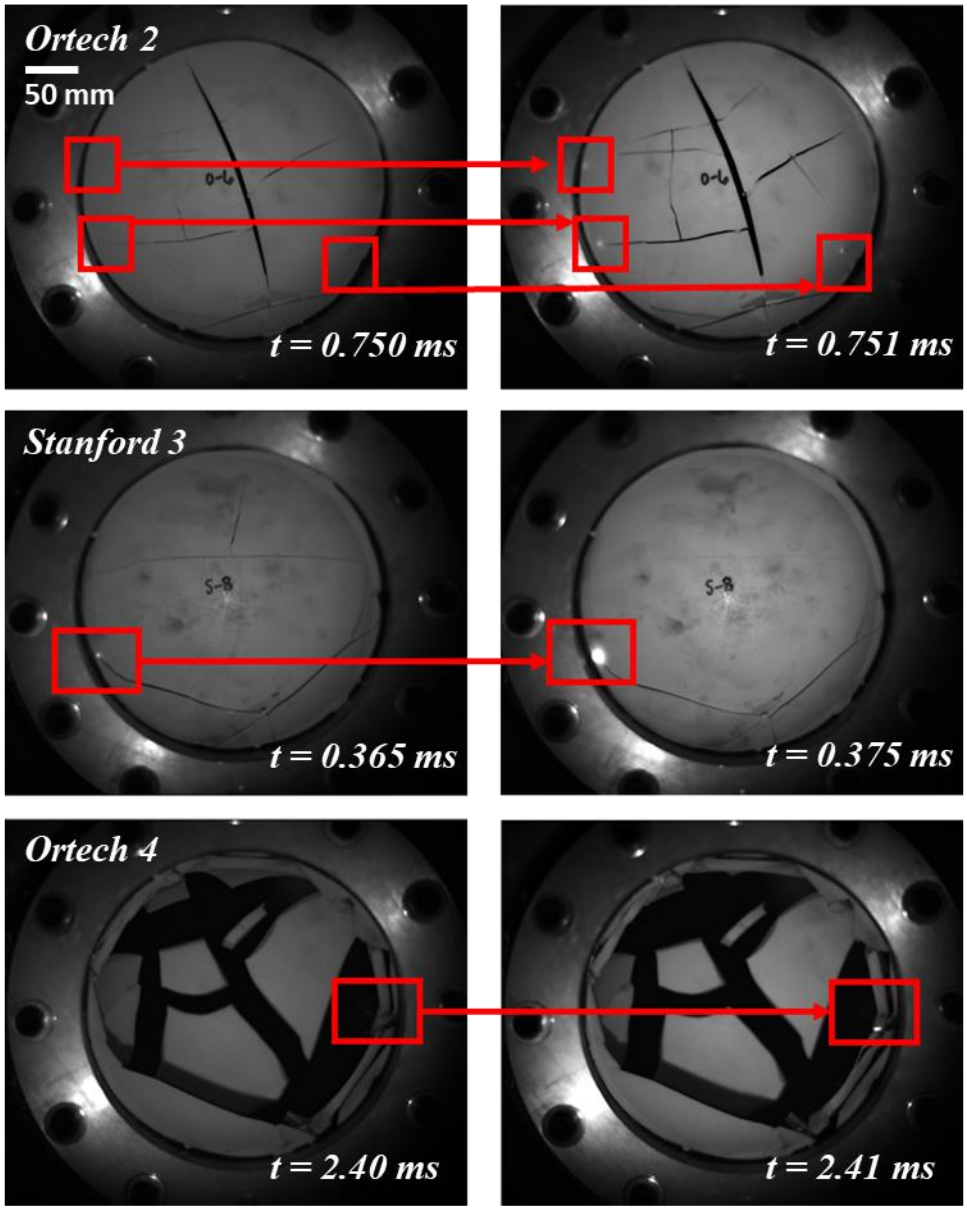

Figure 4.14: Triboluminescence flashes during initial fracture.

CHAPTER FIVE

CONCLUSIONS

Alumina port covers designed for use in integrated ramjet rocket systems were investigated in collaboration with Air Force Research Labs and NASA Langley Research Center to support the development of hypersonic flight technologies. The engineering ceramic alumina is chosen because it is widely available and has the desired thermal properties, compressive strength and frangibility required for use in these IRR systems. Port covers have been studied for a relatively long period beginning in the 1970's during the Advanced Strategic Air-Launched Missile (ASALM) program up to the parametric evaluation performed by Air Force Research Labs (AFRL) in 2019. The AFRL numerical study provided the most efficient port cover geometry to feature a 45-degree dome angle and 6mm thickness throughout. The port cover geometry was modified by removing bolt holes in the outer support rim to alleviate unnecessary additional stress concentration locations and redesigning the port cover to be a perfect circle instead of slightly oblong to decrease production cost.

Since the port cover was modified, additional finite element analysis (FEA) stress analysis was required to verify it could withstand the same pressure loads as the original model. Solidworks and Ansys were used to perform the FEA stress analysis on two alumina concentrations of 99.5% and 99.7%, in which the entire outer support rim was fixed and pressure loads were applied to the upstream and downstream faces of the dome. Data were collected on maximum deflection and maximum principal stress. Maximum deflection, a measure of deformation a material experiences under a load, was calculated to be 13.1 μm in Solidworks and 14.0 and 13.5 μm in Ansys for the 99.5% and 99.7% alumina concentration respectively. These results were expected for a brittle material such as alumina which experiences little to no deformation before fracture. Maximum principal stresses, the value at which if it exceeds the ultimate tensile strength of that material failure will occur, were found to be 127.0 MPa in Solidworks and 133.1 MPa in Ansys for both the 99.5% and 99.7% alumina concentrations. These results conclude that the modified design withstands the same pressure loads in the original AFRL model using the same FEA stress analysis techniques.

Alumina, the engineering ceramic of interest, is inherently brittle. Brittle fracture is defined as sudden failure of a material caused by the rapid propagation of cracks. In a tensile test, brittle materials feature no visible plastic deformation and a smooth fracture surface indicating a clean break. This fracture surface is attributed to the crystalline microstructure of alumina. Like most ceramics, alumina is made by metals that are covalently bonded with non-metals. These covalent bonds are strongly directional and therefore resistive to deformation, leading to a very hard and brittle material. Despite impressive compressive strength properties, due to the microstructure, brittle materials feature low ductility and, consequentially, low tensile strength.

Alumina port covers are manufactured by compacting the alumina powder into the desired geometry by hot or cold pressing. This is said to be the green state and most necessary machining is done at this point when the piece is weak because once the piece is fused and hardened, machining becomes much more difficult. The piece is then sintered for several hours at extremely high temperatures in order to fuse the powder into a solid. Several surface finishes are available from as fired, which is what this investigation used, up to a mirror finish, which is extremely expensive.

To obtain a more comprehensive understanding of performance with minimal impact from vendor specific manufacturing processes, the port covers used in this experiment were fabricated and purchased from three external vendors: Ortech Inc., Stanford Advanced Materials and Precision Ceramics. A microscope was used to obtain surface roughness images and although manufacturing processes from each vendor were virtually identical, the surface roughness images displayed stark differences in machining marks, mixing impurities and pre-existing flaws before testing began. Recall from Figure 4.1, the microscopic surface roughness images demonstrate a much more uniform and smoother surface the Precision Ceramics port cover has than that of Ortech and Stanford. Since alumina has an ultimate tensile strength of 390 MPa, the FEA stress analysis maximum principal stress results suggest that the port covers should not fracture due to pressure loads alone, a critical requirement for ramjet operation. However, due to the presence of these visible pre-existing cracks and flaws, experimental failure occurred at much lower pressures than expected in two out of the three vendors. Ortech and Stanford failed to withstand the maximum pressure loads of 450 psi. Although Precision Ceramics port covers were successfully fractured in preliminary tests when characterizing maximum burst pressures, the fracturing method used in these experiments failed to fracture this brand of port covers at the pressure of 130 psi. Meaningful data is reported for three Ortech port covers and three Stanford port covers.

Initial crack propagation caused by the fracturing rod striking the downstream dome face and corresponding fracture pattern was visualized by utilizing the two windows that were designed in the pressure chamber. The first window allows for optical access of the upstream dome face while the second window is used for a light source to illuminate the port cover. The initial crack formed by the fracturing rod striking the port cover is the determining factor to the entire fracture propagation pattern of the port cover. After the crack is initiated, the pressure loads are responsible for fully fracturing the port cover. The observed fracture patterns caused by the pressure loads agree well with FEA stress analysis results in that the fragmentation was likely to occur where the highest stress concentrators were located. It is common in brittle materials for failure or fracture to occur where there is a sharp change in geometry and the highest stress concentrators are located where the outer support rim meets the dome face. The fracture pattern data provided qualitative data that emphasized the influence the fracture mechanism posed on the crack propagation and confirmed that most of the pressure-influence fragmentation occurred around the rim where the dome meets the flat region while the fracturing rod supplied the fracture mechanics of the dome face.

The port covers were installed and tested in a high-pressure chamber capable of providing up to 600 psi and operation in an open or closed state. Safety precautions and facility location allowed for open state operation where the port covers burst into true atmosphere which allows enhanced optical access and alleviates further fragmentation upon impact with the closed state design. The port covers were installed into a frame then attached to the pressure chamber, which was then raised to 130 psi to simulate realistic pressure loads a port cover will encounter during flight conditions. Once the desired pressure was reached, a mechanical fracturing mechanism was used to initiate fracture onto the pressurized port cover. A steel rod is triggered to fire with the use of a pneumatic cylinder to strike the dome face and cause an initial crack, compromising the port cover's strength and allowing the pressure loads to fully fragment the port cover. In order to visualize the motion of the fragments and surrounding air, the fracture and subsequent fragments travelling downstream were captured by the retroreflective shadowgraphy imaging technique. The average fragment velocity was calculated to be 101.9 m/s for Ortech with a standard deviation of 30.78 m/s. The Stanford port cover average fragment velocity was calculated to be 112.8 m/s with a standard deviation of 24.79 m/s.

After rupture, the fragments were then collected and surface area measurements were recorded using ImageJ techniques. ImageJ calculates the number of fragments collected, each individual fragment size in area and the average fragment size. It is important to emphasize one more time that it is imperative that the fragments are small enough so that they do not cause damage to the IRR system when they exit through the exhaust. The fragment size analysis is considered to be the most important data in these experiments. Fractured at 130 psi, the average fragment size for Ortech port covers is 150.15 mm^2 with a standard deviation of 514.35 mm^2. Stanford port covers results in an average fragment size of 127.49 mm^2 with a standard deviation of 564.15 mm^2.

The large standard deviations indicate that the average is not a fully accurate representation of fragment size. For both Ortech and Stanford, the fragment size histograms are extremely skewed to the lower end, more specifically the very first bin. Unfortunately, the large concentration of small, satisfactory fragments does not alleviate the daunting handful of large fragments. It should be emphasized that in most realistic applications a detonation cord affixed to the port cover's dome face is used to fracture the port covers rather than a mechanical fracturing rod featured in these experiments. From the results of this numerical and experimental campaign, the major research objective of this investigation to determine if alumina port covers are suitable for vehicle use cannot be fully concluded yet. Additional research is necessary.

5.1 Future Work

Smaller fragment size is the most obvious goal of this continuing campaign and should be the focus moving forward. The extremely large fragments are likely attributed to the pre-existing flaws or cracks caused by manufacturing processing, which can cause failure at a pressure well below the material's yield strength, and/or the mechanical fracture initiation method, which heavily influences the fracture pattern of the port cover. The fracture initiation method currently features a single contact point where the rod strikes the bottom corner of the dome face, labeled consistently as quadrant 3. Through port cover reconstruction, quadrant 3 generally contained the smallest fragments which leads to the idea that a multi-point fracture could minimize the fragment size. A basic diagram from the front view of the pressure chamber is pictured in Figure 5.1 where a fracturing mechanism located at all four port cover quadrants. The mulit-point fracture mechanism would be synced to strike in unison from the same triggering system used for single-point fracturing.

A threshold of acceptable versus non-acceptable fragment sizes has not been characterized yet. It is necessary to determine a maximum allowable fragment size in future work. One idea to characterize that value is to place several fabricated "fragments" of varying surface area in the pressure chamber under the same loading conditions the whole port covers are exposed to. Utilizing the high-pressure chamber's closed state operation as a mock IRR system, allow the fragments to "burst" and travel downstream. If successful, the evaluation of the damages caused by each group of corresponding fragment size can be used to determine a threshold. With that, a percentage of acceptable versus non-acceptable fragment sizes can be calculated from each port cover which would determine if the port cover design material can be deemed fit or unfit for vehicle use.

Another idea to minimize fragment size is to score the upstream dome face with a rectangular grid pattern, pictured in Figure 5.2. With the geometry modification, finite element stress analysis of the scored model is necessary in future work to determine the maximum deflection and maximum principal stresses.

When calculating the average fragment velocity, there was uncertainty present due to the two-dimensional nature of the retroreflective shadowgraphy technique. Fragments appeared to move only in the x-direction while it is known that the fragments are travelling and rotating in the y- and z-directions simultaneously. Utilizing a multi-camera system in the future could account for this velocity measurement uncertainty and provide better detail of the spread angle at which the port covers burst.

One final note for future work is the use of dry air in the high-pressure chamber. In the retroreflective shadowgraphy images, the wet air appears as a large shadow that completely covers the fragments, effectively making obsolete the large field of view that was obtained. Dry air would improve the shadowgraphy images, allow for a larger sample size and in turn provide more accurate fragment velocity measurements.

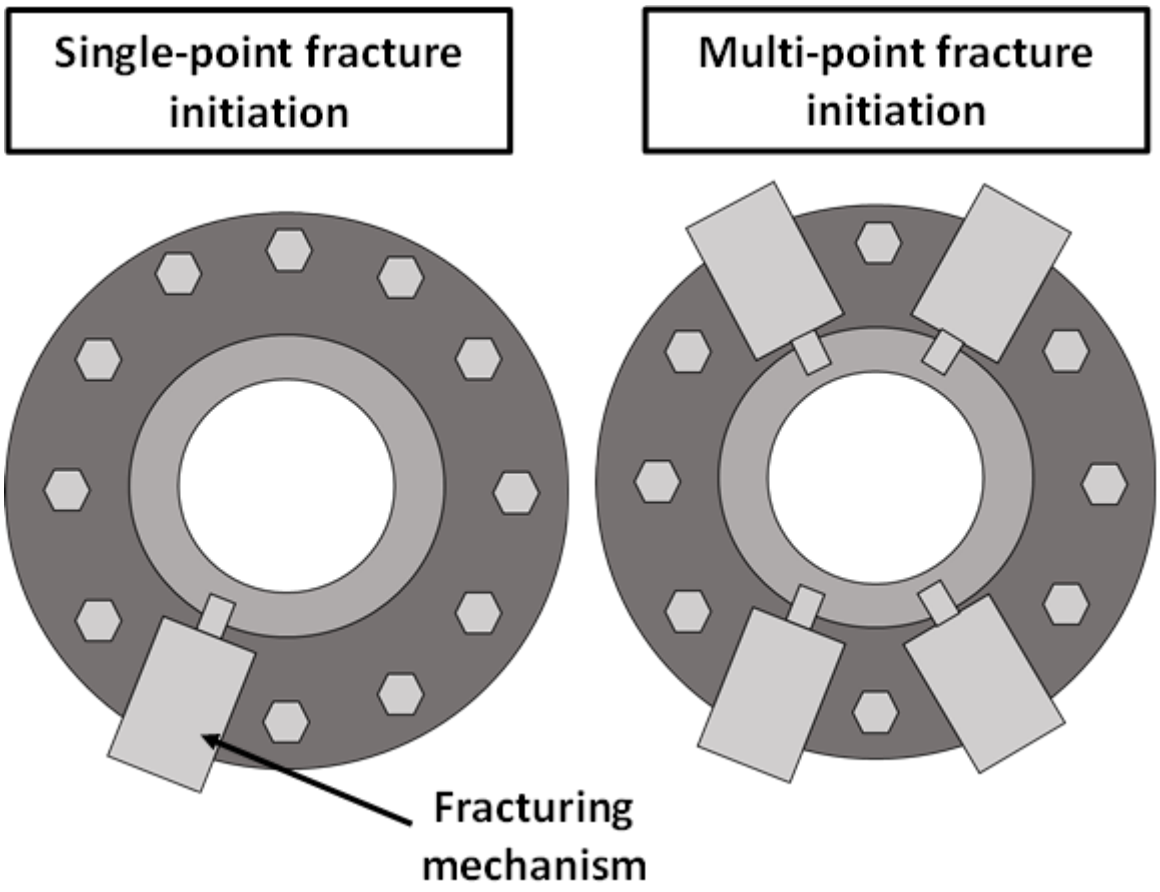

Figure 5.1: Multi-point fracture initiation to minimize fragment size.



Figure 5.2: Scoring of port cover dome face in rectangular grid pattern to encourage smaller fragment size.

REFERENCES

[1] Sayler, H. M. (2019). *Hypersonic weapons: Background and issues for Congress*. Congressional Research Service.
[2] Hyten, J. (2018). *Statement of John E. Hyten Commander United States Strategic Command before Senate Committee on Armed Services*.
[3] Karako, T. (2019). *The Missile Defense Review*. Strategic Studies Quarterly, *13*(2), 3-15.
[4] Force, U. A. (2019). *Department of Defense Fiscal Year (FY) 2020 Budget Estimates, Air Force Justification Book.* Volume 2 of 3: Research, Development, Test & Evaluation, Air Force Vol− II, February, 691.
[5] Speier, R. H., Nacouzi, G., Lee, C., & Moore, R. M. (2017). *Hypersonic missile nonproliferation: hindering the spread of a new class of weapons*. Rand Corporation.
[6] Trimble, S. (2020). *USAF Errantly Reveals Research on ICBM-Range Hypersonic Glide Vehicle*. Aviation Week. August 18.
[7] Hitchens, T. (2020). *Hypersonic Missiles: Plethora of Boost-Glide & Cruise*. Vol. 2020, Breaking Defense.
[8] Acton, J. M. (2015). *Hypersonic boost-glide weapons*. Science & Global Security, 23(3), 191-219.
[9] Heiser, W. H., Pratt, D. T., & Daley, D. H. (1994). *Hypersonic airbreathing propulsion*. AIAA.
[10] Anderson Jr, J. D. (2010). Fundamentals of aerodynamics. Tata McGraw-Hill Education.
[11] Anderson, J. D. (2000). Hypersonic and high temperature gas dynamics. Aiaa.
[12] Trimble, S. (2019). *New Long-Term Pentagon Plan Boosts Hypersonics, But Only Prototypes*. Aviation Week, March 15.
[13] Fry, R. S. (2004). A century of ramjet propulsion technology evolution. *Journal of propulsion and power*, *20*(1), 27-58.
[14] Webster, F. F. (1982). Integral rocket/ramjet propulsion-flight data correlation and analysis techniques. *Journal of Spacecraft and Rockets*, *19*(4), 326-336.
[15] Dugger, G. L. (1959). Recent advances in ramjet combustion. *ARS Journal*, *29*(11), 819-827.
[16] Waltrup, P. J., White, M. E., Zarlingo, F., & Gravlin, E. S. (2002). History of US Navy ramjet, scramjet, and mixed-cycle propulsion development. *Journal of propulsion and power*, *18*(1), 14-27.
[17] Anderson, J. D. (1990). *Modern compressible flow: with historical perspective* (Vol. 12). New York: McGraw-Hill.
[18] White, F. M., & Majdalani, J. (2006). *Viscous fluid flow* (Vol. 3, pp. 433-434). New York: McGraw-Hill.
[19] Jenkins, D. R. (2000). Hypersonics before the shuttle: A concise history of the X-15 research airplane (No. 18). National Aeronautics and Space Administration, NASA Office of Policy and Plans, NASA History Office, NASA Headquarters.
[20] Fry, R., & Fry, R. (2011). The US Navy's Contributions to Airbreathing Missile Propulsion Technology. In AIAA Centennial of Naval Aviation Forum" 100 Years of Achievement and Progress" (p. 6942).
[21] Majumdar, S. (2018). MBDA's Meteor BVRAAM. Vayu Aerospace and Defence Review, (4), 44-46.

[22] Jackson, K., Gruber, M., & Buccellato, S. (2011). HIFiRE flight 2 project overview and status update 2011. In *17th AIAA International Space Planes and Hypersonic Systems and Technologies Conference* (p. 2202).
[23] McClinton, C. (2006). X-43-Scramjet power breaks the hypersonic barrier: Dryden lectureship in research for 2006. In *44th AIAA aerospace sciences meeting and exhibit* (p. 1). January.
[24] Smart, M. K., Hass, N. E., & Paull, A. (2006). Flight data analysis of the HyShot 2 scramjet flight experiment. *AIAA journal*, *44*(10), 2366-2375.
[25] Taylor, R. (2020)."Private Communication: Excerpts from AFRL Scholars summer progress report." AFRL/RWP.
[26] Webster, F., & Bucy, J. (1979). *ASALM-PTV chin inlet technology overview*. Advanced Strategic Air Launched Missile Propulsion Technology Validation of integral rocket/ramjet. In *15th Joint Propulsion Conference* (p. 1240).
[27] Johnson, G. (2021, July 1). Another ramjet that I worked on. [Blog post]. Retrieved from https://exrocketman.blogspot.com/2021/07/another-ramjet-that-i-worked-on.html
[28] Küchemann, D. (2012). *The aerodynamic design of aircraft*. American Institute of Aeronautics and Astronautics, Inc.
[29] Scannel, P., Milich, N., & Kalil, E. (1980). Advanced integral rocket ramjet port cover development. In *16th Joint Propulsion Conference* (p. 1279).
[30] Hwang, K. T., Kim, J. H., Lee, Y. S., Kwon, S. G., Park, J. H., & Song, K. H. (2010). A study on fracture phenomena of glass filled ceramics using shock tube. *Materialwissenschaft und Werkstofftechnik*, *41*(5), 306-313.
[31] Szabó, B., & Babuška, I. (1991). Finite element analysis. John Wiley & Sons.
[32] Akin, J. E. (2010). *Finite element analysis concepts: via SolidWorks*. World Scientific.
[33] Dhondt, G. (2017). CalculiX CrunchiX User's Manual Version 2.12. *Munich, Germany, accessed Sept*, *21*, 2017.
[34] Werrell, K. P. (1985). The evolution of the cruise missile. Air University Maxwell AFB AL.
[35] Webster, F. F. (1989). Ramjet development testing-Which way is right?. Journal of Propulsion and Power, 5(5), 565-576.
[36] Billig, F. S. (1993). Research on supersonic combustion. Journal of Propulsion and Power, 9(4), 499-514.
[37] Anderson, T. L. (2017). Fracture mechanics: fundamentals and applications. CRC press.
[38] Norman E. Dowling, Mechanical Behavior of Materials, 2nd edition, prentice hall, 1999.
[39] Hertzberg, R. W., Vinci, R. P., & Hertzberg, J. L. (2020). *Deformation and fracture mechanics of engineering materials*. John Wiley & Sons.
[40] Dey, A. (n.d.). Brittle fracture and ductile fracture: definitions, mechanism, differences. [Blog post]. Retrieved from https://whatispiping.com/brittle-fracture-ductile-fracture/
[41] Budynas, R. G. (1977). Advanced strength and applied stress analysis. McGraw-Hill Science, Engineering & Mathematics.
[42] Failure criteria for brittle materials. (n.d.) Retrieved October 28, 2021, from https://www.efunda.com/formulae/solid_mechanics/failure_criteria/failure_criteria_brittle.cfm
[43] Angus, H. T. (2013). Cast iron: physical and engineering properties. Elsevier.

[44] Auerkari, P. (1996). Mechanical and physical properties of engineering alumina ceramics (Vol. 23). Espoo: Technical Research Centre of Finland.
[45] Rybicki, E. F., Simonen, F. A., & Weis Jr, E. B. (1972). On the mathematical analysis of stress in the human femur. Journal of biomechanics, 5(2), 203-215.
[46] Waltham, T. (2002). Foundations of engineering geology. CRC Press.
[47] Maca, K. (2009). Microstructure evolution during pressureless sintering of bulk oxide ceramics. *Processing and Application of Ceramics*, *3*(1-2), 13-17.
[48] Alumina 99.5% material properties. Retrieved November 15, 2021 from https://www.ortechceramics.com/creamic-materials/alumina-ceramics/.
[49] Alumina 99.5% material properties. Retrieved November 15, 2021 from https://www.samaterials.com/199-alumina.html.
[50] Alumina 99.7% material properties. Retrieved November 15, 2021 from https://precision-ceramics.com/materials/alumina/.
[51] Thompson, M. K., & Thompson, J. M. (2017). *ANSYS mechanical APDL for finite element analysis*. Butterworth-Heinemann.
[52] 8020 aluminum extrusion. Retrieved November 15, 2021 from https://8020.net/framing-options/t-slotted-profiles.html.
[53] Pneumatic Cylinders. Retrieved November 15, 2021 from https://www.mcmaster.com/pneumatic-cylinders/.
[54] Photron FASTCAM miniseries. Retrieved October 28, 2021, from https://photron.com/mini-range/
[55] Nikon lenses. Retrieved October 28, 2021, from https://www.nikonusa.com/en/nikon-products/lenses.page
[56] Settles, G. S. (2001). *Schlieren and shadowgraph techniques: visualizing phenomena in transparent media*. Springer Science & Business Media.
[57] Abràmoff, M. D., Magalhães, P. J., & Ram, S. J. (2004). Image processing with ImageJ. *Biophotonics international*, *11*(7), 36-42.
[58] White, F. M. (2015). *Fluid mechanics.* 8th ed. New York: McGraw-Hill Education.
[59] Keith, T. G., & John, J. E. (2006). *Gas dynamics.*
[60] Walton, A. J. (1977). Triboluminescence. *Advances in Physics*, *26*(6), 887-948.

VITA

Haley Regan Goldston was born in Lakenheath, England to Chad and Billie Goldston. Haley and her older brother Chane were raised in Biloxi, Mississippi and graduated high school in Harriman, Tennessee. She began her academic career in the fall of 2015 at Roane State Community College in Harriman, Tennessee where she was the starting pitcher for the softball team. After earning her Associate degree in pre-engineering, she continued her education in 2017 at Tennessee Technological University in Cookeville, Tennessee where she graduated with a Bachelor of Science in Mechanical Engineering. During her time at TTU, she joined the Society of Women Engineers and continues to be an active member. Haley joined the HORIZON research group in 2020 to pursue a Masters of Science in Aerospace Engineering under the advisement of Dr. John Schmissuer.